A Study of Planar Velocity Dynamos

and Related Issues

Al Haji Akbar Bachtiar

School of Mathematics and Statistics
The University of Sydney
March 2009

A thesis submitted in fulfillment of the requirements for the degree of Doctor of Philosophy

Preface

I would like to thank A/Prof. Ron James for his guidance, support and time in preparing this thesis. And also thanks to Dr. D.J. Ivers for providing helpful ideas. Except where otherwise indicated, the work in this thesis is original, and the thesis contains no material which has been accepted for the award of any other degree. This candidature is sponsored by an Australian Agency for International Development scholarship (*www.ausaid.gov.au*) and was conducted during my study leave from Mathematics Department, University of Indonesia.

Abstract

This thesis is essentially a numerical investigation of planar velocity dynamos. It was believed that the existence of planar velocity dynamos is ruled out by the planar velocity theorem (PVT). The PVT is an example of an anti dynamo theorem. This particular theorem eliminates the possibility of having a dynamo process when the flow is planar (i.e. parallel to some plane). All PVT proofs, given by earlier authors (e.g. Zel'dovich (1957), Lortz (1968), and Moffat (1978)), were based on the conductor occupying all space. Bachtiar, Ivers and James (BIJ, 2006) showed that the PVT proofs fail for a finite spherical conductor. BIJ found a numerical model, model p1Y22DM12, that indicates the possible existence of a planar velocity dynamo. However, BIJ did not obtain fully satisfactory results due to convergence problems.

In Chapter 3, the BIJ successful model is reconsidered using higher truncation levels, to get better convergence than BIJ. A sub-band method is devised in order to obtain numerical results at these higher truncation levels. The size of the matrix band is up to 39 GB. Using these higher truncation levels, the convergence level of the eigenvalue ($\lambda_{\max}$) is significantly better than that of BIJ. In addition, a more prospective model, model p1q10Y22DM12, is investigated. The $\lambda_{\max}$ of this model converges better than that of p1Y22DM12.

In Chapter 4, insulating and conducting inner cores are included in our numerical experiments, to investigate the effect of an inner core on the convergence level of models p1Y22DM12 and p1q10Y22DM12. The boundary conditions for both types of inner core are derived. The numerical results show that the convergence levels for models p1Y22DM12 and p1q10Y22DM12, are better in spherical shells. It is also shown that a simple modification of the Pekeris, Accad, Skholler (PAS, 1973) flow, in a spherical shell, allows us to transform that flow into a planar flow. This leads us to propose two modifications of the PAS flow that can be fully planarized in a sphere.

Thus, two PAS-like flows, BiPAS and QuasiPAS, are introduced in Chapter 5. The unplanarized, partly planarized and fully planarized versions of these flows are investigated. Nineteen new successful dynamos are found for the unplanarized and partly planarized versions of the BiPAS and QuasiPAS models. Fourteen of these new dynamos have lower critical Reynolds numbers than that of model PAS. No dynamos were found for the fully planarized version of the BiPAS and QuasiPAS models over the interval of Reynolds numbers investigated.

Lastly, in Chapter 6, the convergence of kinematic dynamos is investigated using several convergence tests. The aim of this chapter is to closely examine the convergence of planar velocity dynamos. Besides some classical tests (e.g the $\lambda, \mathbf{B}, (S, T)$ tests), two new convergence tests: SRMS and VRMS are introduced. These tests are applied to the some historical models, to determine the most sensitive and convenient test. It is found that no test is always most sensitive, and that the SRMS graphs are

the most convenience visual test to use, especially for higher truncation levels. Finally, all of the above tests are applied to models p1Y22DM12 and p1q10Y22DM12. All tests, except the $\lambda_{\max}$ test, reveal that these models have converged below a 1% level (in various senses as defined in Chapter 6).

Contents

Chapter 1

Introduction

Credit for the initial dynamo hypothesis for an astro-planetary magnetic field is usually given to Larmor (1919). He proposed self-excited dynamos as an explanation for the magnetic fields of the Sun and the Earth. Later, researchers found several conditions that prevent dynamo action from being maintained. These conditions form the basis of anti-dynamo theorems. The first anti-dynamo theorem was established by Cowling (1934). He showed that a steady axisymmetric magnetic field cannot be maintained by an axisymetric velocity field, where magnetic and velocity fields are in a meridional plane. Backus and Chandrasekhar (1956) attempted to generalize Cowling's theorem by using axisymetric magnetic and velocity fields which are not in a meridional plane. A more general and extensive investigation on the axisymetric anti-dynamo theorem was given by Ivers and James (1984, IJ).

However, Backus (1958) and Herzenberg (1958) established that self-excited dynamos do exist. Later on, in 1970, Childress and G.O. Roberts showed the impossibility of establishing a general anti-dynamo theorem (Merrill, McElhinny and McFadden, 1996). Furthermore, several researchers, including G.O. Roberts, found flow models that can induce a self-excited dynamo.

Although self-excited dynamo models are well established, some scientists are still interested in the study of anti-dynamo theorems. The planar velocity theorem, one of the anti-dynamo theorems, was recently discussed by Bachtiar, Ivers and James (2006, BIJ). This theorem was originally considered by Zel'dovich (1957). In this work, Zel'dovich proved a planar velocity is not able to maintain a magnetic field, when the conducting fluid occupies all space. BIJ showed that Zel'dovich's proof is not valid for a finite volume conductor. They also discovered a Y_2^2 (spherical harmonic) model that supports their claim. However, their numerical results did not achieve a fully satisfactory level of convergence.

In this thesis, we try to provide better numerical evidence for the existence of planar velocity dynamos, following BIJ's work. We discuss some numerical investigations of planar velocity dynamos which include: evaluating BIJ's model using higher

truncation levels, studying variations of BIJ's model including the presence of an inner core, studying several partly and fully planarized flows based on the Pekeris, Accad and Skholler (1973, PAS) flow, and investigating the convergence of planar velocity dynamos.

In Chapter 2, we provide a brief introduction to kinematic dynamo theory. Then, the spectral form of the induction equation is explained and the numerical methods used are detailed. At the end of Chapter 2, we discuss the planar velocity theorem, including its original proof and an argument that shows that the proof fails for finite conductors, such as a sphere.

The numerical investigation of planar velocity dynamos is the subject of Chapter 3. We start our discussion with the derivation of the spectral form of planar flows. Then, we investigate some planar flows which are: (a) single harmonic flows and (b) planarized versions of three historical flows (Bullard and Gellman flow (1954, BG), PAS flow and Kumar and Roberts flow (1975, KR)). A modification of our numerical dynamo routine using a sub-band method is detailed. This method allows us to present results using much higher truncation levels. We present the numerical results of four dynamo models with a single harmonic flow using high truncation levels.

In Chapter 4, we include both insulating and conducting inner cores in our models. We begin with the discussion of some earlier research that involved inner cores. After that, boundary conditions for inner cores are discussed. The aim of this chapter is to investigate the effect of an inner core on the convergence level of our previous models. To achieve this aim, we conduct numerical experiments and present the results for insulating and conducting cores. We conclude this chapter by showing that a simple modification of the PAS flow allows us to fully planarize it inside a spherical shell.

In Chapter 5, we introduce two new modification of PAS-like flows which we label biPAS and quasiPAS flows. These PAS-like flows have the advantage that they may be fully planarized inside a sphere. We present numerical results for biPAS and quasiPAS flows including partly and fully planarized versions.

The convergence of planar velocity dynamos is closely examined in Chapter 6. We compare the sensitivity of various conventional tests and several new tests which we define. Later, we apply all of the convergence tests to Y_2^2 models and discuss the results.

To conclude this thesis, in Chapter 7 we summarize all of our results and make suggestions for future work.

Chapter 2

Kinematic Dynamo Theory

2.1 Geomagnetic Field

As an introduction, we try to explain the history of the geomagnetic field. We will start by discussing the earliest studies, the reversal behaviour and the source of the geomagnetic field. Most information in this section is taken from Merrill, McElhinny and McFadden (1996).

It is generally believed that the geomagnetic field, the so-called main field, has existed for around 2.7 billion years. *De Magnete* (Gilbert, 1600) is probably the first publication which contains a comprehensive description of the main field. This book was written by William Gilbert in 1600, physician for Queen Elizabeth I and President of the Royal College of Physicians, and contains his thoughts and investigations on magnetism over many years (Malin, 1987). In an experiment, Gilbert used a spherical magnet (Figure 2.1), made from a lodestone, and observed the magnetic force's direction over its surface. Gilbert concluded that the Earth itself is a huge magnet and thought that there was a permanent magnet inside the Earth.

The recognition of the main field began many years before *De Magnete*'s time. It started with observations on magnets by the Greek philosopher Thales in the sixth century B.C and was followed by Chinese literature between the third century B.C. and the sixth century A.D. The first discussion of a compass was written by Shen Kua, a Chinese scientist, in the eleventh century A.D. (Rikitake and Honkura, 1985). Apparently, the Chinese people had used compasses since early in the twelfth century (Rikitake and Honkura, 1985). Meanwhile, it is believed that Arabs brought compasses into Europe during the twelfth century by sea route. Moreover, in 1190 an English monk, Alexander Neckham, wrote what is considered to be the earliest European article on compasses.

Shen Kua observed that the compass needle does not point to exact geographical north. Such a phenomenon is called compass error or declination. In 1510, Georg

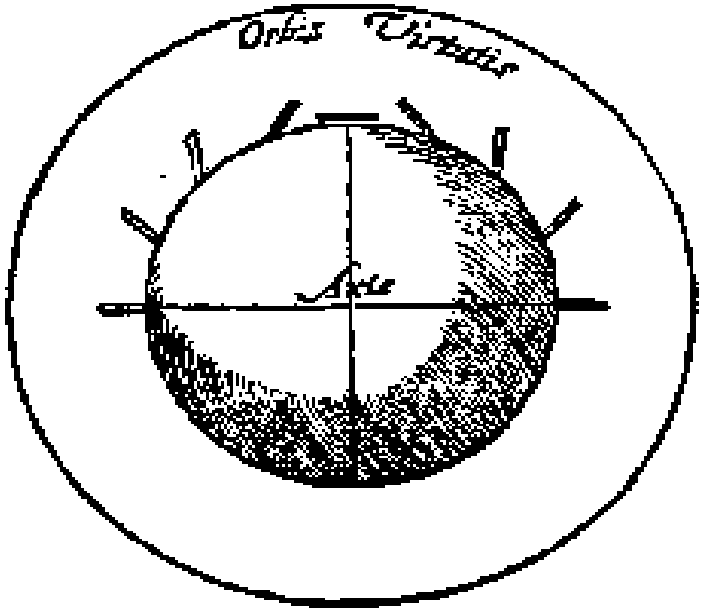

Figure 2.1: Model spherical lodestone of Gilbert (1600). Gilbert used this lodestone to observe the direction of magnetic force.

Hartmann, a Nuremberg priest, observed the declination and published his work in Rome. He also found the magnetic inclination, the dip of a compass needle, in Konigsberg in 1544. In 1576, Robert Norman in England rediscovered Hartmann's result. Henry Gellibrand, Professor of astronomy at Gresham college, observed the change in the magnetic inclination in 1634. Earlier, Edmund Gunter had observed inclination in 1622, but thought it was due to measurement errors.

When rocks are formed from lava, they became magnetized in the direction of the local main field. This magnetization is called the natural remanent magnetization (Rikitake and Honkura, 1985). Palaeogmagnetism, a study of the past main field, is based on the observation of the magnetic direction in rocks. From this study, the reversal behaviour of the main field was discovered. Reversal behaviour is also found in the magnetic field of the Sun.

The study of palaeomagnetism was initiated in 1904 by David, followed by Brunhes in 1906. They discovered that magnetic directions in lava flows differ from that of the present main field. The discovery was confirmed by Matuyama in 1929. He observed more than 100 lava flows from Japan and Manchuria and found similar phenomena. However, in 1955 Néel proposed a self reversal theory for magnetized rocks leading to some uncertainty concerning the reversal of the main field. In contrast, Wilson (1962a, 1962b) observed the magnetic direction of doubly baked and baked contact rocks. From these experiments, he concluded that his results could only be explained by the reversal of the main field.

If rocks preserve the polarity of the past main field, we can determine the period of

the reversal of the main field. Mercanton, in 1926, suggested that this period must be recorded in rocks around the world. Later, many scientists tried to produce a geomagnetic polarity time scale. One such time scale was made by Cande and Kent in 1995. In this time scale, they present the geomagnetic polarity for the past 160 Ma. However, the first scale that covers the geomagnetic polarity for the past 160 Ma was probably produced by Kent and Gradstein in 1986. Figure 2.2 contains a geomagnetic polarity time scale which is a combination of the work by Cande and Kent in 1995 and Kent and Gradstein in 1986.

Long after Gilbert had proposed that there is a huge magnet inside the Earth, Blackett conjectured in 1947 that all huge rotating bodies might possess magnetic fields. He could not explain his hypothesis theoretically and tried unsuccessfully to provide experimental evidence. Later, Inglis (1955) found that Blackett's hypothesis cannot be applied to the Earth because of it's high temperature and pressure. Other researchers proposed different hypotheses about the source of the main field. For example, Hollenbach and Herndon (2001) suggested that the main field may be produced by a nuclear fission reactor inside the Earth.

However, most scientists believe that the main field is produced by a self-excited dynamo process as proposed by Larmor (1919). He proposed that there is an interaction between a moving electrically conducting fluid and magnetic field inside the Earth. Such interaction generates electric currents that may maintain the magnetic field. Larmor's concept is supported by seismic evidence on the structure of the Earth's interior. It is believed that the Earth has two cores. The inner core, with a radius of about 1,220 km, is probably solid. Meanwhile, the outer core, with a radius of about 3,480 km, is mostly comprised of electrically conducting fluid which consists of iron and other light elements, possibly silicon, oxygen, and sulfur.

2.2 Dynamo Theory

One example of a self-excited dynamo is the disk dynamo invented by Michael Faraday. Bullard (1955) investigated three types of disk dynamos: frictionless, viscous free and an externally loaded disk dynamo. He reported that these dynamos can maintain a magnetic field. However, no-sign of reversal was found. He predicted that a more complicated disk dynamo might have reversal behaviour.

Following Bullard's suggestion, Rikitake (1958) investigated a coupled disk dynamo as depicted in Figure 2.3. Bullard (1949) suggested that there are at least four phases of induction required to produce the main field. Rikitake thought a series of disk dynamos could produce a similar field with reversal behaviour. Rikitake's system (Figure 2.3) is governed by

$$L_1 \frac{\mathrm{d}I_1}{\mathrm{d}t} + R_1 I_1 = \omega_1 M_1 I_2$$

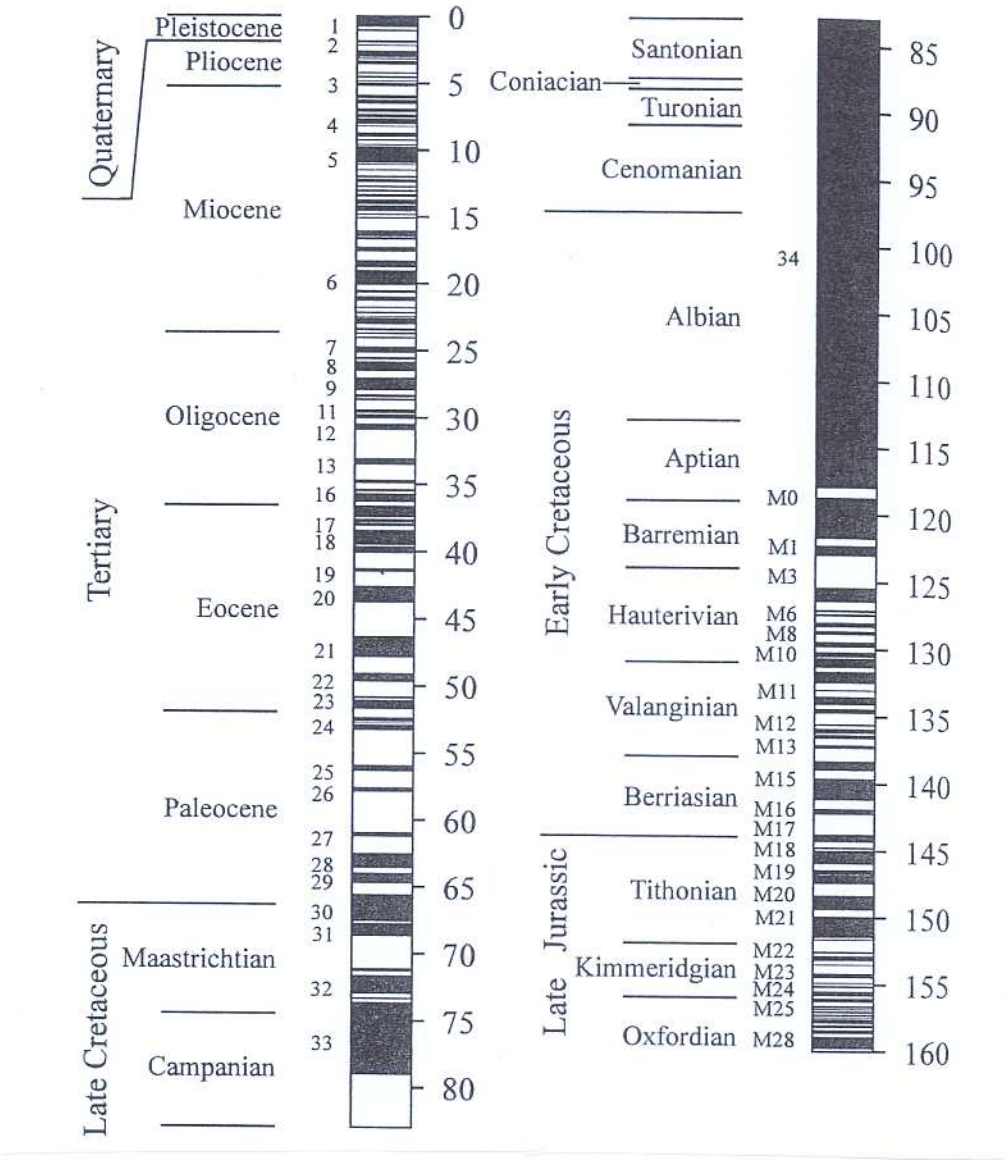

Figure 2.2: A combination of Kent and Gradstein (1986) and Cande and Kent (1995) geomagnetic polarity time scales. This picture is taken from Merrill et al (1996).

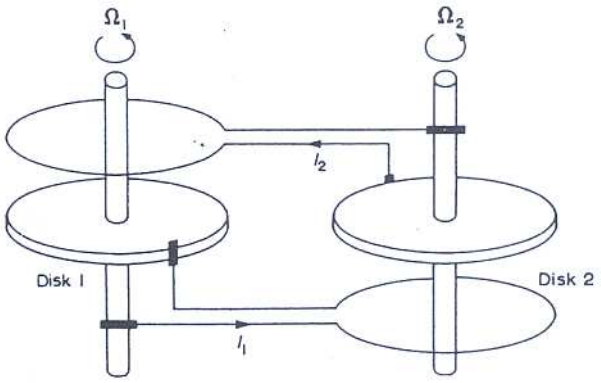

Figure 2.3: Model coupled disk dynamo of Rikitake (1954). This system is able to show reversal of a magnetic fields.

$$L_2\frac{\mathrm{d}I_2}{\mathrm{d}t} + R_2 I_2 = \omega_2 M_2 I_1$$
$$C_1\frac{\mathrm{d}\omega_1}{\mathrm{d}t} = G_1 - M_1 I_1 I_2$$
$$C_2\frac{\mathrm{d}\omega_2}{\mathrm{d}t} = G_2 - M_2 I_1 I_2,$$

where L is the self-inductance of the coil, R is the resistance of the coil, I is the electric current, M is the mutual inductance between the coil and the periphery of the disk, ω denotes the angular velocity, C indicates the moment of inertia of the disk around the axle and G is the torque. Rikitake (1958) considered a two disk system with

$$L_1 = L_2,\ R_1 = R_2,\ I_1 = I_2,\ M_1 = M_2,\ C_1 = C_2,\ G_1 = G_2,$$

and solved the resulting dimensionless differential equations numerically. He found that the electric current did reverse which indicates reversal of the magnetic field.

Although it shows reversal behaviour, this disk dynamo is not an accurate model for the Earth's dynamo. On the other hand, magnetohydrodynamics (MHD) is a good model for the Earth's dynamo since the outer core is a fluid. In MHD, we need to simultaneously solve: the induction equation, the Navier-Stokes equation, the mass conservation equation, Poisson's equation for gravity, the heat equation and an equation of state (Merrill, McElhinny and McFadden, 1996).

Solution of MHD problems is very difficult, requiring high level mathematical analysis and a huge amount of calculation. However, a comprehensive numerical investigation has been successfully performed by Glatzmaier and Roberts (1995). Their model shows reversal behaviour as seen in the Earth's reversal record. The decay rate of the magnetic field is also similar to the Earth's one. They discovered that

the conducting fluid in the outer core attempted to reverse the field continuously but the inner core discouraged the process since the field required a longer time to reverse in the inner core.

In this work, we only consider the kinematic dynamo problem where the flow is specified and the induction equation is solved for the magnetic field. Despite the simplification, this problem still requires extensive computations.

2.3 Kinematic Dynamo Theory

To define the kinematic dynamo problem, we start with the pre-Maxwell equations:

$$\nabla \times \mathbf{B} = \mu \mathbf{j}, \tag{2.1}$$
$$\nabla \cdot \mathbf{B} = 0, \tag{2.2}$$
$$\nabla \times \mathbf{E} = -\partial \mathbf{B}/\partial t, \tag{2.3}$$
$$\nabla \cdot \mathbf{E} = \mathscr{I}/\varepsilon, \tag{2.4}$$

where $\mathbf{B}$ is the magnetic induction field, $\mathbf{E}$ is the electric field, $\mathbf{j}$ is the electric current density, μ is the permeability, $\mathscr{I}$ is the charge density and ε is the dielectric constant. Equation (2.1) is referred to as the quasi-steady approximation which is valid when $\mathcal{L}/\tau \ll c$. τ is the time scale of the variation in field. $\mathcal{L}$ is the length scale of the system and c is the velocity of light in a vacuum. A more detailed discussion is presented in Roberts (1967). We also need Ohm's law for a moving conductor,

$$\mathbf{j} = \sigma(\mathbf{E} + \mathbf{v} \times \mathbf{B}), \tag{2.5}$$

where σ is the electrical conductivity and $\mathbf{v}$ is the velocity of the conductor. Using equations (2.1–2.3) and vector identities, we can recast Ohm's law as

$$\partial \mathbf{B}/\partial t = \nabla \times (\mathbf{v} \times \mathbf{B}) + \eta \nabla^2 \mathbf{B}, \tag{2.6}$$

where $\eta = 1/\mu\sigma$, is the magnetic diffusivity. Equation (2.6) is the induction equation.

In this work, the conducting fluid occupies finite spherical volume V, and has an incompressible time-dependent flow i.e.

$$\nabla \cdot \mathbf{v} = 0. \tag{2.7}$$

Outside the sphere is an insulating environment $\widehat{V}$, where

$$\nabla \times \widehat{\mathbf{B}} = 0, \tag{2.8}$$
$$\nabla \cdot \widehat{\mathbf{B}} = 0, \tag{2.9}$$
$$\nabla \times \widehat{\mathbf{E}} = -\partial \widehat{\mathbf{B}}/\partial t, \tag{2.10}$$
$$\nabla \cdot \widehat{\mathbf{E}} = 0. \tag{2.11}$$

Having no current source in $\widehat{V}$ implies

$$|\widehat{\mathbf{B}}| = \mathcal{O}(1/r^3), \text{ as } r \to \infty. \tag{2.12}$$

$\mathbf{B}$ is continuous across the boundary, Σ, of V i.e.

$$[\mathbf{B}] = 0, \text{ across } \Sigma, \tag{2.13}$$

where $[Q]$ refers to the jump in Q across Σ. On Σ, $\mathbf{v}$ satisfies the rigid boundary condition

$$\mathbf{n} \cdot \mathbf{v} = 0, \tag{2.14}$$

where $\mathbf{n}$ is the unit normal, and sometimes the no-slip condition

$$\mathbf{v} = \mathbf{0}. \tag{2.15}$$

The non-dimensionalized form of the induction equation is

$$\frac{\partial \mathbf{B}}{\partial t} = R\nabla \times (\mathbf{v} \times \mathbf{B}) + \nabla^2 \mathbf{B}, \tag{2.16}$$

where $R = UL/\eta$ is the magnetic Reynolds number, U is a characteristic velocity, L is the radius of the sphere, and time is measured in units of the diffusion time (L^2/η).

2.3.1 The Spectral Form of the Induction Equation

We expand $\mathbf{B}$ and $\mathbf{v}$ in poloidal-toroidal form, using scalar fields S, T and s, t, respectively:

$$\mathbf{B} = \mathbf{S} + \mathbf{T} = \nabla \times \nabla \times (S\mathbf{r}) + \nabla \times (T\mathbf{r}), \tag{2.17}$$

$$\mathbf{v} = \mathbf{s} + \mathbf{t} \ = \nabla \times \nabla \times (s\mathbf{r}) + \nabla \times (t\mathbf{r}); \tag{2.18}$$

and expand S, T in spherical harmonics

$$\begin{aligned} S &= \sum_{n,m} S_n^m(r,t) Y_n^m(\theta,\phi), \\ T &= \sum_{n,m} T_n^m(r,t) Y_n^m(\theta,\phi), \end{aligned} \tag{2.19}$$

and similarly for s, t, where $m = -n, ..., n$ and $n = 1, 2, 3, ...$ In the above equation,

$$Y_n^m = (-)^m \left[\frac{2n+1}{2-\delta_m^0}\right]^{\frac{1}{2}} P_n^m(\cos\theta) e^{\mathrm{i}m\phi} = (-)^m \overline{Y_n^{-m}}, \tag{2.20}$$

where P_n^m is the Schmidt-normalized Legendre function defined by

$$P_n^m(\mu) = \left[\frac{(2-\delta_m^0)(n-m)!}{(n+m)!}\right]^{\frac{1}{2}} \frac{(1-\mu^2)^{m/2}}{2^n n!} \left[\frac{\mathrm{d}}{\mathrm{d}\mu}\right]^{n+m} (\mu^2-1)^n. \tag{2.21}$$

The overbar $\overline{(...)}$ means complex conjugate and δ_m^0 is the Kronecker delta. We will use n_1, n_2, n_3 notation instead of BG's notation (α, β, γ) and drop the m superscripts when possible. Our definition of $\mathbf{T}$ and $\mathbf{S}$ differs slightly from that of BG, who used

$$\begin{aligned}\mathbf{S} &= \nabla \times \nabla \times (S\mathbf{e_r}),\\ \mathbf{T} &= \nabla \times (T\mathbf{e_r}).\end{aligned}$$

The spectral form of equation (2.16) is

$$\begin{aligned}\left(\frac{\partial}{\partial t} - D_{n_3}\right) S_{n_3} &= R\sum_{n_1 n_2}[(t_{n_1} S_{n_2} S_{n_3}) + (s_{n_1} T_{n_2} S_{n_3}) + (s_{n_1} S_{n_2} S_{n_3})],\\ \left(\frac{\partial}{\partial t} - D_{n_3}\right) T_{n_3} &= R\sum_{n_1 n_2}[(t_{n_1} T_{n_2} T_{n_3}) + (t_{n_1} S_{n_2} T_{n_3}) + (s_{n_1} T_{n_2} T_{n_3})\\ &\quad + (s_{n_1} S_{n_2} T_{n_3})],\end{aligned} \tag{2.22}$$

where

$$D_n \equiv \frac{\partial^2}{\partial r^2} + \frac{2}{r}\frac{\partial}{\partial r} - \frac{n(n+1)}{r^2}.$$

The interactions in equations (2.22) are

$$(t_{n_1} S_{n_2} S_{n_3}) = \frac{n_2(n_2+1)}{4\pi r n_3(n_3+1)}(-)^{m_3} E t_{n_1} S_{n_2}, \tag{2.23}$$

$$(s_{n_1} T_{n_2} S_{n_3}) = \frac{n_1(n_1+1)}{4\pi r n_3(n_3+1)}(-)^{m_3} E s_{n_1} T_{n_2}, \tag{2.24}$$

$$(t_{n_1} T_{n_2} T_{n_3}) = (-)^{m_3} E t_{n_1} T_{n_2}/4\pi r, \tag{2.25}$$

$$\begin{aligned}(s_{n_1} S_{n_2} S_{n_3}) =& \Big\{ n_1(n_1+1)[n_1(n_1+1) - n_2(n_2+1) - n_3(n_3+1)]\frac{s_{n_1}}{r}\\ & S'_{n_2} + (n_1-n_2)(n_1+n_2+1)[n_1(n_1+1) + n_2(n_2+1)\\ & - n_3(n_3+1)]\frac{s_{n_1}}{r}\frac{S_{n_2}}{r} + n_2(n_2+1)[n_1(n_1+1)\\ & - n_2(n_2+1) + n_3(n_3+1)]\frac{S_{n_2}}{r} s'_{n_1}\Big\}\frac{(-)^{m_3} A}{8\pi n_3(n_3+1)}\end{aligned} \tag{2.26}$$

$$\begin{aligned}(t_{n_1} S_{n_2} T_{n_3}) =& \Big\{ n_3(n_3+1)[n_1(n_1+1) + n_2(n_2+1) - n_3(n_3+1)]\frac{t_{n_1}}{r}\\ & (\frac{S_{n_2}}{r} + S'_{n_2}) + n_2(n_2+1)[n_1(n_1+1) - n_2(n_2+1)\\ & + n_3(n_3+1)](t'_{n_1}\frac{S_{n_2}}{r} + \frac{t_{n_1}}{r} S'_{n_2})\Big\}\frac{(-)^{m_3} A}{8\pi n_3(n_3+1)},\end{aligned} \tag{2.27}$$

$$(s_{n_1} T_{n_2} T_{n_3}) = \Big\{ n_3(n_3+1)[n_3(n_3+1) - n_1(n_1+1) - n_2(n_2+1)]\frac{T_{n_2}}{r}$$

$$
\begin{aligned}
&(\frac{s_{n_1}}{r}+s'_{n_1})+n_1(n_1+1)[n_1(n_1+1)-n_2(n_2+1)\\
&-n_3(n_3+1)](T'_{n_2}\frac{s_{n_1}}{r}+\frac{T_{n_2}}{r}s'_{n_1})\Big\}\frac{(-)^{m_3}A}{8\pi n_3(n_3+1)}, \qquad (2.28)\\
(s_{n_1}S_{n_2}T_{n_3})=&\Big\{[n_1(n_1+1)+n_2(n_2+1)+n_3(n_3+1)]\frac{s_{n_1}}{r}\frac{S_{n_2}}{r^2}\\
&-n_1(n_1+1)\frac{s_{n_1}}{r}S''_{n_2}-[n_1(n_1+1)+n_2(n_2+1)\\
&-n_3(n_3+1)](S'_{n_2}\frac{s_{n_1}}{r^2}+\frac{s'_{n_1}}{r}S'_{n_2}+\frac{S_{n_2}}{r^2}s'_{n_1})\\
&-n_2(n_2+1)s''_{n_1}\frac{S_{n_2}}{r}\Big\}\frac{(-)^{m_3}E}{4\pi n_3(n_3+1)}, \qquad (2.29)
\end{aligned}
$$

where

$$
\begin{aligned}
A&=\int_{4\pi}Y_{n_1}^{m_1}Y_{n_2}^{m_2}Y_{n_3}^{-m_3}\sin\theta\mathrm{d}\theta\mathrm{d}\phi,\\
E&=\int_{4\pi}\left(\frac{\partial Y_{n_1}^{m_1}}{\partial\theta}\frac{\partial Y_{n_2}^{m_2}}{\partial\phi}-\frac{\partial Y_{n_1}^{m_1}}{\partial\phi}\frac{\partial Y_{n_2}^{m_2}}{\partial\theta}\right)Y_{n_3}^{-m_3}\mathrm{d}\theta\mathrm{d}\phi,
\end{aligned}
\qquad (2.30)
$$

and $S'=\mathrm{d}S/\mathrm{d}r$, $S''=\mathrm{d}^2S/\mathrm{d}r^2$, A is the Adams integral and E is the Elsasser integral. The spectral form of the induction equation in the present formalism was considered by James (1974), and will be referred to herein as the complex Y-form. The alternative BG form of the interactions can be seen in BG and Dudley (1988).

In solving equation (2.16), we need to satisfy

$$T_n=S_n=0,\ \text{ at } r=0, \qquad (2.31)$$

$$T_n=\frac{\partial S_n}{\partial r}+(1+n)S_n=0,\ \text{ at } r=1. \qquad (2.32)$$

Equation (2.31) results from the differentiability of $\mathbf{B}$ with respect to x,y,z at $r=0$ (discussed in more detail in §2.3.4). Boundary condition (2.32) reflects the current free nature of $\widehat{V}$ and the vanishing of $\mathbf{B}$ as $r\to\infty$. The spectral form of the rigid boundary condition (2.14) is

$$s_n=0,\ \text{ at } r=1, \qquad (2.33)$$

and the no-slip condition (2.15) is

$$t_n=\frac{\partial s_n}{\partial r}=0,\ \text{ at } r=1. \qquad (2.34)$$

2.3.2 Numerical Method

For a successful dynamo, we need to have a growing solution $\mathbf{B}$ of the induction equation (2.16). In general, it is impossible to solve the induction equation unless

we truncate the expansion of $\mathbf{B}$ and $\mathbf{v}$ in poloidal-toroidal forms (2.17), (2.18) at some degree $n = N$. In the radial direction, we divide the interval $0 \leq r \leq 1$ into J equal subintervals. We call a pair of N and J the truncation level, $[J, N]$. The solutions are meaningless unless they converge for increasing N and J.

Since $\mathbf{v}$ is time dependent, we may seek the solution in the form

$$\mathbf{B}(\mathbf{r}, t) = \sum_{\lambda} \mathbf{B}_{\lambda}(r, \theta, \phi) e^{\lambda t},$$

assuming non-degeneracy of the problem. We use the second order central difference schemes,

$$f_j' = \frac{(f_{j+1} - f_{j-1})}{2h} + O(h^2), \tag{2.35}$$

$$f_j'' = \frac{(f_{j+1} - 2f_j + f_{j-1})}{h^2} + O(h^2), \tag{2.36}$$

in the radial direction, where $h = 1/J$. This method requires the third derivative of f_j to be continuous, i.e. $f_j \in C^{(3)}(r)$. $C^{(p)}(r)$ means p times continuously differentiable with respect to r. Equations (2.22) are second order coupled differential equations and s_n'', t_n' are the highest s, t derivatives in the coefficients of S, T in the interaction terms (2.23)–(2.29). It follows that $S, T \in C^{(3)}(r)$ if

$$s_n'', t_n' \in C^{(1)}(r). \tag{2.37}$$

This is true for all flows where (2.35) and (2.36) are used numerically in this thesis. The spectral form (2.22) then reduces to an ordinary eigenvalue problem

$$\mathbf{A}\mathbf{x} = \lambda \mathbf{x}, \tag{2.38}$$

where A is a banded matrix. Our aim is to find λ such that real part of $\lambda \geq 0$, which implies the existence of a successful dynamo. For each R, we let $\lambda_{\max}$ denote the λ with maximum real part, i.e. representing the slowest decaying or fastest growing mode.

Earlier researchers had difficulty in increasing $[J, N]$ due to computer limitations. Dudley (1988) stated that BG and Lilley (1970) used insufficient $[J, N]$, which led them to erroneous conclusions. In particular, Lilley had s'' discontinuous at $r = 0.5$, which significantly hinders convergence since (2.37) is invalid there. Although more sophisticated computers, in terms of memory and speed, are now available, we still need to ensure that we use sufficiently high $[J, N]$ to indicate convergence.

There are at least three methods to increase $[J, N]$. The first one is by constructing a sparse banded matrix so that we only need to store the band of the matrix. In order to do that, we define

$$F_{nj} = [S_n^{-n}, S_n^{-n+1}, \ldots, S_n^n, T_n^{-n}, \ldots, T_n^n],$$

at grid point $r = jh$ and arrange the elements of the eigenvector $\mathbf{x}$ in (2.38) in the following order,

$$\mathbf{x} = (F_{11}, F_{21}, \ldots, F_{N1}, F_{12}, F_{22}, \ldots, F_{N2}, \ldots, F_{1J}, F_{2J}, \ldots, F_{NJ}).$$

The boundary values F_{nJ}, $n = 1, ..., N$, only consist of S contributions due to the boundary conditions (2.32).

The second method is by choosing an appropriate $\mathbf{v}$ so that the $\mathbf{B}-$harmonics decouple into two or more independent sets. Each of these sets can be investigated separately. We give a more detailed discussion about this method in §2.3.3.

The last method involves dividing the matrix into sub-bands and processing one sub-band at a time. Details of this method are given in Chapter 3. If applicable, we can obtain even higher $[J, N]$ by combining two or more of the above methods.

In solving the eigenvalue problem in equation (2.38), we need to choose an appropriate method to preserve the structure of the matrix. If the band structure is destroyed then we will need to store a larger matrix. Consequently, the optimum $[J, N]$ cannot be achieved. Considering this, we choose the inverse iteration method to solve our problem because it is known that this method may be programmed to preserve the band structure.

2.3.3 Selection Rules

The interaction terms on the right side of the spectral form (2.22) consist of either Adams or Elsasser integrals. These integrals are zero unless some selection rules are satisfied. James (1974) showed that these integrals are proportional to Wigner $3-j$ coefficients. From the Wigner $3-j$ coefficient, we can obtain the following selection rules:

SR1: $(s_{n_1} S_{n_2} S_{n_3})$, $(s_{n_1} T_{n_2} T_{n_3})$, and $(t_{n_1} S_{n_2} T_{n_3})$ depend on A and are zero unless $n_1 + n_2 + n_3$ is even, and $|n_1 - n_2| \leq n_3 \leq n_1 + n_2$.

SR2: $(s_{n_1} T_{n_2} S_{n_3})$, $(s_{n_1} S_{n_2} T_{n_3})$, $(t_{n_1} S_{n_2} S_{n_3})$, and $(t_{n_1} T_{n_2} T_{n_3})$ depend on E and are zero unless $n_1 + n_2 + n_3$ is odd, and $|n_1 - n_2| < n_3 < n_1 + n_2$.

SR3: $(s_{n_1} S_{n_2} S_{n_3}), \ldots, (t_{n_1} T_{n_2} T_{n_3})$ are all zero unless $m_3 = m_1 + m_2$.

Using SR1 and SR2, we can reduce the size of the matrix. This gives a large computational saving. If the degree of harmonics of s_{n_1} is even and the degree of harmonics of t_{n_1} is odd, we can separate $\mathbf{B}$ into dipole (D) and quadrupole (Q) parities

$$\begin{aligned} \text{D:} \quad & S_1^0, S_1^1, T_2^0, T_2^1, T_2^2, S_3^0, S_3^1, S_3^2, S_3^3, T_4^0, T_4^1, T_4^2, T_4^3, T_4^4, \ldots \\ \text{Q:} \quad & T_1^0, T_1^1, S_2^0, S_2^1, S_2^2, T_3^0, T_3^1, T_3^2, T_3^3, S_4^0, S_4^1, S_4^2, S_4^3, S_4^4, \ldots \end{aligned} \tag{2.39}$$

where S_n^m denotes the presence of S_n^m and its conjugate, S_n^{-m}, and similarly for T. Each parity has its own solution and can be investigated independently. Furthermore, BIJ showed that the presence of s_{odd} or t_{even} prohibits the possibility of having

D or Q parity. Their argument can be seen in Table 1 of BIJ. In this work, we are going to call the separation (2.39) the DQ-decoupling.

Besides the DQ-decoupling, BIJ also decoupled **B** using SR3. If the orders of harmonics of the flow satisfy

$$m_1 = 0 \bmod k$$

for some integer k, then **B** can be separated into independent chains and each chain can be investigated separately. In these chains, the orders of the harmonics satisfy

$$m = l \bmod k \text{ or } m = (l-k) \bmod k, l = 1, 2, ..., k$$

We label these chains Mlk and call this m-decoupling. For example, if $k = 2$, we have 2 different chains:

$$\begin{aligned}
\text{M02}: &\quad S_1^0, T_1^0, S_2^0, T_2^0, S_2^2, T_2^2, S_3^0, T_3^0, S_3^2, T_3^2, S_4^0, T_4^0, S_4^2, T_4^2, S_4^4, T_4^4, \ldots \\
\text{M12}: &\quad S_1^1, T_1^1, S_2^1, T_2^1, S_3^1, T_3^1, S_3^3, T_3^3, S_4^1, T_4^1, S_4^3, T_4^3, S_5^1, T_5^1, S_5^3, T_5^3, \\
&\quad S_5^5, T_5^5, \ldots
\end{aligned}$$

Sometimes, we can combine the DQ and m decouplings to get a smaller matrix. For example, if we can use D parity and m-decoupling with $k = 2$, then we will have the following independent chains:

$$\begin{aligned}
\text{DM02}: &\quad S_1^0, T_2^0, T_2^2, S_3^0, S_3^2, T_4^0, T_4^2, T_4^4, S_5^0, S_5^2, S_5^4, T_6^0, T_6^2, T_6^4, T_6^6, \ldots \\
\text{DM12}: &\quad S_1^1, T_2^1, S_3^1, S_3^3, T_4^1, T_4^3, S_5^1, S_5^3, S_5^5, T_6^1, T_6^3, T_6^5, \ldots
\end{aligned}$$

A more detailed discussion can be found in BIJ(2006).

2.3.4 Differentiability Conditions

In general, if we want to solve the induction equation (2.16), then **B** and **v** have to satisfy differentiability conditions. According to Friedman (1964), if $\mathbf{v} \in C^{(p)}(x, y, z)$ then $\mathbf{B} \in C^{(p+1)}(x, y, z)$. Here, $C^{(p)}(x, y, z)$ means p times continuously differentiable with respect to x, y, z. As a minimal condition, **B** needs to be in $C^{(2)}(x, y, z)$ to satisfy the induction equation. This will be true if $\mathbf{v} \in C^{(1)}(x, y, z)$. For other purposes, **B** may need a higher level of differentiability as discussed in detail by Dudley (1988).

It is known (Hobson, 1931) that $r^n Y_n$ is a homogeneous multinomial of degree n in x, y, z and hence infinitely differentiable. It follows that if

$$s_n^m = r^n(a_0 + a_2 r^2 + a_4 r^4 + a_6 r^6 + \ldots), \tag{2.40}$$

$$t_n^m = r^n(a_0 + b_2 r^2 + b_4 r^4 + b_6 r^6 + \ldots), \tag{2.41}$$

then **v** is infinitely differentiable with respect to x, y, z, and this will ensure any higher differentiability requirement of **B** (e.g. as required if Richardson extrapolation

is used). If (2.40) and (2.41) are not satisfied, then the point $r = 0$ is problematic, since the (x, y, z) higher derivatives of $\mathbf{v}$ may be multivalued or infinite, and this may lead to convergence or other numerical problems.

Several early authors (e.g. BG, KR, Gubbins (1973)) used flows that violated (2.40) and (2.41). However, their numerical results are acceptable because $r = 0$ is not used in the computations, and the s, t radial derivatives used in (2.37) and the spectral form of the induction equations (2.22), are well behaved. (The discontinuity in s'' in the model of Lilley occurs at $r = 0.5$ and has been discussed in §2.3.2 earlier.) In the new models introduced in this thesis, we require (2.40) and (2.41), which ensure infinite differentiability, even at $r = 0$.

2.4 Anti-dynamo Theorems

Besides the Cowling theorem, a number of other anti-dynamo theorems have been proven. Examples include: the toroidal velocity theorem (BG) and the radial velocity theorem (Namikawa and Matsushita, 1970). A common characteristic of these theorems is that the magnetic field decouples in some fashion. It has been occasionally conjectured that if the toroidal and poloidal components of the magnetic field decouple, then the magnetic field will decay (See references in Ivers and James, 1988 IJ).

IJ discussed 4 different conditions that can decouple the magnetic field: (i) $\mathbf{B}$ and $\mathbf{v}$ are axisymmetric about the same axis, (ii) $\mathbf{B}$ and $\mathbf{v}$ are independent of any one of the cartesian coordinates, (iii) the radial component of $\mathbf{v}$ is independent of θ and ϕ, and (iv) one of the cartesian components is independent of x_j $(i \neq j)$.

A special case of (iv) is the planar velocity theorem. In this theorem, one of the velocity components is zero. Hence, it is independent of all coordinates. This theorem is the subject of our present work. We will discuss it in more detail in the next section.

2.4.1 Planar Velocity Theorem

The Planar Velocity Theorem (PVT) is an analogue of the Toroidal Velocity Theorem (BG) in cartesian coordinates. The PVT precludes the existence of a dynamo process made by an incompressible flow lacking one cartesian component. Here, we assume that the flow has no z-component.

Theorem *The Planar Velocity Theorem: if* $\mathbf{v} \cdot \mathbf{e}_z = 0$*, then* $|\mathbf{B}| \to 0$ *as* $t \to \infty$*.*

The PVT was considered by Zel'dovich (1957). He discussed the theorem in the con-

text of two-dimensional turbulence. Later, Lortz (1968) provided a proof. However, Moffat considered Lortz's proof is weaker than that of Zel'dovich. Moffat (1978) gave a similar proof to Zel'dovich. In all of these proofs, it was assumed that the conductor occupies all space.

Recently, BIJ gave a more detailed proof of the PVT as below
Proof :
Firstly, we assume that an incompressible flow fills an infinite volume V_∞ and satisfies:

$$\mathbf{v} = \nabla f \times \mathbf{e}_z. \tag{2.42}$$

We dot product equation (2.6) with $\mathbf{e}_z$ to get the z-component of the induction equation

$$\frac{\partial B_z}{\partial t} = -\mathbf{v}\cdot\nabla B_z + \eta\nabla^2 B_z. \tag{2.43}$$

Now, we multiply the above equation with B_z, integrate over a spherical volume V_r of radius r and surface Σ, and apply the divergence theorem to get

$$\begin{aligned}\frac{\mathrm{d}}{\mathrm{d}t}\int_{V_r}\frac{1}{2}B_z^2\mathrm{d}V = &-\int_\Sigma \frac{1}{2}B_z^2\mathbf{v}\cdot\mathrm{d}\mathbf{\Sigma} + \eta\int_\Sigma B_z\nabla B_z\cdot\mathrm{d}\mathbf{\Sigma}\\ &-\eta\int_{V_r}(\nabla B_z)^2\mathrm{d}V,\end{aligned} \tag{2.44}$$

where $\mathrm{d}\mathbf{\Sigma} = \mathbf{e}_r\mathrm{d}\Sigma = \mathbf{e}_r r^2\sin\theta\mathrm{d}\theta\mathrm{d}\phi$ is the surface differential pointing outward. Provided $\mathbf{v}, B_z \to 0$ sufficiently fast as $r\to\infty$, we let $r\to\infty$ to get

$$\begin{aligned}\frac{\mathrm{d}}{\mathrm{d}t}\int_{V_\infty}\frac{1}{2}B_z^2\mathrm{d}V &= -\eta\int_{V_\infty}(\nabla B_z)^2\mathrm{d}V\\ &\le 0\end{aligned} \tag{2.45}$$

Equation (2.45) indicates that either B_z is decaying in time or $B_z\equiv 0$. We need to show that B_x and B_y also decay. We introduce scalars ϕ and Φ such that

$$\begin{aligned}B_x &= \frac{\partial\Phi}{\partial y} + \frac{\partial\phi}{\partial x}\\ B_y &= -\frac{\partial\Phi}{\partial x} + \frac{\partial\phi}{\partial y}.\end{aligned} \tag{2.46}$$

Applying (2.2) to (2.46) gives

$$\nabla_2^2\phi = -\frac{\partial B_z}{\partial z}, \tag{2.47}$$

where

$$\nabla_2^2 = \frac{\partial^2}{\partial x^2} + \frac{\partial^2}{\partial y^2}.$$

Equation (2.47) yields

$$\phi = -\frac{1}{2\pi}\int\log|\mathbf{r}-\mathbf{r}'|\left(\frac{\partial B_z}{\partial z}\right)'\mathrm{d}x'\mathrm{d}y', \tag{2.48}$$

where the integral is over the plane $z' = z$. From the last equation, we can conclude that $\phi \equiv 0$ or decays in time because B_z decays. As a result, $\mathbf{B} = \nabla \times (\Phi \mathbf{e_r})$ as $t \to \infty$. If we let $t \to \infty$ and uncurl the equation (2.6) then we have

$$\frac{\partial \Phi}{\partial t} = -\mathbf{v} \cdot \nabla \Phi + \eta \nabla^2 \Phi + \frac{\partial \psi}{\partial z}, \tag{2.49}$$

where $\psi = \psi(z, t)$. If we take the average of Φ over a disc A with radius ϖ at fixed z and apply the divergence theorem in the plane, then we get

$$\frac{\partial \overline{\Phi}}{\partial t} = \frac{1}{A} \int_C \left(\eta \frac{\partial \Phi}{\partial \varpi} - v_\varpi \Phi \right) \mathrm{d}C + \eta \frac{\partial^2 \overline{\Phi}}{\partial z^2} + \frac{\partial \psi}{\partial z}, \tag{2.50}$$

where C is the perimeter of the disk and

$$\overline{\Phi} = \frac{1}{A} \int_A \Phi \, \mathrm{d}A. \tag{2.51}$$

We can add to Φ a function of z without affecting B_x and B_y so that $\overline{\Phi}(\infty, z) = 0$. Now, if we let $\varpi \to \infty$ then $\partial \psi / \partial z = 0$. If we assume $\mathbf{v}, \Phi \to 0$ as $r \to \infty$ and use the same manipulation as for B_z, then we can recast equation (2.50) into

$$\frac{\mathrm{d}}{\mathrm{d}t} \int_{V_\infty} \Phi^2 \mathrm{d}V = -\eta \int_{V_\infty} (\nabla \Phi)^2 \mathrm{d}V.$$

The above equation implies $\Phi \equiv 0$ or Φ decays in time. Hence, B_x and B_y decay too.

Zel'dovich and Ruzmaikin (1980) gave a similar PVT proof. Furthermore, BIJ (2006) argued that the proof fails if the conducting fluid occupies a finite volume, such as a sphere, surrounded by insulating environment. We let $f^\pm$ represent the values on the inside $(-)$ and outside $(+)$ of Σ. If the flow satisfies boundary condition (2.33), then we can recast equation (2.44) into

$$\frac{\mathrm{d}}{\mathrm{d}t} \int_V \frac{1}{2} B_z^2 \mathrm{d}V = \eta \int_\Sigma (B_z \nabla B_z)^- \cdot \mathrm{d}\Sigma - \eta \int_V (\nabla B_z)^2 \mathrm{d}V, \tag{2.52}$$

provided $B_z = \mathcal{O}(1/r^3)$ as $r \to \infty$. We take the curl equation (2.8), apply the divergence theorem and take the z-component to get

$$\int_{\widehat{V}} (\nabla B_z)^2 \mathrm{d}V = -\int_\Sigma (B_z \nabla B_z)^+ \cdot \mathrm{d}\Sigma. \tag{2.53}$$

We combine equations (2.52) and (2.53) and use the continuity of B_z across Σ to get

$$\frac{\mathrm{d}}{\mathrm{d}t} \int_V \frac{1}{2} B_z^2 \mathrm{d}V = -\eta \int_\Sigma B_z \left[\frac{\partial B_z}{\partial r} \right] \cdot \mathrm{d}\Sigma - \eta \int_{V_\infty} (\nabla B_z)^2 \mathrm{d}V. \tag{2.54}$$

We cannot determine the first term of the right side of equation (2.54) since $\partial B_z / \partial r$ is, in general, discontinuous across Σ. Hence, we have no conclusion regarding the decay B_z. If we impose continuity on $\partial B_z / \partial r$ then we will overdetermine the problem, which may then have no solution.

Since the proof fails for a finite volume, BIJ(2006) investigated the PVT problem in a sphere numerically. They found one model, p1Y22DM12, that indicates the existence of non-decaying magnetic fields. They argued that maximum principles applied to equation (2.44) implied that the maximum of B_z must occur at the boundary $r = 1$ (Sperb, 1981). They therefore suggested that a flow with more shear near the boundary might give a better result. In this work, we continue their work in trying to definitely establish the existence of planar velocity dynamos.

2.5 Chapter Summary

The geomagnetic field is a key feature of the Earth. This field has existed for billions of years and reversed many times in the past. It is generally believed that the Earth's main magnetic field is caused by a self-excited dynamo. The first comprehensive discussion of the main field was written by William Gilbert in 1600. Later, Larmor (1919) proposed that there is a self-excited dynamo process inside the Earth that produces the main field. Recently, researchers have been trying to find an appropriate MHD model for this process.

The main subject of this thesis is the planar velocity theorem (PVT) which precludes magnetic field maintenance when the flow is parallel to a plane. The PVT was first proposed by Zel'dovich in 1957. Proofs of the PVT have been given by Lortz (1968) and Moffat (1978). However, these proofs assumed that the conducting fluid occupies all space. For a conductor in a finite volume, such as a sphere, no one has yet proven the PVT. BIJ (2006) argued that the proof fails for a finite conductor. Furthermore, they found one model that gives strong numerical evidence for the existence of planar velocity dynamos.

Chapter 3

Planar Velocity Dynamos

3.1 Formula for Planar Velocity Dynamos

A planar flow is a flow without one cartesian component. We assume a flow with no z-component, i.e.

$$\mathbf{v} = \nabla f \times \mathbf{e}_z. \tag{3.1}$$

As in the previous chapter, we expand the velocity field into toroidal and poloidal fields. Thus, we need to express a planar flow in the poloidal-toroidal form (2.18), which includes coefficients s_n^m, t_n^m. First, we define the following notation

$$\begin{aligned}\mathbf{T}\{g\} &= \nabla \times (g\mathbf{r}),\\ \mathbf{S}\{g\} &= \nabla \times \nabla \times (g\mathbf{r}),\end{aligned}$$

with properties

$$\begin{aligned}\nabla \times \mathbf{T}\{g\} &= \mathbf{S}\{g\},\\ \nabla \times \mathbf{S}\{g\} &= \mathbf{T}\{-\nabla^2 g\}.\end{aligned}$$

Expanding $f = \sum_{n,m} f_n^m Y_n^m$ in (3.1), using vector identities and dotting (2.18) with $\mathbf{r}$ gives

$$L^2 s_n^m Y_n^m = f_n^m \frac{\partial Y_n^m}{\partial \phi}, \tag{3.2}$$

where

$$\begin{aligned}L^2 Y_n^m &= -\left[\frac{1}{\sin\theta}\frac{\partial}{\partial\theta}\Big(\sin\theta\frac{\partial}{\partial\theta}\Big) + \frac{1}{\sin^2\theta}\frac{\partial^2}{\partial\phi^2}\right] Y_n^m,\\ &= n(n+1)Y_n^m.\end{aligned}$$

For simplicity, we frequently suppress the superscript m. Equation (3.2) implies

$$s_n = \frac{\mathrm{i}m}{n(n+1)} f_n. \tag{3.3}$$

To obtain the toroidal coefficient t_n^m of the flow, we take the curl of equation (2.18),

$$\nabla \times \mathbf{v} = \mathbf{S}\{t\} + \mathbf{T}\{-\nabla^2 s\}, \tag{3.4}$$

and then we dot equation (3.4) with $\mathbf{r}$ and make use of equation (3.1) to get:

$$\begin{aligned}
L^2 t &= \mathbf{r} \cdot \nabla \times \mathbf{v}, \\
&= \mathbf{r} \cdot \nabla \times (\nabla f \times \mathbf{e}_z), \\
&= \nabla \cdot ((\nabla f \times \mathbf{e}_z) \times \mathbf{r}), \\
&= \nabla \cdot (\mathbf{r} \cdot \nabla f)\mathbf{e}_z - \nabla \cdot (z \nabla f), \\
&= \frac{1}{r^2}\left(\frac{\partial}{\partial r} r^2 (r \cos\theta \frac{\partial f}{\partial r})\right) + \frac{1}{r \sin\theta}\frac{\partial}{\partial \theta}\left(-r \sin^2\theta \frac{\partial f}{\partial r}\right) \\
&\quad - \cos\theta \frac{\partial f}{\partial r} + \frac{\sin\theta}{r}\frac{\partial f}{\partial \theta} - r\cos\theta \nabla^2 f, \\
&= r\cos\theta \frac{\partial^2 f}{\partial r^2} - \sin\theta \frac{\partial^2 f}{\partial \theta \partial r} + \frac{\sin\theta}{r}\frac{\partial f}{\partial \theta} - r\cos\theta \nabla^2 f, \\
&= -2\cos\theta \frac{\partial f}{\partial r} + \frac{\cos\theta}{r} L^2 f + \frac{\sin\theta}{r}\frac{\partial}{\partial \theta}\Big(f - r\frac{\partial f}{\partial r}\Big).
\end{aligned} \tag{3.5}$$

Based on Chapman and Bartels (1962), we have the following recurrence relations:

$$\begin{aligned}
\cos\theta\, Y_n &= \alpha_{n+1} Y_{n+1} + \alpha_n Y_{n-1}, \\
\sin\theta \frac{\partial Y_n}{\partial \theta} &= n\alpha_{n+1} Y_{n+1} - (n+1)\alpha_n Y_{n-1},
\end{aligned}$$

where $\alpha_n := \sqrt{[(n^2 - m^2)/(4n^2 - 1)]}$. These relations are for surface harmonics as defined in equation (2.20). Using these relations, we obtain :

$$n(n+1)t_n = -(n+1)\alpha_n d_{1-n} f_{n-1} + n\alpha_{n+1} d_{n+2} f_{n+1}, \tag{3.6}$$

where $d_n := \mathrm{d}/\mathrm{d}r + n/r$. This implies that, for each f_n^m, there are two toroidal coefficients:

$$t_{n-1} = \frac{\alpha_n}{n}\, d_{n+1} f_n, \tag{3.7}$$

$$t_{n+1} = -\frac{\alpha_{n+1}}{n+1}\, d_{-n} f_n, \tag{3.8}$$

and a poloidal coefficient s_n^m given by equation (3.3). Therefore, to construct a planar flow, we can define f_n and find the corresponding poloidal and toroidal coefficients from (3.3), (3.7) and (3.8).

Another way to construct a planar flow is by transforming a given flow, $\mathbf{v}$, into a planar flow. We can take the poloidal and toroidal parts of $\mathbf{v}$ and add the corresponding poloidal and toroidal coefficients using equation (3.3), (3.7) and (3.8). We call this procedure *the planarizing process*.

Suppose,

$$\mathbf{v} = (2 - \delta_m^0)\Re\{\mathbf{s}_n^m + \mathbf{t}_n^m\},$$

where $\Re$ indicates the real part. For the given $\mathbf{s}_n^m (m \neq 0)$, we can derive f_n from equation (3.3) and construct $t_{n\pm1}$ from equations (3.7) and (3.8). The combination $\mathbf{s}_n^m + \mathbf{t}_{n-1}^m + \mathbf{t}_{n+1}^m$ is then planar, and $\mathbf{s}_n^m$ has been planarized. However, it is impossible to find f_n for given $\mathbf{s}_n^0$, due to the m factor in the numerator of equation (3.3).

There are two options for planarizing the $\mathbf{t}_n^m$ component. We can either (i) derive f_{n+1} from t_n using equation (3.7), or (ii) derive f_{n-1} from t_n using equation (3.8). In case (i), we generate s_{n+1} and t_{n+2} using equation (3.3) and (3.8) to get the planar combination $\mathbf{t}_n^m + \mathbf{t}_{n+2}^m + \mathbf{s}_{n+1}^m$. In case (ii), we generate s_{n-1} and t_{n-2} using equation (3.3) and (3.7) in order to get the planar combination $\mathbf{t}_n^m + \mathbf{t}_{n-2}^m + \mathbf{s}_{n-1}^m$. For given t_n, the f-solutions of equations (3.7) and (3.8) satisfying the rigid boundary condition (2.33) at $r = 1$ are

$$\begin{aligned} f_{n+1} &= \frac{n+1}{\alpha_{n+1}} r^{-n-2} \int_1^r r^{n+2}\, t_n\, dr \,, \\ f_{n-1} &= -\frac{n}{\alpha_n} r^{n-1} \int_1^r r^{-n+1}\, t_n\, dr \,. \end{aligned} \tag{3.9}$$

In case (i), t_n must also satisfy the consistency condition

$$\int_0^1 r^{n+2}\, t_n\, dr = 0 \,, \tag{3.10}$$

in order for f_{n+1} given by equation (3.9a) to satisfy the differentiability conditions (2.40) and (2.41). Otherwise, $\mathbf{t}_n$ cannot be planarized by method (i). In case (ii), the f_{n-1} of equation (3.9b) satisfies the differentiability condition. However, if $n = |m|$, the flow cannot be planarized by method (ii) since $\alpha_n = 0$.

Due to the above constraints, some flows can only be partly planarized. For example, for the flow of PAS only the poloidal part can be planarized. This example will be discussed later in §3.2.2

3.2 The Preliminary Results

In this section §3.2, we discuss the history of our investigation on planar velocity dynamos. Most of the content of this section is from BIJ (2006). Also, some background theory and low truncation numerical results were reported earlier in my MSc (by coursework) project. However, this discussion is important because the earlier results are the foundation of our current investigation.

3.2.1 Single Harmonic Flows

BIJ considered flows with a single harmonic degree, with stream function

$$f_n^m = r^n (1 - r^2)^p Y_n^m, \tag{3.11}$$

where $1 \leqslant n \leqslant 4$, $-n \leqslant m \leqslant n$ and $p = 1, 2, 3$. The choices of n, m, p values were due to computer limitations and convergence difficulties. The associated planar flow is

$$\mathbf{v} = (2 - \delta_m^0)\Re\{\mathbf{s}_n^m + \mathbf{t}_{n-1}^m + \mathbf{t}_{n+1}^m\}\,, \tag{3.12}$$

where s_n^m, t_{n-1}^m and t_{n+1}^m are derived from f_n using equation (3.3), (3.7) and (3.8). These flows satisfy the differentiability conditions (2.40) and (2.41), the rigid boundary condition (2.33) and, if $p > 1$, the no-slip conditions (2.34). For these flows, we can use DQ- and m-decoupling for the magnetic chain as we discussed in Chapter 2.

BIJ considered 36 models and found that, where convergence was evident, all of their models, except one, supported the planar velocity anti-dynamo theorem. BIJ labeled a model with flow parameters $n = 4, m = 2$ and magnetic field chain DM12 by the acronym Y42DM12, and if $p = 1$ then by p1Y42DM12. Here, we follow their nomenclature for naming single harmonic flows. The BIJ exceptional case is when $n = 2$, $m = 2$, $p = 1$ using DM12 decoupling, i.e. model p1Y22DM12, with stream function

$$f_2^2 = r^2(1 - r^2)Y_2^2. \tag{3.13}$$

The streamlines of this model are depicted in Figure 3.1. The profile of $\lambda_{\max}$ can be seen in Figure 3.2. The profile suggests that p1Y22DM12 can produce a successful dynamo. The critical magnetic Reynolds number (R_{crit}) is around 210. The graph shows that the profile has converged to some extent. However, the numerical results, in Table 3.1, show that the change in λ is around 10% as N is increased and 40% as J is increased at $R = 220$. On the other hand, Figure 3.2 shows that p2Y22DM12 and p3Y22DM12 do not maintain a magnetic field for $R < 220$.

BIJ were unable to obtain higher accuracy due to computer limitations. High accuracy for model p1Y22DM12 can be achieved by increasing $[J, N]$. The method of doing this will be discussed in §3.3.

Besides p1Y22DM12, some indication of growing modes were also found for two other models i.e. p1Y42DM12 and p1Y44DM24; due to poor convergence these results were not published. The stream functions of these models are

$$f_4^2 = r^4(1 - r^2)Y_4^2, \tag{3.14}$$

$$f_4^4 = r^4(1 - r^2)Y_4^4. \tag{3.15}$$

We will reconsider these models at higher $[J, N]$ later in §3.4.

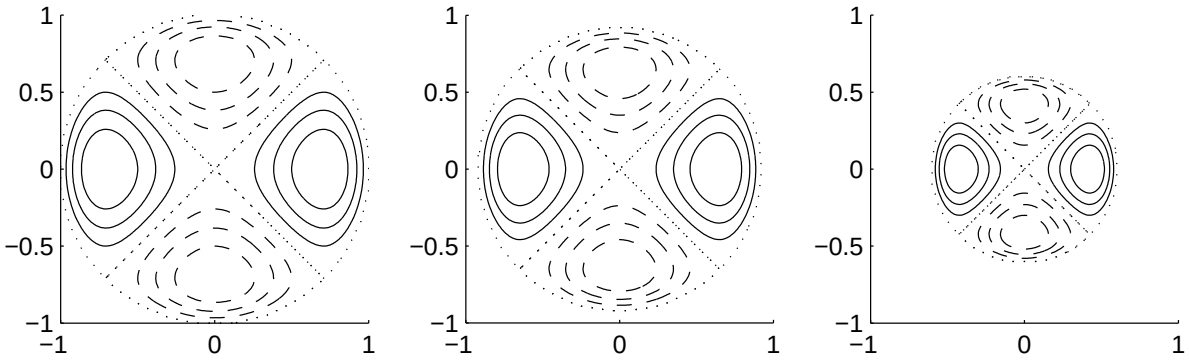

Figure 3.1: The streamlines $f_2^2 = \text{const.}$ for p1Y22DM12 at $z = 0, 0.4, 0.8$. Solid (dashed) lines represent positive (negative) f_2^2. Flow direction is determined by $v_\phi = -\partial f/\partial\varpi$.

N	$J = 400$	$J = 800$
24	1.404215	1.002401
25	1.542941	1.120445
28	0.919501	
29	1.188013	
30	0.979911	

Table 3.1: $\lambda_{\max}$ for model p1Y22DM12 at $R = 220$. The size of the matrix band is around 3 GB.

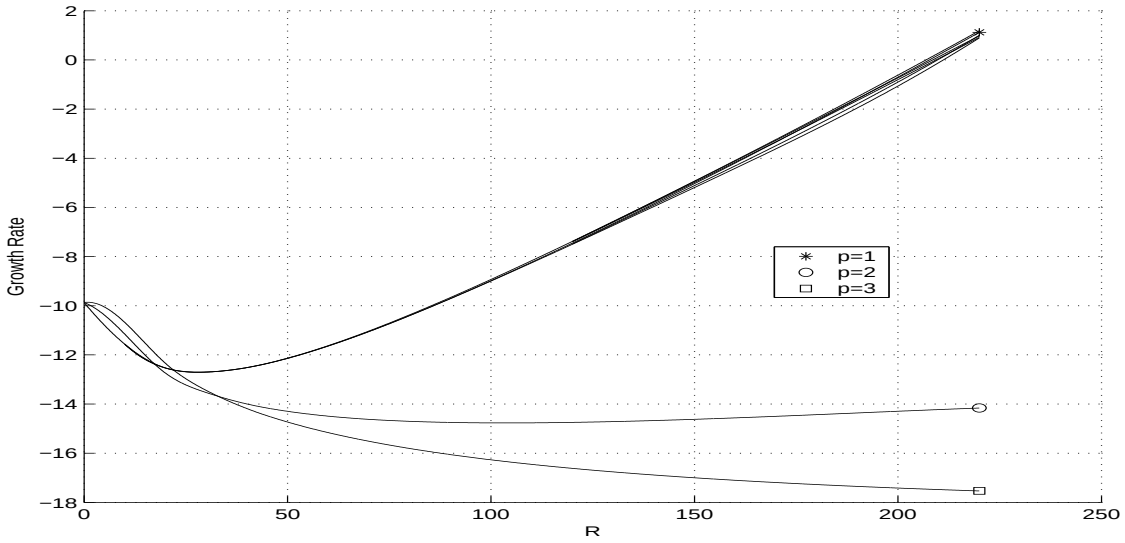

Figure 3.2: $\lambda_{\max}\{R\}$ profiles for model p1Y22DM12, with $p = 2, 3$ using $[J, N] = [200, 20]$, and $p = 1$ using the six truncation levels $[J, N] = [1200, 22], [800, 24], [800, 25], [400, 28], [400, 29], [400, 30]$.

3.2.2 Planarizing Three Historical Flows

In this section, we try to planarize three well-known flows: the Bullard & Gellman flow (1954), the Kumar & Roberts flow (1975), and the Pekeris, Accad & Shkoller flow (1973). Before planarizing them, we outline the properties of these flows. A more comprehensive discussion of the original unplanarized flows can be found in Dudley & James (1989, DJ).

To planarize the above flows, we need to find, for each s and t component of the original flow, appropriate s and t planarizing coefficients. We need to use (3.3), (3.7) and (3.8) and the planarizing procedure given on page 28–29. Our aim is to see whether the planarization process enhances dynamo action.

Bullard & Gellman Flow

This flow was firstly discussed by BG. Later on, DJ re-examined BG's work using higher $[J, N]$ with $J \leqslant 125$ and $N \leqslant 12$, and investigated non-steady solutions. In our formalism, the BG flow is

$$\mathbf{v} = \epsilon \mathbf{t}_1^0 + 2\Re\{\mathbf{s}_2^2\}, \tag{3.16}$$

where

$$t_1^0 = \frac{1}{\sqrt{3}} r(1-r), \tag{3.17}$$

$$s_2^2 = s_2^{-2} = \sqrt{\frac{6}{5}} r^2 (1-r)^2. \tag{3.18}$$

This flow satisfies the rigid boundary condition (2.33) and no-slip conditions (2.34), but not the differentiability conditions (2.40) and (2.41). The $\lambda_{\max}$-profile can be seen in Figure 3.3a. In order to planarize the poloidal part $\mathbf{s}_2^2$, we need to add $\mathbf{t}_3^2$ to the flow. In contrast, the toroidal part $\mathbf{t}_1^0$ is already planar. Thus, the planarized version of BG flow is

$$\mathbf{v} = \epsilon \mathbf{t}_1^0 + 2\Re\{\mathbf{s}_2^2 + \mathbf{t}_3^2\}, \tag{3.19}$$

where

$$f_2^2 = -3\mathrm{i} s_2^2, \tag{3.20}$$

$$t_3^2 = -\frac{1}{3\sqrt{7}} \Big(\frac{\mathrm{d} f_2}{\mathrm{d} r} - \frac{2}{r} f_2 \Big). \tag{3.21}$$

The t_3^2 coefficient is derived using equation (3.8). In this project, we use $\epsilon = 5$ with DM02 magnetic chain decoupling.

No one has yet shown the ability of the original BG flow to maintain a magnetic field. BIJ's results reveal that the magnetic field of the planarized version decays over a certain range of the magnetic Reynolds number. The $\lambda_{\max}$-profiles can be

seen in Figure 3.3a on page 35. The planar decay-rate is better than the original. Moreover, the $\lambda_{\max}$-profile of the planar version is purely real, whereas the original one is complex for $R \gtrsim 30$.

Kumar & Roberts Flow

In our formalism, the Kumar & Roberts (KR) flow is

$$\mathbf{v} = \mathbf{t}_1^0 + \epsilon_1 \mathbf{s}_2^0 + 2\epsilon_2 \Re\{\mathbf{s}_2^2\}, \tag{3.22}$$

where

$$t_1^0 = \frac{r(1-r^2)}{\sqrt{3}}, \tag{3.23}$$

$$s_2^0 = \frac{r^5(1-r^2)^3}{\sqrt{5}}, \tag{3.24}$$

$$s_2^{-2} = \overline{s_2^2} = \frac{\mathrm{i}r^3(1-r^2)^2 e^{-\mathrm{i}k\pi r}}{\sqrt{10}}. \tag{3.25}$$

This flow satisfies the rigid boundary condition (2.33) and no-slip conditions (2.34), but not the differentiability conditions (2.40) and (2.41). We use $\epsilon_1 = 0.03, \epsilon_2 = 0.04, k = 3$ and DM02 decoupling, a set of parameters shown by the earlier researchers to maintain the magnetic field. This flow was established by KR and reconsidered using higher $[J, N]$ by DJ.

It is impossible to fully planarize this flow due to the presence of the meridional circulation s_2^0. BIJ were unable to use equation (3.3) to find the corresponding toroidal coefficients because $m = 0$. As a result, they only planarized $\mathbf{s}_2^2$ and defined the partly planarized version of the KR flow

$$\mathbf{v} = \mathbf{t}_1^0 + \epsilon_1 \mathbf{s}_2^0 + 2\epsilon_2 \Re\{\mathbf{s}_2^2 + \mathbf{t}_3^2\}, \tag{3.26}$$

where

$$f_2^2 = -3\mathrm{i}s_2^2, \tag{3.27}$$

$$t_3^2 = -\frac{1}{3\sqrt{7}}\Big(\frac{\mathrm{d}f_2}{\mathrm{d}r} - \frac{2}{r}f_2\Big). \tag{3.28}$$

As shown in Figure 3.3b, the partly planarized KR model does not produce dynamo action for the given parameters. Although not shown on the graph, the $\lambda_{\max}$-profile remains flat over the interval $|R| \leqslant 25000$. The $\lambda_{\max}$-profile of the partly planarized model is purely real, whereas the original KR model has an oscillatory mode for $-1300 \leqslant R \leqslant -1000$.

Sarson and Gubbins (1996) showed that the KR flow (3.22) is still able to produce dynamo action without the meridional component, i.e. with $\epsilon_1 = 0$, although $R > 20000$ is required. Following this result, BIJ fully planarized the KR flow with $\epsilon_1 = 0$. They discovered that the magnetic field decays over the entire interval $|R| \leqslant 25000$. Thus, in this case planarization has destroyed the dynamo action found by Sarson and Gubbins.

Pekeris, Accad & Shkoller Flow

In their last trial, BIJ attempted to planarize the Pekeris, Accad and Shkoller (PAS) flow. BIJ chose this flow because $\lambda_{\max}$ easily converges at a relatively low critical magnetic Reynolds number, $R_{\text{crit}} \approx 0.37$. They also believed that it might be possible to fully-planarize PAS flow due to the absence of meridional circulations.

The PAS flow in our formalism is

$$\mathbf{v} = 2\Re\{\mathbf{s}_2^2 + \mathbf{t}_2^2\}, \tag{3.29}$$

where

$$s_2^2 = K\Lambda j_2(\Lambda r), \tag{3.30}$$
$$t_2^2 = \Lambda s_2^2(r). \tag{3.31}$$

Here, $K = \sqrt{6/5}$, and Λ is a positive root of the spherical Bessel function

$$j_2(r) = \left(\frac{3}{r^3} - \frac{1}{r}\right)\sin r - \frac{3}{r^2}\cos r. \tag{3.32}$$

This flow satisfies the rigid boundary condition (2.33) and the differentiability conditions (2.40) and (2.41), but not the non-slip conditions (2.34). This flow was proposed by PAS and reconsidered by DJ using higher $[J, N]$.

To planarize $\mathbf{s}_2^2$, BIJ used equation (3.3) to define

$$f_2^2 = -3\mathrm{i}K\Lambda j_2(\Lambda r),$$

and constructed t_3^2 using equation (3.8). A problem emerged when they wanted to planarize $\mathbf{t}_2^2$. BIJ constructed f_3^2 using equation (3.7). However, the t_2^2 term does not satisfy the consistency condition (3.10). As a consequence, f_3^2 cannot satisfy both the differentiability conditions (2.40) and (2.41), and the rigid boundary condition (2.33). Thus, similar to the KR flow, they only planarized $\mathbf{s}_2^2$ and defined the partly planarized version of PAS flow:

$$\mathbf{v} = 2\Re\{\mathbf{s}_2^2 + \mathbf{t}_2^2 + \mathbf{t}_3^2\}, \tag{3.33}$$

Here, they used $\Lambda = 12.3229$ and magnetic chain M02. As presented in Figure 3.3c on the next page, the growth rate of the partly planarized model is significantly better than the original PAS model. Moreover, R_{crit} is reduced from 0.37 to about 0.26.

Of the three trials, BIJ succeeded in fully-planarizing the BG flow but failed to planarize the others. We conclude that it is not always easy to planarize an existing flow. It may be necessary to modify the original flow slightly in order to construct a fully-planarized version.

(a)

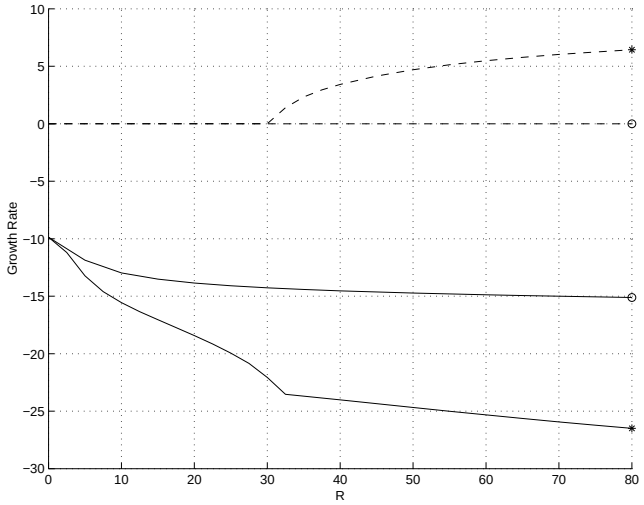

(b)

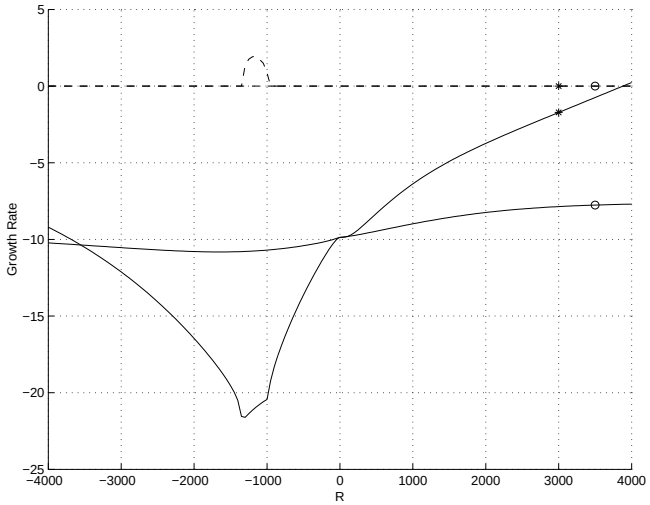

(c)

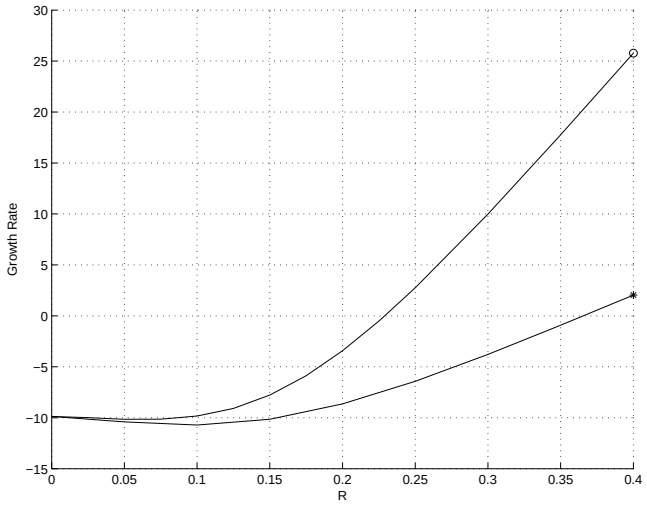

Figure 3.3: $\lambda_{\max}\{R\}$ profiles for original ($\bullet$) and planarized ($\circ$) flows of (a) BG with $[J, N] = [100, 12]$, (b) KR with $[J, N] = [150, 12]$, and (c) PAS with $[J, N] = [100, 15]$, $\Re\lambda_{\max}\{R\}$(solid line),$\Im\lambda_{\max}\{R\}$ (dashed line).

3.3 The Sub-Band Method

Although Figure 3.2 shows a growing mode, the convergence level, i.e. the convergence of the first two leading digits, of the eigenvalues in Table 3.1 is still around 10%. This is not quite a satisfactory level of convergence, since, in most work, the level of convergence is usually around 1%. In order to get a better convergence level, we need to increase $[J, N]$. However, the problem is the size of the matrix band has reached the maximum RAM capacity of our computers.

To overcome this problem, we modified our dynamo routine so that it stores the matrix on a disk and processes sub-bands of the matrix one at a time. To fit the available computer memory, the size of each sub-band needs to be controlled. First, we create a sub-band of the matrix and store it on the disk. We repeat this procedure until the whole matrix is stored. After that, we retrieve a sub-band of the matrix, process it and store it back on the disk. This process is repeated until the whole matrix is processed. We call this procedure the sub-band method. Unfortunately, each sub-band requires information from the previous sub-band. So, we cannot apply parallel computing techniques to the routine.

An example of the banded matrix can be seen in Figure 3.4. We only need to store the matrix band. If the band structure is destroyed, the size of the matrix will increase dramatically which means more memory will be needed. To avoid that situation, we needed to write our own routine rather than use any available software package.

Using the sub-band method, we can attain higher $[J, N]$ for model p1Y22DM12 and thus expect to get better convergence. However, due to the retrieving and storing process, the modified routine is slower than the original. A sufficiently large and fast disk space is needed to avoid the modified routine being impracticable.

Before applying the modified routine to higher $[J, N]$, we ran it using small $[J, N]$ and compared the results against those calculated using the original routine. We achieved exact agreement which indicates that the modification has been appropriately conducted.

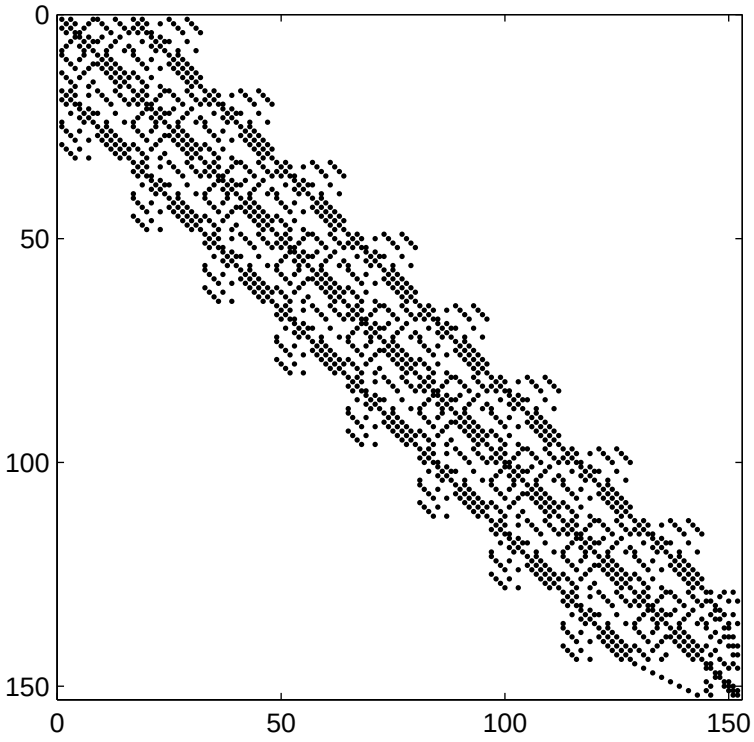

Figure 3.4: Matrix of model p1Y22DM12 using a low $[J, N] = [10, 3]$ which has sparse and banded structure.

3.4 Higher Truncation Level Results

In this section, we present the results for model p1Y22DM12 using higher $[J, N]$. To achieve these results, we used a 64 bit machine with 8 GB of RAM. In addition to model p1Y22DM12 results, we also present models p1Y42DM12 and p1Y44DM24 results using higher $[J, N]$. Furthermore, we find a modified p1Y22DM12 model which has a better convergence level than the original p1Y22DM12 model.

In presenting our results, we use several different convergence tests. Each of the models uses all or part of the following tests. The classical ones are the growth rate graph and the $\lambda_{\max}$ table using several $[J, N]$. We also plot $\lambda_{\max}$ against N, i.e. $\lambda(N)$, with various J. The last indicator is the plot of $\lambda_{\max}$ against h^2, i.e. $\lambda(h^2)$, with various N. We do not use the graphs of $S_n^m(r)$ and $T_n^m(r)$ because it is inconvenient to use these for high $[J, N]$. We will discuss this issue in Chapter 6.

3.4.1 Model p1Y22DM12

For higher $[J, N]$, the sub-band routine requires a long computer run time for each combination of N, J, R. Therefore, we decided to observe the change in λ at a fixed slightly supercritical Reynolds number in order to reduce the number of runs. From Figure 3.2, R_{crit} for model p1Y22DM12 appears to be about 210. Thus, we choose $R = 220$ for our numerical investigation.

Our aim is to get around a 1% convergence level for $\lambda_{\max}$. First, we run the model at a fixed J, and vary N. Based on preliminary results, we choose $[400, 25]$ as the minimum $[J, N]$ level. Fixing $J = 400$, we get a 0.1% change in $\lambda_{\max}$ with $N = 55, 56$. The matrix band-size is around 38 GB. On the other hand, if we fix N and vary J, we obtain a best result of about 5% at $N = 35$ and $J = 1600, 2400$. The change in $\lambda_{\max}$ is presented in Table 3.2. In addition, several computer run times for model p1Y22DM12 are presented in Table 3.3.

In Figure 3.5, we plot $\lambda(N)$ with various values of J. It is observable that convergence is occurring as we increase N and J. The graph suggests that it is possible to obtain a satisfactory convergence level. However, higher $[J, N]$ are needed to achieve this aim. In figure 3.6, we plot $\lambda(h^2)$ with $N = 35 - 45$.

At the moment, the largest achievable matrix band-size is around 38 GB which is equivalent to $[J, N]$ such as $[J, N] = [400, 56], [800, 45], [1600, 35]$. Reaching the maximum disk space of our machine, we have to stop increasing the size of the matrix. From Figure 3.5, we predict that we need to run the model with $J = 1600, 2400$ and $N = 55, 56$ to get a 1% level of convergence. However, the matrix band-size then is around 230 GB and would require more that a week to run on our machine for each N, J, R combination.

Because of time constraints, we have to put off investigating this model in order to investigate other planar flow models. We leave this model for future work when a faster computer with a greater memory is available for us to use.

N	$J = 400$	$J = 800$	$J = 1600$	$J = 2400$
31	0.768363	0.362947	0.261183	0.242320
32	0.877181	0.471211	0.369300	0.350410
33	1.045474	0.635773	0.532922	0.513857
34	0.988497	0.579102	0.476332	0.457282
35	0.861048	0.455024	0.353103	0.334210
55	0.929184			
56	0.930387			

Table 3.2: $\lambda_{\max}$ for model p1Y22DM12. The convergence level is around 5% with respect to J and 1% with respect to N.

J	N	matrix band(GB)	sub-band(GB)	run-time(hr)
400	56	38	7	107
800	45	33	7	91
1600	35	26	7	70
2400	35	39	7	91

Table 3.3: The computer run time of model p1Y22DM12 using higher $[J, N]$. A 64 bit machine with 8 GB of RAM is used.

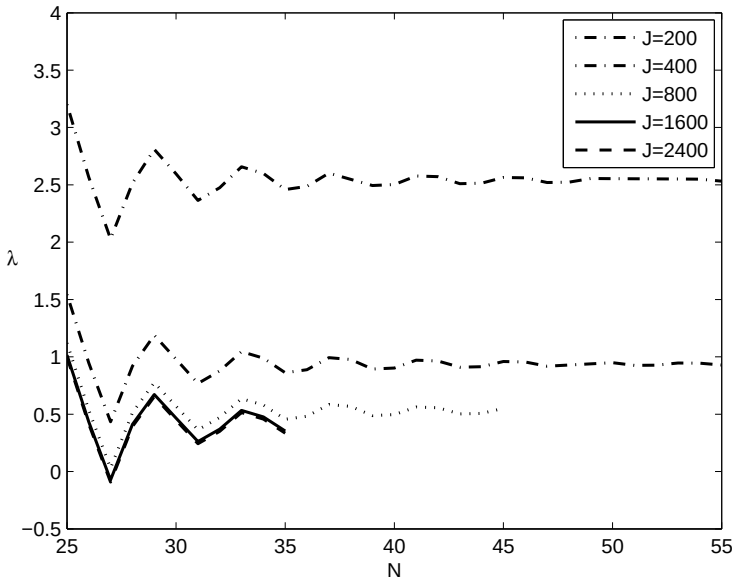

Figure 3.5: $\lambda_{\max}(N)$ for model p1Y22DM12 with various J at $R = 220$. The convergence level is less than 1% for J=200,400 with N=54,55.

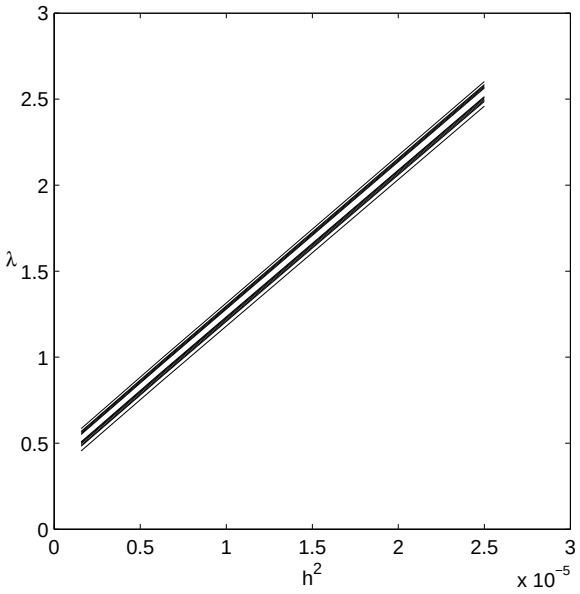

Figure 3.6: $\lambda_{\max}(h^2)$ for model p1Y22DM12 with $J = 200, 400, 800$ and $N = 35-45$ at $R = 220$. These lines are parallel and their gaps become smaller as we increase N.

3.4.2 Models p1Y42DM12 and p1Y44DM24

In the preliminary results of §3.2, model p1Y42DM12 and p1Y44DM24 indicate the existence of a dynamo process. However, the indication is weaker than that of model p1Y22DM12. Streamlines of these flows can be seen in Figures 3.7–3.8. These contours indicate steeper gradients than for the p1Y22DM12 flow in Figure (3.1). Furthermore, p1Y44DM24 has 8 cells compared to 4 cells in p1Y22DM12 flow. We expect therefore that it is even more difficult to obtain convergent results for these flows compared to the p1Y22DM12 flow.

As a start, we investigate these flows using $[J, N]$, which are equivalent to 3 GB matrix size. Growth rates for these models can be seen in Figure 3.9–3.10. As expected, the convergence is much worse than for model p1Y22DM12. Consequently, the $[J, N]$ required for these models is impracticable. However, Figures 3.9–3.10 show that these models might have growing modes. Thus, we may investigate these flows in the future.

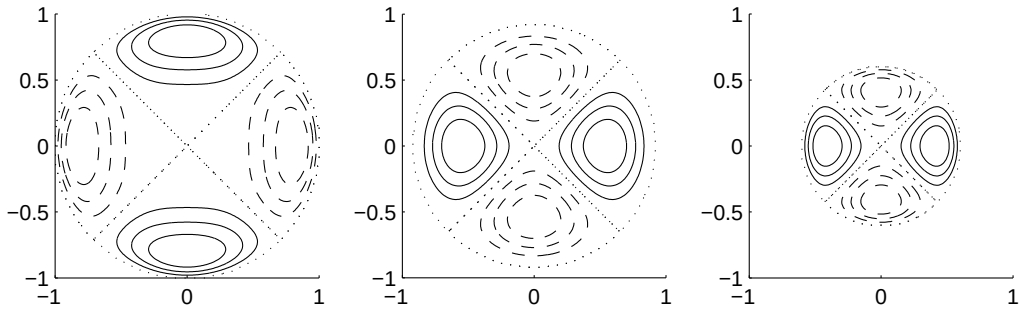

Figure 3.7: The streamlines $f_4^2 = \text{const.}$ for p1Y42DM12 at $z = 0, 0.4, 0.8$. Solid (dashed) lines represent positive (negative) f_4^2. Flow direction is determined by $v_\phi = -\partial f / \partial \varpi$.

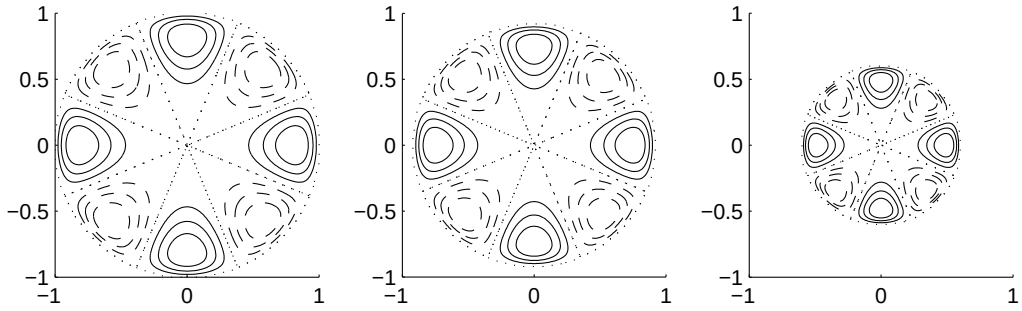

Figure 3.8: The streamline $f_4^4 = \text{const.}$ for p1Y44DM24 at $z = 0, 0.4, 0.8$. Solid (dashed) lines represent positive (negative) f_4^4. Flow direction is determined by $v_\phi = -\partial f / \partial \varpi$.

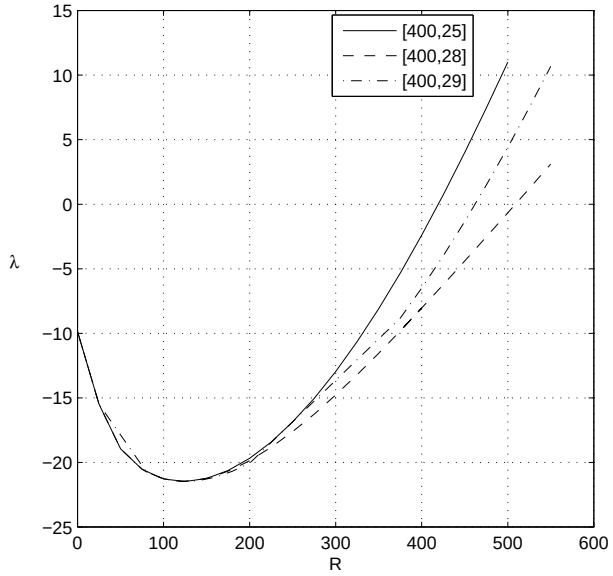

Figure 3.9: $\lambda_{\max}(R)$ for model p1Y42DM12 using the three truncation levels $[J, N] = [400, 25], [400, 28], [400, 29]$. The convergence level is inadequate but suggestive of a growing mode.

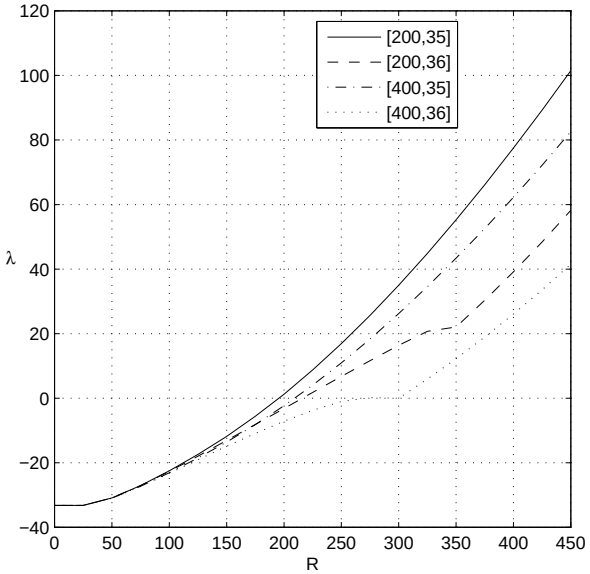

Figure 3.10: $\lambda_{\max}(R)$ for model p1Y44DM24 using the four truncation levels $[J, N] = [200, 34], [200, 35], [400, 34], [400, 35]$. The convergence level is inadequate but suggestive of a growing mode.

3.4.3 Model p1q10Y22DM12

In the original proof of the PVT, B_z decays as $t \to \infty$. However, for a finite volume, the second term of (2.44) does not vanish. BIJ argued, using maximum principles, that maxima of B_z must occur at the boundary. One might expect that there is a mechanism near the boundary that generates B_z. Once B_z is generated, the other two components of $\mathbf{B}$ are also created.

Following the above argument, we modify the p1Y22DM12 radial function, f_2^2, to have steeper gradients near $r = 1$ and hope to get better convergence. The modified stream functions are:

$$f_2^2 = r^2(1 - r^q)^p Y_2^2 \tag{3.34}$$

where $p = 1, q = 4, 6, 8, ...$
We label these models p1q4Y22DM12, p1q6Y22DM12, p1q8Y22DM12,.... Preliminary results are shown in Table 3.4. The table shows results for $\lambda_{\max}$ at slightly supercritical R. These results suggest that $q = 10$ is optimum with respect to convergence, and lowest R_{crit} without normalization.

Plots of the radial parts f_2^2 for the p1Y22DM12 and p1q10Y22DM12 flows can be seen in Figure 3.11. It can be seen that f_2^2 for p1q10Y22DM12 flow has a steeper gradient near $r = 1$. Meanwhile, Figure 3.12 shows the streamlines of p1q10Y22DM12 at certain levels of z.

The numerical results for model p1q10Y22DM12 can be seen in Table 3.5. The convergence level in the N direction, i.e. where we fix J and vary N, is much better than the p1Y22DM12 model. Using the same $[J, N]$, $N = 31 - 35$ and $J = 400$, the convergence level for $\lambda_{\max}$ of the p1Y22DM12 model is around 10%. Meanwhile, the p1q10Y22DM12 model has around 1–3% convergence level.

To be able to compare the R_{crit} of models p1Y22DM12 and p1q10Y22DM12, we normalized the R_{crit} using: root-mean-square of $\mathbf{v}$, rms($\mathbf{v}$), and maximum of $|\mathbf{v}|$, $\max|\mathbf{v}|$. The normalized R_{crit} can be seen in Table 3.6. If we use rms($\mathbf{v}$), then model p1q10Y22DM12 has lower R_{crit}. However, if we use $\max|\mathbf{v}|$, then model p1Y22DM12 has lower R_{crit}. Thus, we can make no conclusion on which model has lower R_{crit}.

Figures 3.13 and 3.14 are similar to those of the p1Y22DM12 model in Figures 3.5 and 3.6 and indicate that convergence is occurring, and at a faster rate than for model p1Y22DM12.

N	$J = 400$	$J = 800$
R=220 q=2		
28	0.919	0.513
29	1.188	0.775
30	0.979	0.569
R=120 q=4		
28	1.658	1.262
29	1.877	1.476
30	1.763	1.363
R=90 q=6		
28	2.324	1.890
29	2.514	2.075
30	2.434	1.995
R=75 q=8		
28	2.556	2.082
29	2.719	2.242
30	2.661	2.183
R=65 q=10		
28	2.178	1.688
29	2.311	1.817
30	2.270	1.776
R=60 q=12		
28	2.401	1.855
29	2.527	1.977
30	2.489	1.938
R=50 q=20		
28	2.263	1.522
29	2.361	1.616
30	2.326	1.580
R=47 q=50		
28	1.913	0.525
29	2.029	0.643
30	1.919	0.526

Table 3.4: $\lambda_{\max}$ for model p1qY22DM12 with various q. With $q = 10$, the flow has lower R_{crit} compared to model p1Y22DM12 (i.e. model p1q2Y22DM12) and has reasonable convergence with respect to N and J.

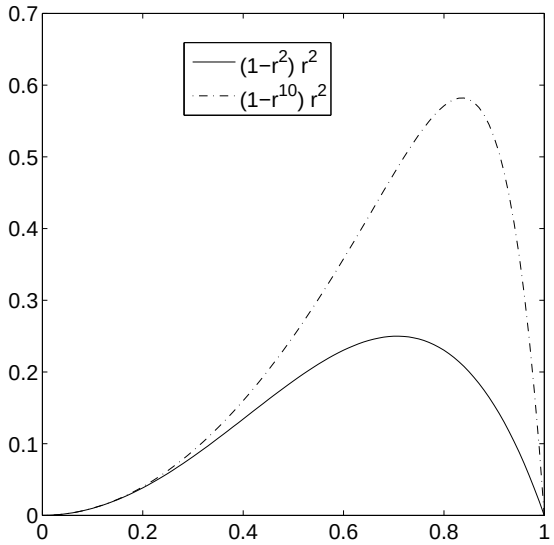

Figure 3.11: The radial functions for the p1Y22DM12 and p1q10Y22DM12 flows.

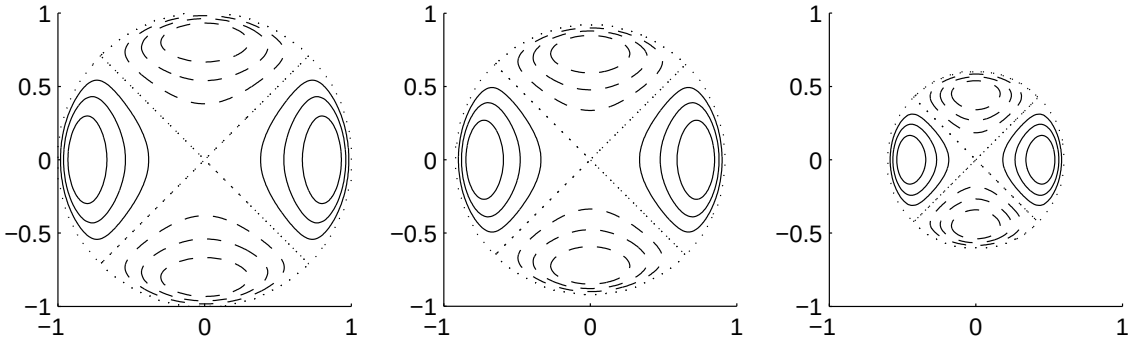

Figure 3.12: The streamline $f_2^2 = \text{const.}$ for p1q10Y22DM12 at $z = 0, 0.4, 0.8$. Solid (dashed) lines represent positive (negative) f_2^2. Flow direction is determined by $v_\phi = -\partial f / \partial \varpi$.

N	$J = 400$	$J = 800$	$J = 1600$	$J = 2400$
31	2.169138613	1.678021203	1.554858646	1.532034014
32	2.182484715	1.691741681	1.568671992	1.545864522
33	2.259949847	1.766388264	1.642612095	1.619673714
34	2.256005780	1.762247456	1.638422579	1.615475209
35	2.192478621	1.701350714	1.578185492	1.555360372

Table 3.5: $\lambda_{\max}$ of p1q10Y22DM12 model at $R = 65$. The maximum size of the band matrix is around 38 GB. The convergence level is around 1% with respect to J and 4% with respect to N.

Model	R_{crit}	Normalized R_{crit}	
		rms($\mathbf{v}$)	max $\lvert\mathbf{v}\rvert$
p1Y22DM12	210	317.49	1150.17
p1q10Y22DM12	63	285.74	1725.32

Table 3.6: R_{crit} comparison for models p1Y22DM12 and p1q10Y22DM12.

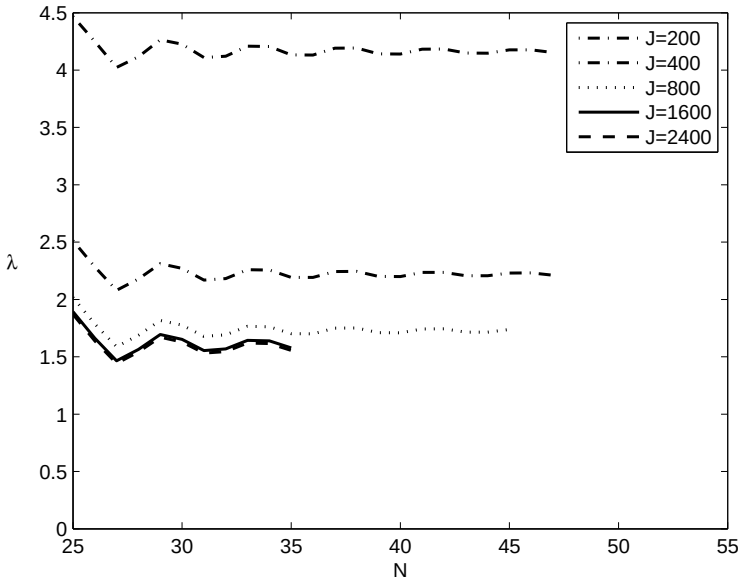

Figure 3.13: $\lambda_{\max}(N)$ of p1q10Y22DM12 model with various J at $R = 65$. The convergence level is less than 1% for J=200,400 with N=45,46.

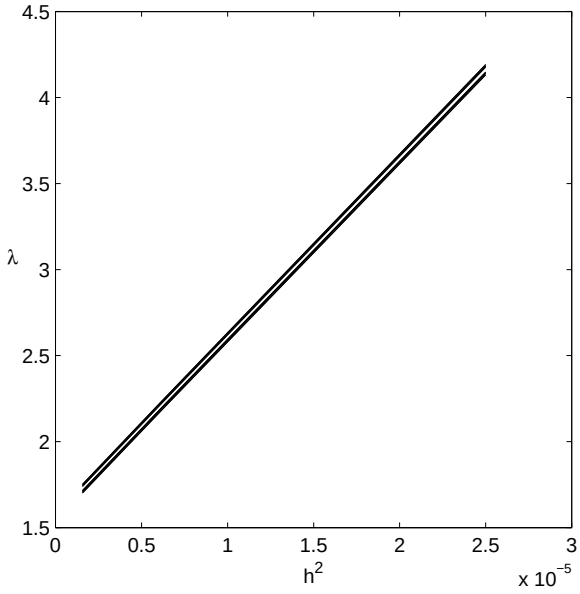

Figure 3.14: $\lambda_{\max}\{h^2\}$ of p1q10Y22DM12 model with $N = 35-45$ at $R = 65$. These lines are parallel and their gaps are smaller than for p1Y22DM12 in Figure 3.6.

3.5 Chapter Summary

BIJ began their numerical investigation using single harmonic (f_n^m) planar flows. They found that most of the models supported the planar velocity theorem. However, one model, p1Y22DM12, indicated existence of a planar velocity dynamo. In addition, two other models, p1Y42DM12 and p1Y44DM14, revealed a weaker indication of the existence of planar velocity dynamos.

BIJ also tried to planarize three well-known models based on: the BG, the PAS, and the KR flows. BIJ were able to fully planarize the BG flow, and partly planarize the other two flows. BIJ found that the planarized version of the BG flow does not produce a dynamo over the interval $0 \leq R \leq 80$. However, the planarization process improved the $\lambda_{\max}$ profile. Moreover, the partly planarized PAS flow has a higher $\lambda_{\max}$ profile than the original PAS, and significantly lower R_{crit}. On the other hand, the partly planarized KR flow fails to maintain a magnetic field.

To get a better convergence level for model p1Y22DM12, we modified our program using a sub-band method so that it can run higher $[J, N]$. We calculated model p1Y22DM12 using higher $[J, N]$, up to matrix band size 38 GB, and achieved better convergence. Our plots in Figures 3.5–3.6 show that $\lambda_{\max}$ converges, but indicate that $[J, N] \geq [400, 56]$, i.e. a band size $\geq$ 38 GB, is needed to get accuracy $\lesssim 1\%$ in $\lambda_{\max}$.

The convergence problem for models p1Y42DM12 and p1Y44DM24 are much worse

than for model p1Y22DM12. So, we have to defer the investigation of these models to some future time.

In §3.4.3, we reported that certain modified p1Y22DM12 flows also indicated they could support planar velocity dynamos. By modifying the radial function of model p1Y22DM12 to have a greater gradient near the boundary, better convergence and lower R_{crit} were obtained. Model p1q10Y22DM12 is found to be optimum in this regard as shown by Table 3.4.

Chapter 4

The Effect of Spherical Shells on Planar Velocity Dynamos

4.1 The Effect of Spherical Shells on Kinematic Dynamos

In the previous Chapter, we assumed that the fluid occupies a sphere. However, for modelling planetary magnetism, it is not accurate to have such an assumption. From seismological data, researchers believe that the Earth has a solid inner core and liquid outer core. The radius of the Earth's inner core is around 1,220 km. The radius of the outer core is around 3,480 km. Some dynamo models include an inner core. This means the fluid occupies a spherical shell instead of a sphere. In this section, we review some earlier work on kinematic dynamos in spherical shells.

The first dynamo work using a spherical shell may have been that by PAS. PAS allowed for an insulating inner core represented by boundary conditions (4.4), (4.5) later herein (equation (92) in PAS). PAS reported that the inner core has no significant effect on their dynamo. Unfortunately, they did not include any numerical results.

Sarson and Gubbins (1996,SG) investigated the effect of inner cores on one of the KR flows. In their work, SG considered both insulating and conducting inner cores. They reported no significant effect for either type of inner core on their particular model.

Another investigation was conducted by Holme (1997). He also included both type of cores. Holme used three different flows. The first flow was the KR flow defined by equation (3.22). He also investigated an altered KR flow, his KR$'$ flow, where s_2^0

is altered to become (in our formalism)

$$s_2^0 = \frac{r^2(1-r^2)^2}{\sqrt{5}}.$$

The last flow that he investigated was one of the DJ flows: in our formalism,

$$\mathbf{v} = \mathbf{t}_1^0 + \epsilon\, \mathbf{s}_2^0, \tag{4.1}$$

where

$$t_1^0 = \sin(\pi r)/\sqrt{3},$$
$$s_2^0 = r\sin(\pi r)/\sqrt{5},$$

with magnetic chain: $S_1^1, T_1^1, S_2^1, T_2^1, S_3^1, T_3^1, ...$

Holme extrapolated his results to get R_{crit} with $h \to 0$ and had similar results to SG. Holme's results can be seen in Table 4.1. We used his results as a benchmark for our computer routine and obtained satisfactory agreement. (Small differences were present presumably due to the different methods used.)

r_c	Conducting	Insulating
(a)		
0.1	4461.78	4461.08
0.2	5149.98	5135.86
0.3	6010.60	5936.21
0.4	7083.33	6861.10
(b)		
0.1	129.123(20.401)	129.099(20.399)
0.2	272.640(29.597)	271.843(29.508)
(c)		
0.1	3962.12	3960.85
0.2	4688.29	4671.54
0.25	163.636	165.572
(d)		
0.1	144.661	144.657
0.2	157.906	158.413

Table 4.1: R_{crit} and non-zero $\Im\{\lambda\}$ (shown in brackets) extrapolated to $h \to 0$ for (a) KR flow, $N = 16, \epsilon_1 = 0.03, \epsilon_2 = 0.04$, (b) DJ flow, $N = 32, \epsilon = 0.13$, (c) KR$'$ flow, $N = 16, \epsilon_1 = 0.005, \epsilon_2 = 0.04$, (d) KR$'$ flow, $N = 16, \epsilon_1 = 0.2, \epsilon_2 = 0.6$.

In the original proof of the PVT, B_z decays. However, if the fluid occupies a finite volume, the proof fails. Moreover, in BIJ, it was shown that the contours of B_z were concentrated near the boundary, $r = 1$. Therefore, in this chapter, we included an inner core to both models p1Y22DM12 and p1q10Y22DM12. We hope that more

B_z will be generated because of the presence of an inner boundary and that the convergence problem will be reduced.

To achieve our aim, there were several steps needed. First, we derived the boundary conditions for the inner core and tested numerical codes utilizing these boundary conditions. Then, we mapped the p1Y22DM12 and p1q10Y22DM12 flows into spherical shells and investigated them numerically.

4.2 Boundary Conditions

For full sphere models, we have the boundary condition (2.32) at $r = 1$ (outer core boundary, OCB), so that $\mathbf{B}$ will be continuous and match with the external field. As mentioned earlier, the exterior of the sphere is an insulator.

Meanwhile, for spherical shells, we have two boundaries. The outer boundary is the same as the full sphere outer boundary. At the inner boundary (ICB), where $r = r_c$ say, there are two types of inner environment to consider: insulating and conducting inner cores.

4.2.1 Insulating Inner Core

From potential theory, the finite solutions of the Laplace equation, $\nabla^2\Phi = 0$ inside and outside a sphere of radius $r = a$ are

$$\Phi = \sum_{n,m} \Phi_n^m \left(\frac{r}{a}\right)^n Y_n^m(\theta,\phi), \qquad r \le a, \tag{4.2}$$

$$\Phi = \sum_{n,m} \Phi_n^m \left(\frac{a}{r}\right)^{n+1} Y_n^m(\theta,\phi), \qquad r \ge a. \tag{4.3}$$

We will use the above results in deriving the boundary conditions.

Using the notation introduced in §3.1

$$\begin{aligned} \nabla\times\hat{\mathbf{B}} &= \nabla\times\mathbf{T}\{\hat{T}\} + \nabla\times\mathbf{S}\{\hat{S}\}, \\ &= \mathbf{S}\{\hat{T}\} + \mathbf{T}\{-\nabla^2\hat{S}\}. \end{aligned}$$

The current free condition (2.8) implies $\hat{T} = 0$ and $\nabla^2\hat{S} = 0$ in $\hat{V}$. From equation (4.3) and the continuity of $\mathbf{B}$ across the boundary, we derive the boundary condition for the OB:

$$\frac{\partial S_n}{\partial r} + (n+1)S_n = T_n = 0\ , \quad \text{at } r = 1\ . \tag{4.4}$$

Applying a similar argument for the insulating inner core, we can use equation (4.2) to derive the boundary condition,

$$\frac{\partial S_n}{\partial r} - \frac{n}{r_c}S_n = T_n = 0\ , \quad \text{at } r = r_c\ . \tag{4.5}$$

4.2.2 Conducting Inner Core

For a conducting inner core, we consider two methods.

Method 1
Here, we take $\mathbf{v} = \mathbf{0}$ for $r \leq r_c$. This is a simpler approach since we do not have to apply a boundary condition on $\mathbf{B}$ at the ICB. We assume the conductivity of the inner core is equal to that of the fluid in the spherical shell. However, the memory usage is as much as for the full sphere problem. If the flow satisfies the conditions

$$s_n = s_n' = s_n'' = 0, \tag{4.6}$$
$$t_n = t_n' = 0, \tag{4.7}$$

at $r = r_c$ then by (2.37) the $\mathcal{O}(h^2)$ error of the finite difference approximations (2.35) and (2.36) on page 20 will be preserved. These conditions (4.6), (4.7) are not satisfied by models p1Y22DM12 and p1q10Y22DM12, but we do not use method 1 for these models.

Method 2
Here, we represent the ICB by boundary conditions on $\mathbf{B}$ at $r = r_c$. This method is valid when we have a stationary field,

$$\nabla^2 \mathbf{B} = 0\ , \quad \text{for } r < r_c, \tag{4.8}$$

and no-slip conditions at the ICB, the need for which will be explained below. Using this method, we can get more accurate results for the same $[J, N]$ since all of the grid points can be put inside the shell.

To understand the need for the no-slip conditions, let us apply Faraday's law,

$$\oint \mathbf{E} \cdot \mathrm{d}\hat{\mathbf{t}} = -\frac{\partial}{\partial t} \int_A \mathbf{B} \cdot \mathrm{d}\mathbf{S} \tag{4.9}$$

to the small rectangle A shown in Figure 4.1, where $\hat{\mathbf{t}}$ is the tangential unit vector. If we let $\delta \to 0$ then the RHS of equation (4.9) tends to 0. This implies,

$$\mathbf{E}_- \cdot \hat{\mathbf{t}} = \mathbf{E}_+ \cdot \hat{\mathbf{t}}, \tag{4.10}$$

where $\mathbf{E}_-$ and $\mathbf{E}_+$ are the electric field just below and just above the ICB. So $\mathbf{E} \cdot \mathbf{t}$ is continuous. If $\mathbf{v}$ satisfies the no-slip condition at the ICB then from the pre-Maxwell equation (2.1) and Ohm's law (2.5), $\nabla \times \mathbf{B} = \sigma\mu\mathbf{E}$, or

$$\mathbf{S}\{T\} + \mathbf{T}\{-\nabla^2 S\} = \sigma\mu\mathbf{E}. \tag{4.11}$$

We introduce the transverse divergence,

$$\nabla_{\mathrm{T}} \cdot \mathbf{A} = \frac{1}{r \sin\theta} \frac{\partial}{\partial\theta} \sin\theta A_\theta + \frac{1}{r \sin\theta} \frac{\partial}{\partial\phi} A_\phi,$$

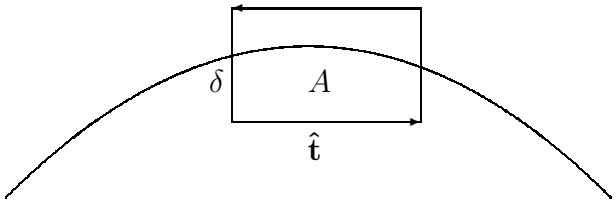

Figure 4.1: A small surface, A, that cuts the inner boundary.

where $\mathbf{A}$ is an arbitrary field. The transverse divergence has the following properties:

$$\nabla_{\mathrm{T}} \cdot \mathbf{S} = -L^2(rS_n)'Y_n, \tag{4.12}$$

$$\nabla_{\mathrm{T}} \cdot \mathbf{T} = 0, \tag{4.13}$$

$$[\nabla_{\mathrm{T}} \cdot \mathbf{E}] = 0 \quad \text{if } [\mathbf{t} \cdot \mathbf{E}] = 0. \tag{4.14}$$

Therefore, applying $\nabla_{\mathrm{T}}\cdot$ to (4.11), we obtain

$$[-L^2(rT_n)'Y_n] = 0. \tag{4.15}$$

which implies $[\mathrm{d}T_n/\mathrm{d}r] = 0$ since $[T_n] = 0$. The solutions of (4.8) are of the form

$$\mathbf{B} = \nabla \times \nabla \times (S\mathbf{r}) + \nabla \times (T\mathbf{r}),$$

where

$$S = \sum_{n,m} \left(\frac{r}{r_c}\right)^n Y_n^m S_n^m(r_c),$$

$$T = \sum_{n,m} \left(\frac{r}{r_c}\right)^n Y_n^m T_n^m(r_c).$$

Matching the magnetic field in $r_c < r < 1$ to this solution at $r = r_c$ gives the following boundary conditions at $r = r_c$:

$$\begin{aligned} \frac{\partial S_n}{\partial r} - \frac{n}{r_c} S_n = 0, \\ \\ \frac{\partial T_n}{\partial r} - \frac{n}{r_c} T_n = 0. \end{aligned} \tag{4.16}$$

The derivation of boundary conditions for a non steady field is harder and is beyond the range of our discussion.

4.3 Validation of Methods 1 and 2

From numerical comparisons, we found that methods 1 and 2 for treating the conducting core give good agreement when both methods are applicable, for example in model KR′ as shown in Table 4.2(b). However, we also found that both methods give reasonable agreement even when method 2 is not applicable, for example in model DJ. Table 4.2(a) compares methods 1 and 2 applied to model DJ (4.1) near $R_{\rm crit} \approx 129.123$. Strictly method 2 is not applicable since $\Im\{\lambda_{\max}\} \neq 0$, but Table 4.2($a$) shows good agreement between methods 1 and 2. Furthermore, the results satisfactorily agree with those of Holme.

(a)	DJ	Method 1	Method 2
	$R = 129.123$ $r_c = 0.1$	$\lambda = (0.0003067, 20.4008)$	$\lambda = (0.0004573, 20.4007)$
(b)	KR′	Method 1	Method 2
	$R = 163.636$ $r_c = 0.25$	$\lambda = (0.003951, 0)$	$\lambda = (0.001417, 0)$

Table 4.2: Comparison of methods 1 and 2 for (a) DJ flow model 4.1 with $[J, N] = [3200, 32]$. (b) KR′ model with $[J, N] = [300, 16]$.

4.4 Models p1Y22DM12 and p1q10Y22DM12 in a Spherical Shell

Having validated our code, we were ready to include inner cores in models p1Y22DM12 and p1q10Y22DM12. However, we needed to transform the corresponding full sphere flows of these models into a spherical shell. Like Holme (1997), we used the linear transformation

$$r^* = \frac{r - r_c}{1 - r_c} \tag{4.17}$$

to rescale our radial functions.

For any flow, in general, the poloidal and toroidal scalars appropriate for the shell are simply[1]

$$\begin{aligned} t^{sh}(r) &= t(r^*), \\ s^{sh}(r) &= s(r^*). \end{aligned} \tag{4.18}$$

[1]To compare with Holme's results, it was necessary to use the BG form. If we used our formalism, then (4.6) would not be satisfied and the $\mathcal{O}(h^2)$ error of the finite difference approximations would not be preserved.

However, for planar flows, such transformations do not produce planar flows in a shell. Indeed, using (3.3), (3.7) and (3.8) inside the shell we would have,

$$\begin{aligned} s_n^{sh} &= \frac{\mathrm{i}m}{n(n+1)} f_n^{sh}, \\ t_{n-1}^{sh} &= \frac{\alpha_n}{n}\Big(\frac{1}{1-r_c}\frac{\mathrm{d}}{\mathrm{d}r^*} + \frac{n+1}{r^*}\Big) f_n^{sh}, \\ t_{n+1}^{sh} &= -\frac{\alpha_{n+1}}{n+1}\Big(\frac{1}{1-r_c}\frac{\mathrm{d}}{\mathrm{d}r^*} - \frac{n}{r^*}\Big) f_n^{sh}, \end{aligned} \tag{4.19}$$

where $f_n^{sh} = f_n(r^*)$. The resulting $\mathbf{v}$, given by (3.12), satisfies rigid boundary conditions for a shell

$$v_r = 0, \text{ at } r = r_c, 1, \tag{4.20}$$

but is not planar. On the other hand, if we transform f_n in (3.11) and apply (3.3), (3.7) and (3.8), we obtain

$$\begin{aligned} s_n^{sh} &= \frac{\mathrm{i}m}{n(n+1)} f_n^{sh}, \\ t_{n-1}^{sh} &= \frac{\alpha_n}{n}\Big(\frac{\mathrm{d}}{\mathrm{d}r} + \frac{n+1}{r}\Big) f_n^{sh}, \\ t_{n+1}^{sh} &= -\frac{\alpha_{n+1}}{n+1}\Big(\frac{\mathrm{d}}{\mathrm{d}r} - \frac{n}{r}\Big) f_n^{sh}. \end{aligned} \tag{4.21}$$

Here, the $\mathbf{v}$ given by (3.12) satisfies the rigid boundary conditions for the shell and is planar.

From Chapter 3, we know that the p1Y22DM12 and p1q10Y22DM12 flows do not satisfy the no-slip conditions at the OCB. However, using the above transformation, they do satisfy the no-slip conditions at the ICB. The streamlines of the shell flows can be seen in Figures 4.2-4.3 on page 57. These streamlines are similar to the full sphere model.

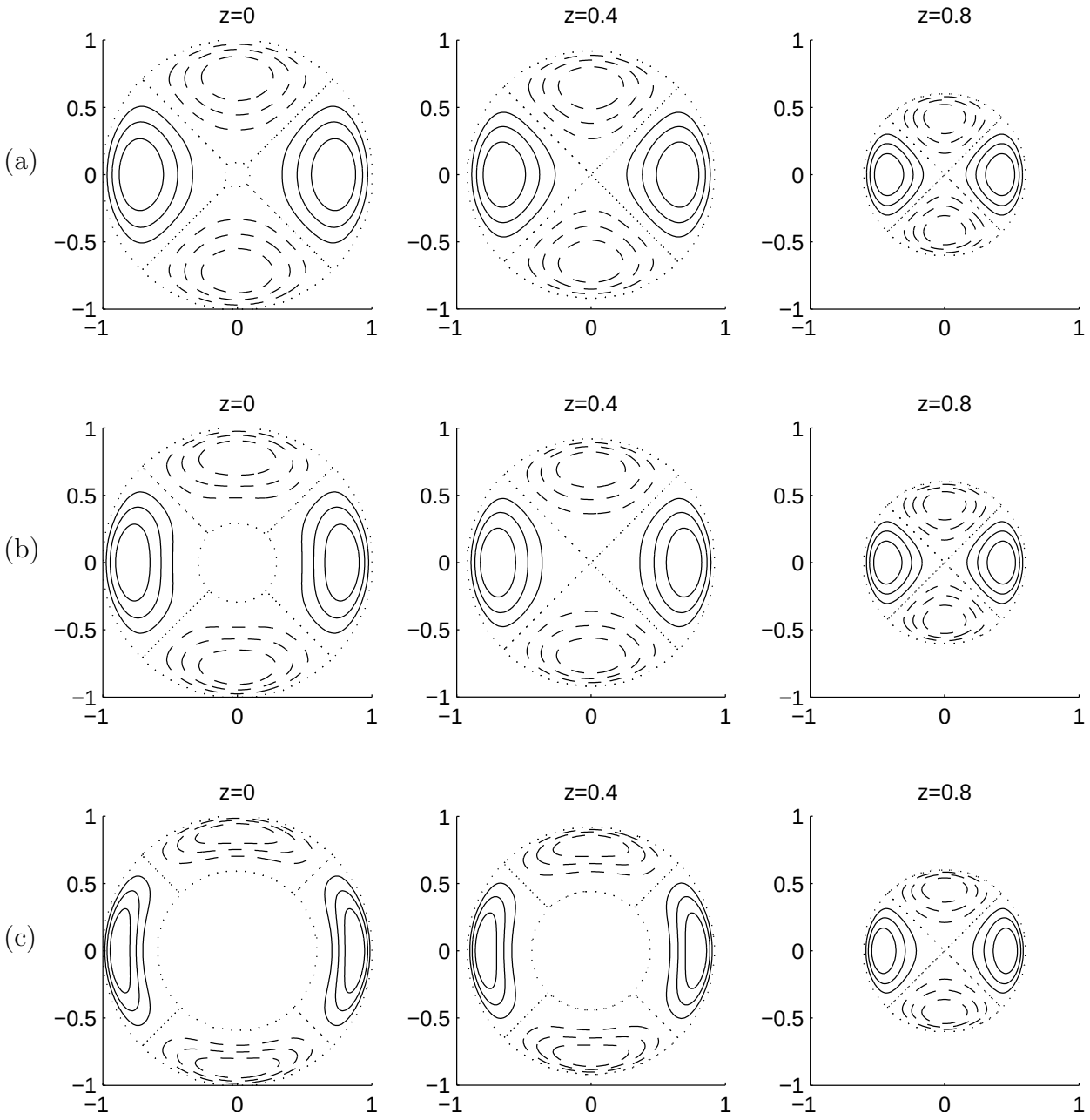

Figure 4.2: the streamlines $f_2^2 = \text{const.}$ for p1Y22DM12 in a spherical shell at $z = 0, 0.4, 0.8$ with:(a) $r_c = 0.1$, (b) $r_c = 0.3$ and (c) $r_c = 0.6$. Solid (dashed) lines represent positive (negative) f_2^2. Flow direction is determined by $v_\phi = -\partial f/\partial\varpi$.

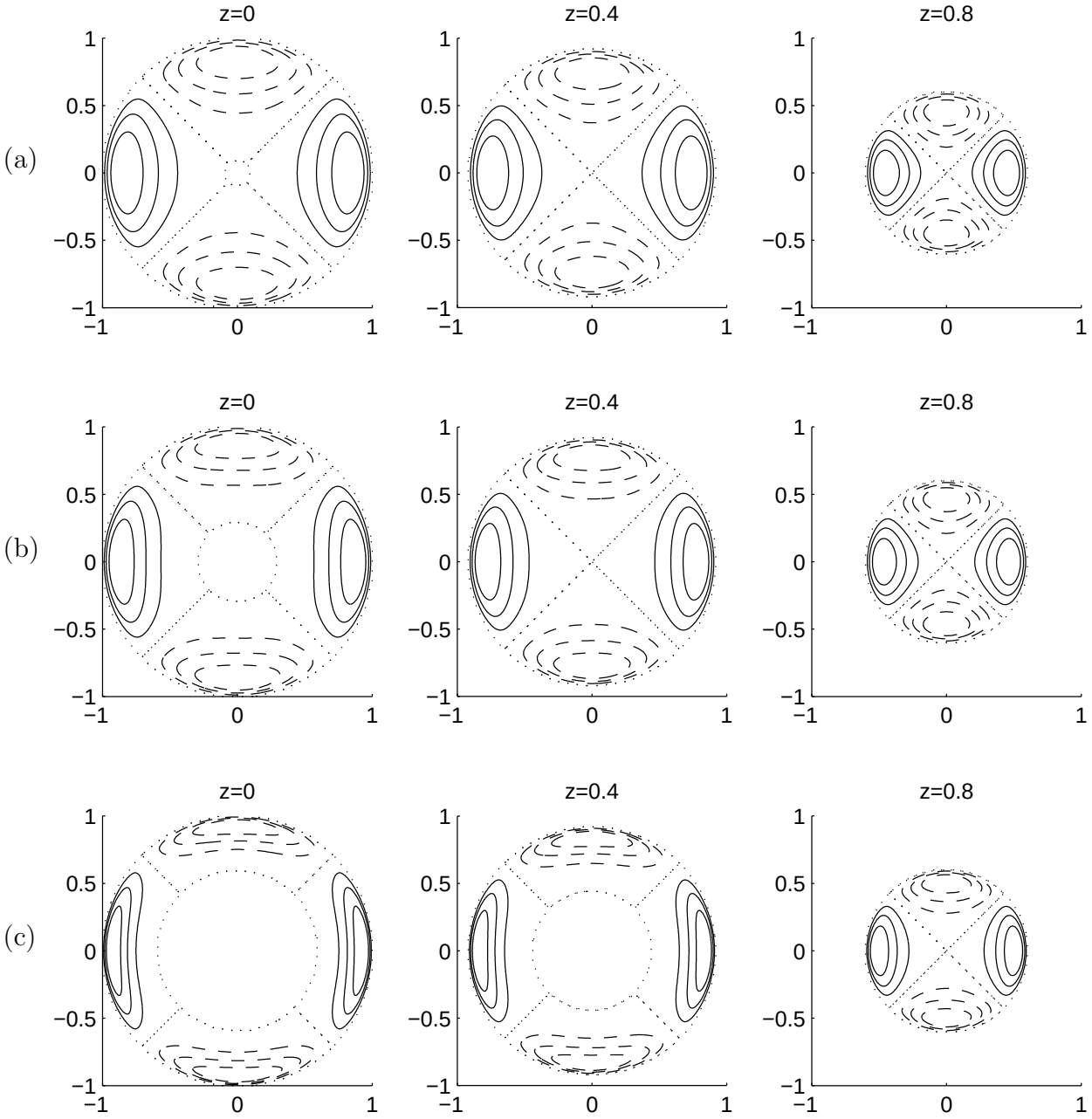

Figure 4.3: the streamlines $f_2^2 = \text{const.}$ for p1q10Y22DM12 in a spherical shell at $z = 0, 0.4, 0.8$ with:(a) $r_c = 0.1$, (b) $r_c = 0.3$ and (c) $r_c = 0.6$. Solid (dashed) lines represent positive (negative) f_2^2. Flow direction is determined by $v_\phi = -\partial f/\partial \varpi$.

4.4.1 Insulating Inner Core Results

Here, we report our results for an insulating inner core, i.e. using boundary conditions (4.4) and (4.5). We began using model p1Y22DM12. First, we searched for the optimum core radius i.e. the core radius that gives us the smallest R_{crit}. The results are in Table 4.3 and Figure 4.4. Based on these results, we concluded that $r_c = 0.24$ is the optimum.

From Figure 4.4, we can see that R_{crit} decreases in $0 \leq r_c \leq 0.24$ and increases afterward. This result differs from the earlier results of Holme and SG. Using different models, they found that R_{crit} increased monotonically with r_c.

Figure 4.5 on page 60 contains $\lambda_{\max}$ profiles of model p1Y22DM12 using various core radii. The matrix band sizes were about 2GB so that we did not need to use our sub-band routine. We can see that the insulating shell models have growing $\lambda_{\max}$ profiles. However, the same convergence problem occurred as in the full sphere model. Also, the convergence becomes worse as r_c increases.

For $r_c = 0.24$, $R_{\text{crit}} \approx 160$. Thus, we investigated this particular model at $R = 170$ using higher $[J, N]$. We can see in Table 4.4 that the convergence has improved compared to p1Y22DM12. However, still higher $[J, N]$ are needed to obtain 1% level of convergence, and we defer this to possible future work.

For model p1q10Y22DM12, we only concentrated on using $r_c = 0.24$. $\lambda_{\max}$ profiles are presented in Figure 4.6. This figure shows that R_{crit} is smaller than that of model p1Y22DM12. However, the convergence problem still exists. So, we have not investigated higher $[J, N]$ for this model.

Core radius	$\lambda_{\max}$
0.10	5.903868719
0.15	7.657371000
0.20	8.664416643
0.22	8.847559000
0.23	8.893496426
0.24	8.909649000
0.25	8.896454000
0.30	8.399736627
0.40	5.152603133
0.50	-2.325973850

Table 4.3: Comparison of $\lambda_{\max}$ for model p1Y22DM12 using different insulating core radii with $R = 220$ and $[J, N] = [400, 25]$ showing that $r_c = 0.24$ is the optimum radius.

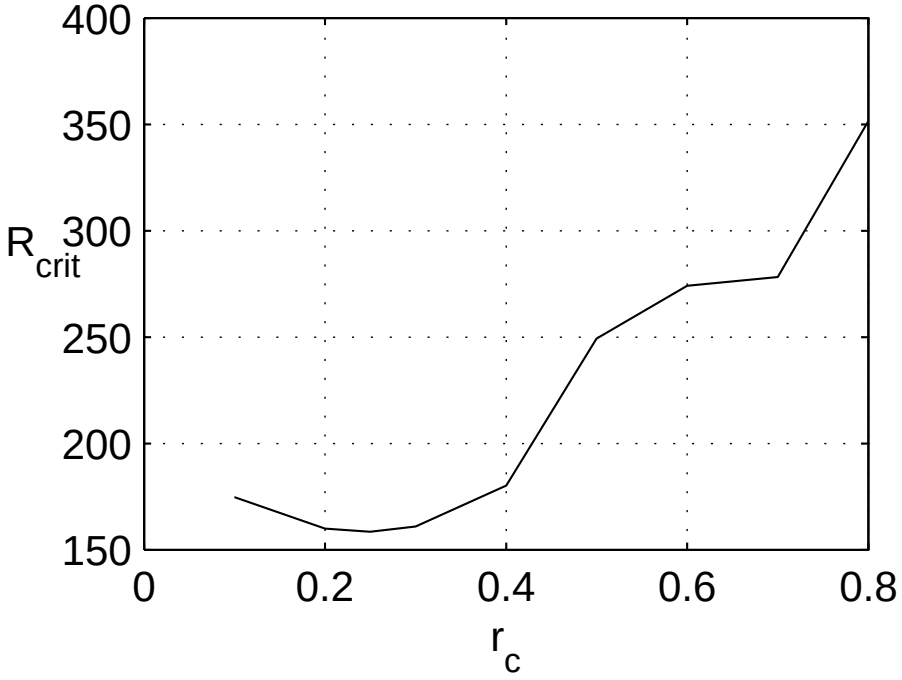

Figure 4.4: R_{crit} for p1Y22DM12 using several different insulating core radii at $[J, N] = [400, 25]$ showing that $r_c = 0.24$ has the lowest R_{crit}.

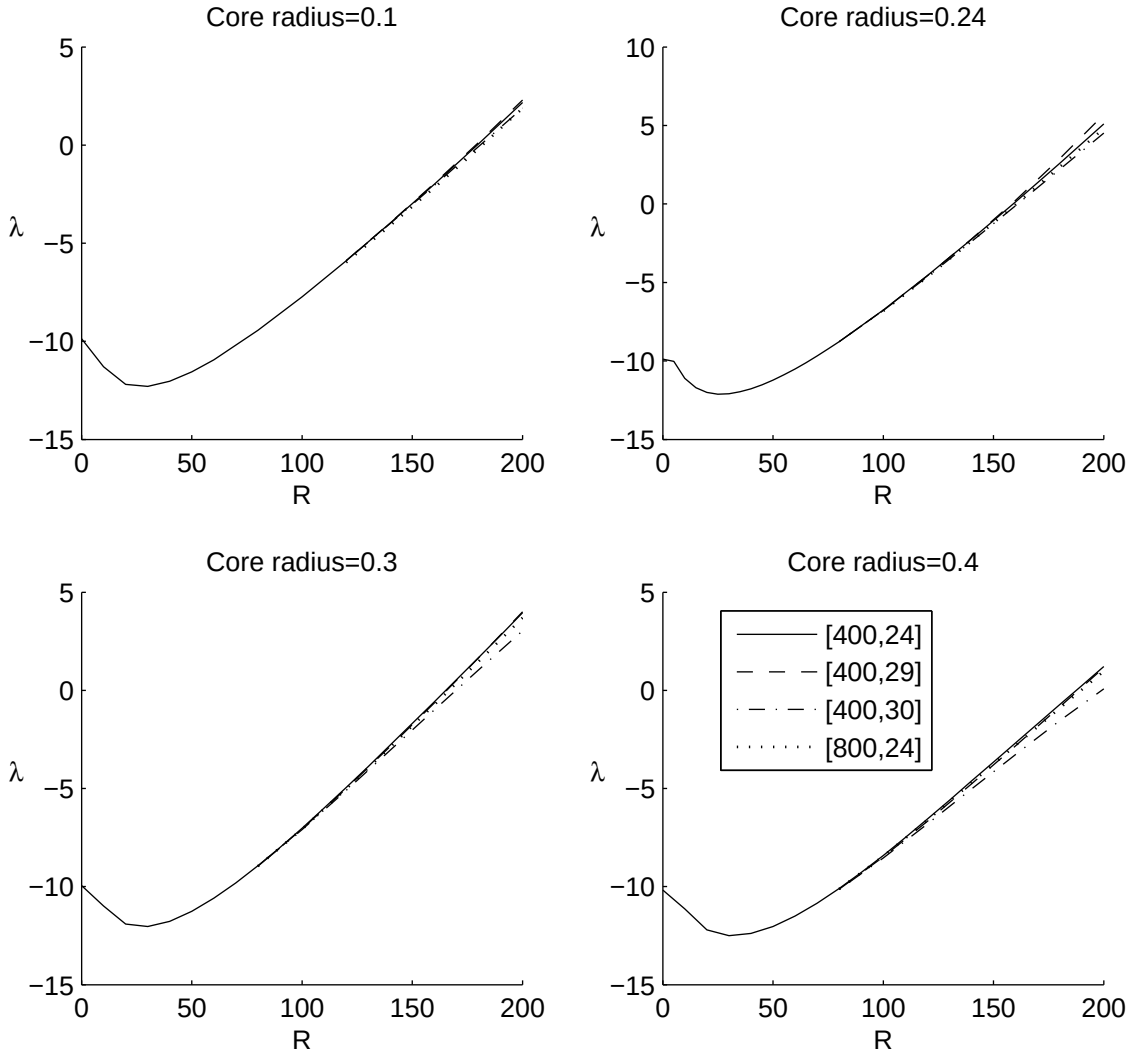

Figure 4.5: $\lambda_{\max}$ for model p1Y22DM12 using an insulating core with $[J, N] = [400, 24], [400, 29], [400, 30], [800, 24]$. The convergence level becomes worse for $R \gtrsim 150$ as we increase r_c.

Core radius	R	J	N	$\Re\{\lambda_{\max}\}$	$\lvert\triangle\lambda_{\max}\rvert/\lambda_{\max}$
0.0	220	400	30	0.979910	11%
			36	0.888190	
		800	36	0.482005	27%
		1600	36	0.380043	
0.24	170	400	30	0.463459	9%
			36	0.509152	
		800	36	0.327397	16%
		1600	36	0.281917	

Table 4.4: Comparison of the change in λ for model p1Y22DM12 at high $[J, N]$. The convergence level with respect to J and N using an insulating inner core with r_c= 0.24 is better than for the full sphere.

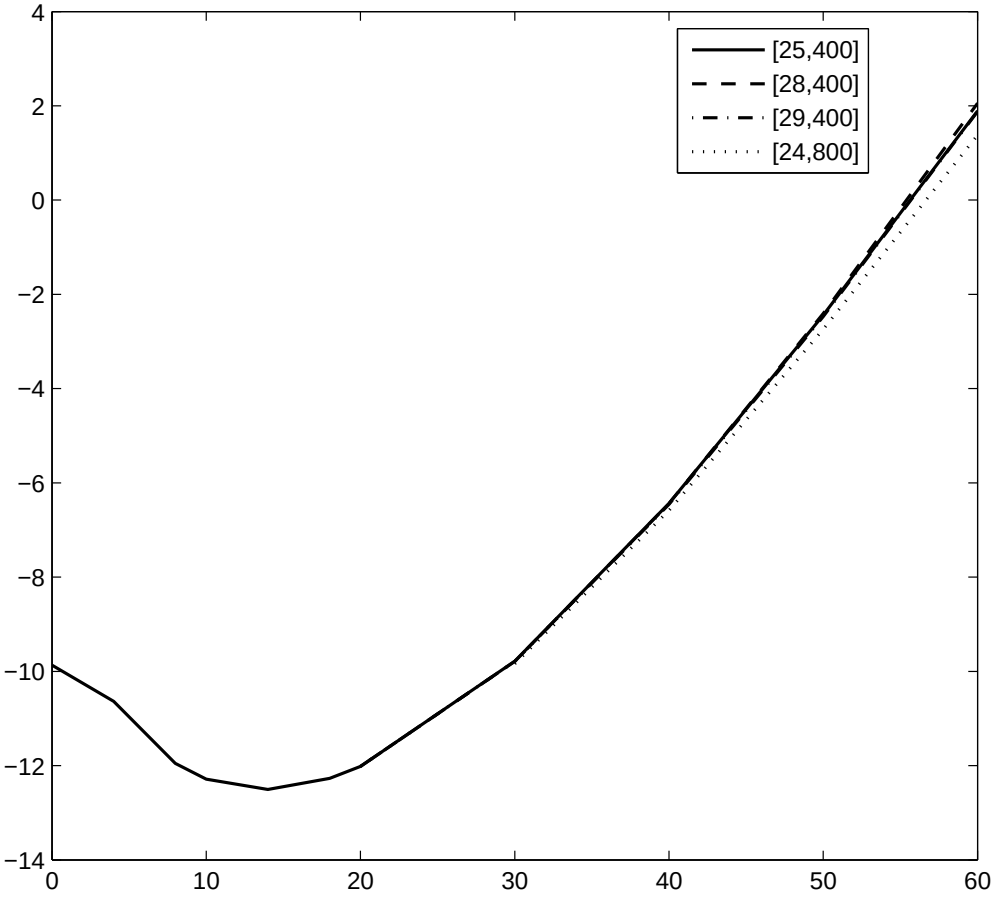

Figure 4.6: $\lambda_{\max}$ for model p1q10Y22DM12 using an insulating core with $[J, N] = [400, 24], [400, 29], [400, 30], [800, 24]$ with $r_c = 0.24$. $R_{\text{crit}} \approx 59$ compared to 160 for model p1Y22DM12 with the same r_c.

4.4.2 Conducting Inner Core Results

Here, we report our results for conducting inner cores, i.e. using method 2 and boundary conditions (4.4) and (4.16). As in the previous section, we seek to find the optimum r_c for model p1Y22DM12. Figure 4.7 shows R_{crit} for model p1Y22DM12 in a spherical shell using various core radii and $[J, N] = [400, 25]$. R_{crit} decreases; its minimum occurs at $r_c \approx 0.6$ before it increases as $r_c \to 1$. In addition, Table 4.5 gives $\lambda_{\max}$ for model p1Y22DM12 in a conducting spherical shell with $R = 220$, various core radii and $[J, N] = [400, 25]$. The Table shows that $\lambda_{\max}$ increases as r_c increases. However, from the earlier insulating results in Figure 4.5 on page 60, $[J, N] = [400, 25]$ may be inadequate for $r_c \gtrsim 0.5$.

Given the above results, we decided to produce $\lambda_{\max}$ profiles using the same $[J, N]$ as in Figure 4.5 on page 60. The results are presented in Figure 4.8. We observe that growing modes exist for all r_c considered, and R_{crit} decreases as r_c increases. However, the convergence deteriorates as r_c increases. This confirms our expectation that $[J, N] = [400, 25]$ is inadequate for $r_c = 0.6$.

We could have attempted to use higher $[J, N]$, but we decided, as with insulating shell models, to concentrate our investigation in a different direction (as in Chapter 5 which follows). For model p1q10Y22DM12, we only performed a preliminary investigation using $r_c = 0.2$. Comparing Figures 4.8 and 4.9, it shows that the convergence improved compared to model p1Y22DM12. Figure 4.8 also shows in spite of convergence difficulties as r_c increases, growing modes persist across all $[J, N]$.

Our results reveal that conducting shells give lower R_{crit} compared to insulating shells. Similar results were also found in non planar velocity dynamos by Bullard and Gubbins (1977).

Core radius	λ
0.1	6.066273
0.2	11.807154
0.3	19.235281
0.4	28.586418
0.5	40.040387
0.6	54.020910
0.7	70.754739
0.8	85.645352

Table 4.5: Comparison of λ for model p1Y22DM12 using different conducting core radii with $R = 220$ and $[J, N] = [400, 25]$ showing that λ increases as we increase r_c.

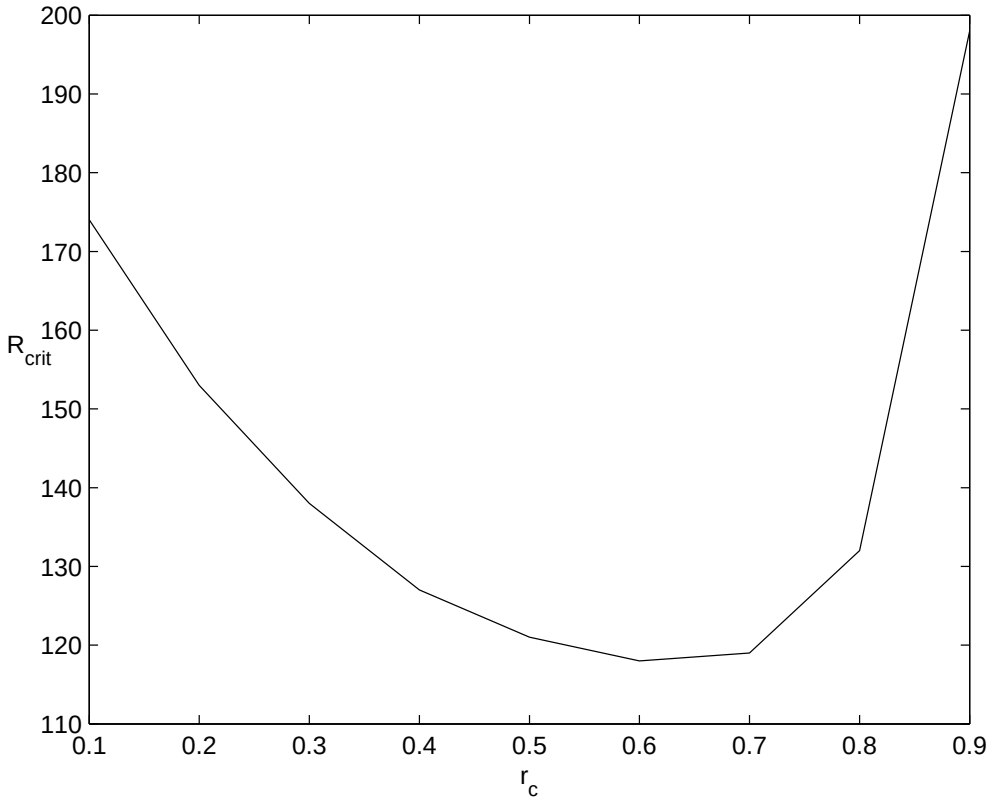

Figure 4.7: R_{crit} for model p1Y22DM12 using different conducting core radii at $[J, N] = [400, 25]$. The model with $r_c = 0.6$ has the lowest R_{crit}.

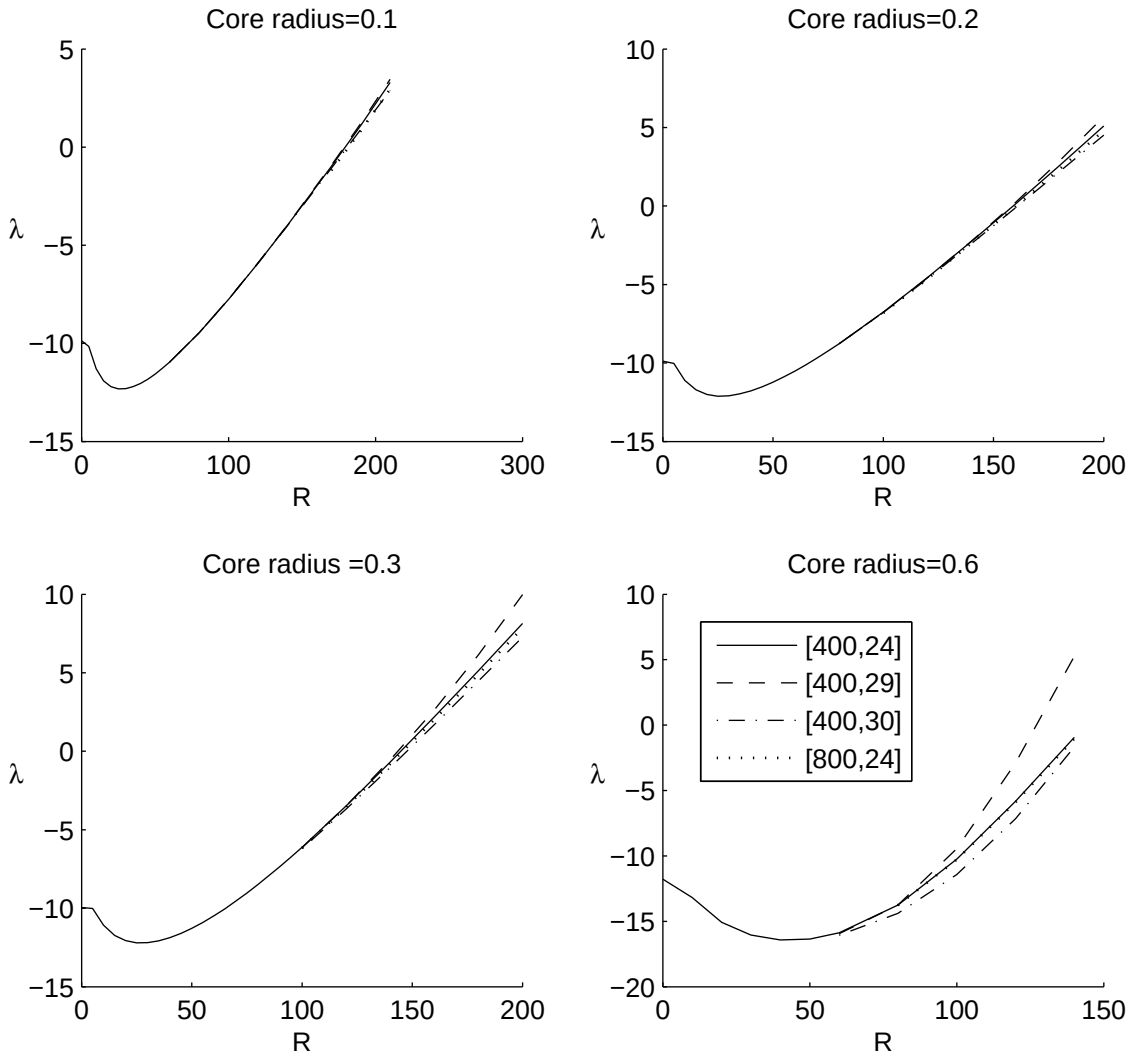

Figure 4.8: $\lambda_{\max}$ for model p1Y22DM12 using conducting cores with $[J, N] = [400, 24], [400, 29], [400, 30], [800, 24]$ showing that these $[J, N]$ are inadequate for the model with $r_c = 0.6$.

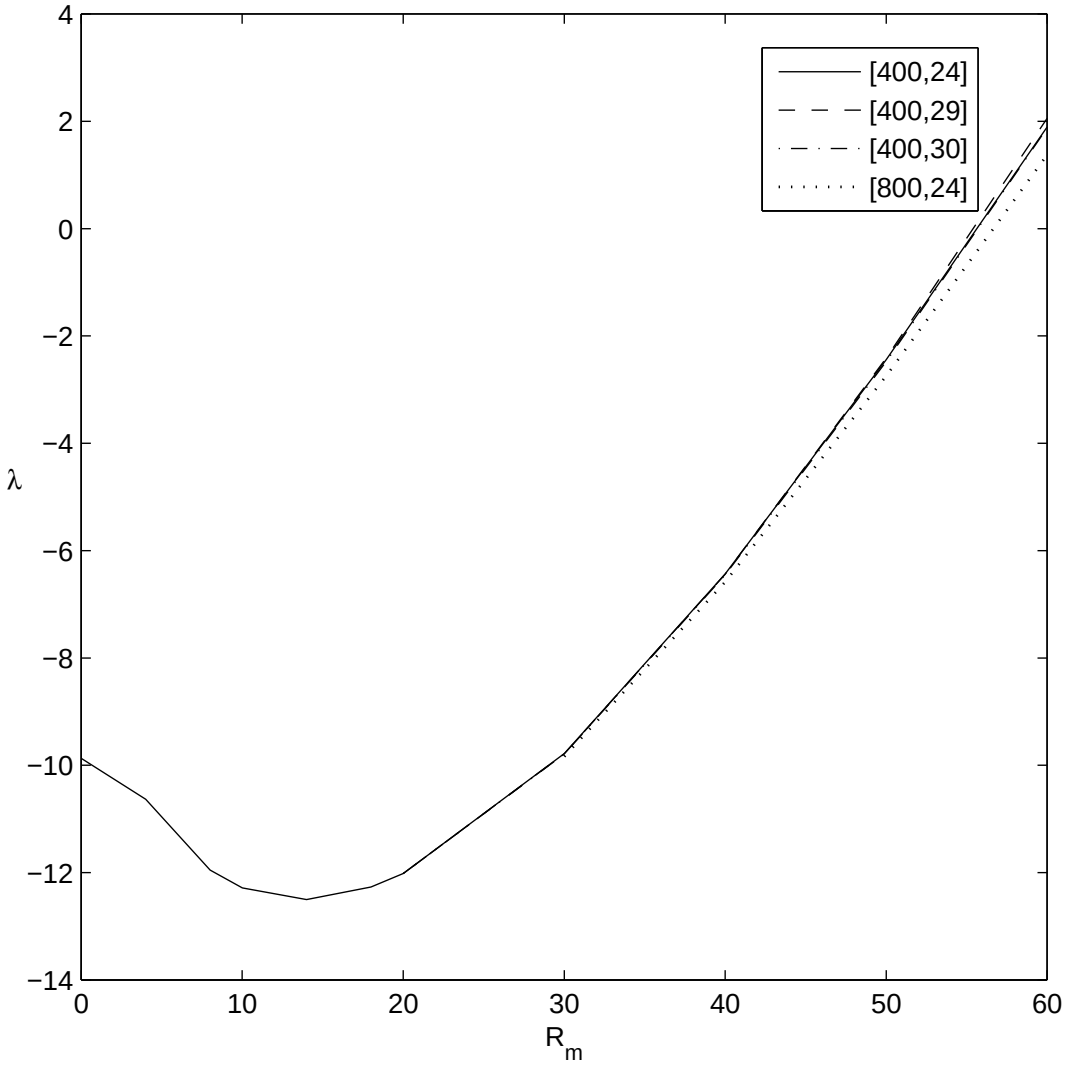

Figure 4.9: $\lambda_{\max}$ for model p1q10Y22DM12 using a conducting core with $[J, N] = [400, 24], [400, 29], [400, 30], [800, 25]$ with $r_c = 0.2$. $R_{\text{crit}} \approx 55$ compared to 160 for model p1Y22DM12 with the same r_c.

4.5 Adding a Constant to The PAS $\mathbf{t}_2^2$ Flow

In this section, we will show how a simple modification of PAS flow results in a fully planarized flow in a shell. In §3.2.2, it was shown that $\mathbf{s}_2^2$ of PAS flow could be planarized by adding a $\mathbf{t}_3^2$ component. Similarly, $\mathbf{s}_2^2$ mapped via transformation (4.18) can be planarized by addition of $\mathbf{t}_3^2$ as shown more generally in §4.4.

Planarization of the PAS t_2^2 is more difficult since, as shown in §3.2.2, the consistency condition (3.10) is not satisfied. However, this condition can be satisfied by a simple modification

$$t_2^2 = K\Lambda^2 j_2(\Lambda r) + C, \tag{4.22}$$

where C is an appropriate constant. But, the resulting flow $\mathbf{t}_2^2$ will be multivalued at $r = 0$. This problem can be overcome by confining the $\mathbf{t}_2^2$ flow to a shell.

Thus, we can construct $\mathbf{s}_3^2$ and $\mathbf{t}_4^2$ to planarize the modified $\mathbf{t}_2^2$. The resulting f_3^2 from (3.9a) is

$$f_3^2 = \frac{3}{\alpha_3} r^{-4} \int_1^r \Big(r^4 \Lambda^2 K j_2(\Lambda r) + r^4 C \Big) \mathrm{d}r, \tag{4.23}$$

which using the identity

$$\frac{\mathrm{d}}{\mathrm{d}r} \frac{1}{\Lambda} r^4 j_3(\Lambda r) = r^4 j_2(\Lambda r),$$

becomes,

$$f_3^2 \;=\; 3\sqrt{7} r^{-4} \Big(\Lambda K (r^4 j_3(\Lambda r) - j_3(\Lambda)) + \frac{C}{5}(r^5 - 1) \Big).$$

The rigid boundary condition (4.20) requires $f_3 = 0$ at $r = r_c$, i.e.

$$C = -\frac{5\Lambda K}{(r_c^5 - 1)} \Big(r_c^4 j_3(\Lambda r_c) - j_3(\Lambda) \Big).$$

Finally given f_3^2, we can use (3.3) to obtain

$$s_3^2 = \frac{\mathrm{i}}{6} f_3^2, \tag{4.24}$$

and (3.8) to obtain

$$t_4^2 = -\frac{\alpha_4}{4} \Big(\frac{\mathrm{d}}{\mathrm{d}r} - \frac{3}{r} \Big) f_3^2. \tag{4.25}$$

Combining all of the components described in this section results in modified PAS flow

$$\mathbf{v} = 2\Re\{(\mathbf{s}_2^2 + \mathbf{t}_3^2) + (\mathbf{t}_2^2 + \mathbf{s}_3^2 + \mathbf{t}_4^2)\}. \tag{4.26}$$

which is planar and satisfies the rigid boundary condition for a shell (4.20). Unfortunately, our numerical investigations only produce decaying magnetic fields so we do not report in detail here. However, our contemplation in this section led us to other planar velocity dynamo investigations which will be discussed in Chapter 5.

4.6 Chapter Summary

The possibility of creating B_z by planar flows results from the jump in $\partial B_z/\partial r$ at the boundary in (2.54). In the successful p1Y22DM12 model of BIJ, the B_z contours are concentrated near the boundary $r = 1$, see BIJ (2006) Figure 4. Thus, we have considered shell dynamos in order to increase the possibility of generating more B_z. We have considered two types of inner core: insulating and conducting.

In §4.2.1, we showed that the ICB for an insulating inner core can be represented by the magnetic boundary condition in (4.5). In §4.2.2, we considered the ICB of a conducting inner core. We discussed that the full sphere approach with $\mathbf{v} = \mathbf{0}$ for $r \leq r_c$ is needed (method 1). For the steady magnetic field, conducting inner core can be represented by the magnetic boundary condition given in (4.16) (method 2). In §4.3, we validated our numerical routine by comparing our results with those of other authors. Interestingly, we found that method 2, although not valid for steady fields, gave quite good agreement to method 1.

Figures 4.5,4.6 and 4.8, show that planar flows in shells can generate and maintain magnetic fields. Indeed, for the shells, R_{crit} is significantly reduced compared to the full sphere model p1Y22DM12 of BIJ. For the shells, the convergence is somewhat better than the full sphere as shown in Table 4.4. Where reasonable convergence is obtained, an optimum r_c exists associated with the lowest R_{crit}.

Finally, in §4.5, we showed that a minor modification allows full planarization of the PAS flow in a shell. Although the resulting magnetic field decays, this modification led us to the subject of Chapter 5 that follows.

Chapter 5

Modified PAS Models

5.1 Introduction

The PAS model was one of the first successful numerical dynamos. This model has low R_{crit} and converges at low $[J, N]$. The PAS flow (3.29) is a Beltrami flow, i.e.

$$\mathbf{v} = k\nabla \times \mathbf{v}, \tag{5.1}$$

where k is a constant. As shown in §3.2.2, the PAS flow cannot be fully planarized by the method of §3.1. The toroidal scalar t_2^2 does not satisfy the consistency condition (3.10).

In this chapter, we establish two modifications of the PAS flow that can be fully planarized in a full sphere.

5.2 BiPAS Models

5.2.1 BiPAS Definition

The biPAS model is defined by the superposition of two PAS flows, i.e.

$$\mathbf{v} = 2\Re\{\mathbf{s}_2^2 + \mathbf{t}_2^2\}, \tag{5.2}$$

where

$$s_2^2 = K\Lambda_i j_2(\Lambda_i r) + CK\Lambda_k j_2(\Lambda_k r), \tag{5.3}$$
$$t_2^2 = K\Lambda_i^2 j_2(\Lambda_i r) + CK\Lambda_k^2 j_2(\Lambda_k r), \tag{5.4}$$

$K = \sqrt{6/5}$, C is a constant, Λ_i and Λ_k are positive roots of $j_2(r)$, and with one of the magnetic chains

$$\begin{aligned}
\text{M02}: &\quad S_1^0, T_1^0, S_2^0, T_2^0, S_2^2, T_2^2, S_3^0, T_3^0, S_3^2, T_3^2, S_4^0, T_4^0, S_4^2, T_4^2, S_4^4, T_4^4, \ldots \\
\text{M12}: &\quad S_1^1, T_1^1, S_2^1, T_2^1, S_3^1, T_3^1, S_3^3, T_3^3, S_4^1, T_4^1, S_4^3, T_4^3, S_5^1, T_5^1, S_5^3, T_5^3, \\
&\quad S_5^5, T_5^5, \ldots
\end{aligned}$$

We use the first three positive roots of $j_2(r)$, which are approximately:

$$\Lambda = 5.3674, 9.0950, 12.3229. \tag{5.5}$$

The flow (5.2) satisfies the rigid boundary condition (2.33), the differentiability conditions (2.40) and (2.41), but not the optional no-slip conditions (2.34). We choose C so that t_2^2 satisfies consistency condition (3.10). Using the identity

$$\int r^{n+1} j_{n-1}(\Lambda r)\,\mathrm{d}r = \frac{1}{\Lambda} r^{n+1} j_n(\Lambda r) + \text{const.}, \tag{5.6}$$

gives

$$\int_0^1 r^4 (K\Lambda_i^2 j_2(\Lambda_i r) + CK\Lambda_k^2 j_2(\Lambda_k r))\,\mathrm{d}r = 0, \tag{5.7}$$

if

$$K(\Lambda_i j_3(\Lambda_i) + C\Lambda_k j_3(\Lambda_k)) = 0, \tag{5.8}$$

which implies,

$$C = -\frac{\Lambda_i j_3(\Lambda_i)}{\Lambda_k j_3(\Lambda_k)}. \tag{5.9}$$

From (5.3), (5.4), and (5.9), it is necessary to have $i \neq k$, in order to avoid free decay. It is easy to show that

$$s_2^2[\Lambda_k, \Lambda_i] = -\frac{\Lambda_k j_3(\Lambda_k)}{\Lambda_i j_3(\Lambda_i)}\; s_2^2[\Lambda_i, \Lambda_k], \tag{5.10}$$

where $s_2^2[\Lambda_i, \Lambda_k] = s_2^2$ in (5.3) and

$$s_2^2[\Lambda_k, \Lambda_i] = K\Lambda_k j_2(\Lambda_k r) + \left(-\frac{\Lambda_k j_3(\Lambda_k)}{\Lambda_i j_3(\Lambda_i)}\right) K\Lambda_i j_2(\Lambda_i r), \tag{5.11}$$

similarly for t_2^2. So, the $\Lambda_i\,\Lambda_k$ combinations that are possible candidates for dynamo are: $\Lambda_1\,\Lambda_2, \Lambda_1\,\Lambda_3, \Lambda_2\,\Lambda_3$.

5.2.2 Planarizing BiPAS

Given the consistency condition (3.10) has now been satisfied, we can fully planarize the biPAS flow (5.2). (As noted in §3.2.2, BIJ were unable to fully planarize the original PAS flow (3.29) on page 34 because it does not satisfy the consistency condition.) Now, we define t_3^2 to planarize s_2^2. From (3.3) and (5.3), we have

$$f_2^2 = -3\mathrm{i}s_2^2 = -3\mathrm{i}K(\Lambda_i j_2(\Lambda_i r) + C\Lambda_k j_2(\Lambda_k r)). \tag{5.12}$$

Thus, using (3.8) and the identity

$$\frac{n}{r}j_n(\Lambda r) - \frac{\mathrm{d}}{\mathrm{d}r}j_n(\Lambda r) = \Lambda j_{n+1}(\Lambda r), \tag{5.13}$$

gives

$$\begin{aligned} t_3^2 &= -\frac{\alpha_3}{3}d_{-2}f_2^2, \\ &= -\alpha_3\ \mathrm{i}K\big(\Lambda_i^2 j_3(\Lambda_i r) + C\Lambda_k^2 j_3(\Lambda_k r)\big). \end{aligned} \tag{5.14}$$

The next step is to planarize the toroidal scalar t_2^2 of the biPAS flow. From (3.9b), we have

$$\begin{aligned} f_3^2 =& \frac{3}{\alpha_3}r^{-4}\int_1^r r^4 t_2^2\,\mathrm{d}r, \\ =& 3\sqrt{7}r^{-4}K\Big[[\Lambda_i r^4 j_3(\Lambda_i r) - \Lambda_i j_3(\Lambda_i)] \\ & - \frac{\Lambda_i j_3(\Lambda_i)}{\Lambda_k j_3(\Lambda_k)}[\Lambda_k r^4 j_3(\Lambda_k r) - \Lambda_k j_3(\Lambda_k)]\Big], \\ =& 3\sqrt{7}\,K\,\Lambda_i\Big(j_3(\Lambda_i r) - \frac{j_3(\Lambda_i)}{j_3(\Lambda_k)}j_3(\Lambda_k r)\Big). \end{aligned} \tag{5.15}$$

Using (3.3) and (3.8)

$$s_3^2 = \frac{\mathrm{i}}{6}f_3^2, \tag{5.16}$$

$$\begin{aligned} t_4^2 &= -\frac{\alpha_4}{4}d_{-3}f_3^2, \\ &= \frac{1}{2}K\sqrt{3}\Lambda_i\left(\Lambda_i j_4(\Lambda_i r) - \frac{j_3(\Lambda_i)}{j_3(\Lambda_k)}\Lambda_k j_4(\Lambda_k r)\right), \end{aligned} \tag{5.17}$$

where $j_3(r)$ is the spherical Bessel function of order 3,

$$j_3(r) = \left(\frac{15}{r^4} - \frac{6}{r^2}\right)\sin r - \left(\frac{15}{r^3} - \frac{1}{r}\right)\cos r, \tag{5.18}$$

and $j_4(r)$ is the spherical Bessel function order 4,

$$j_4(r) = \left(\frac{105}{r^5} - \frac{45}{r^3} + \frac{1}{r}\right)\sin r - \left(\frac{105}{r^4} - \frac{10}{r^2}\right)\cos r. \tag{5.19}$$

Therefore, the fully planarized biPAS model is:

$$\mathbf{v} = 2\Re\{(\mathbf{s}_2^2 + \epsilon_s\mathbf{t}_3^2) + (\mathbf{t}_2^2 + \epsilon_t(\mathbf{s}_3^2 + \mathbf{t}_4^2))\}, \tag{5.20}$$

where $\epsilon_s = \epsilon_t = 1$, with magnetic chains: M02, M12. For arbitrary ϵ_s and ϵ_t, the flow (5.20) satisfies the boundary condition (2.33), the differentiability conditions (2.40) and (2.41), but not the optional no-slip conditions (2.34). In addition to the unplanarized and fully planarized biPAS models, we also investigated the partly planarized version of model biPAS defined by (5.20) with $\epsilon_s = 1, \epsilon_t = 0$ or $\epsilon_s = 0, \epsilon_t = 1$. First, we investigated these models with $R \in [0, 0.4]$. It is easy to show that a rotation through $\Delta\phi = \pi/2$ makes $\lambda(-R) = \lambda(R)$. (The detail of the rotation through $\Delta\phi = \pi/2$ can be found in Dudley (1998)). So, it is not necessary to use $R < 0$. We went beyond this interval if a growing mode was indicated. We used the same m-decoupling of the magnetic chain as in models p1Y22DM12 and p1q10Y22DM12.

5.2.3 Results

For model biPAS, i.e. $\epsilon_s = \epsilon_t = 0$, using all three combinations of Λ_i and Λ_k available in (5.5) gives three new successful dynamos. Table 5.1 shows good convergence of these models. In addition, Figure 5.1 shows growing $\lambda_{\max}$ profiles.

For the partly planarized biPAS, we also find three new successful dynamos using different combinations of Λ_i and Λ_k with $\epsilon_s = 1, \epsilon_t = 0$. Table 5.2 shows good convergence of these models. In addition, Figure 5.2 shows growing $\lambda_{\max}$ profiles. On the other hand, no new dynamo was found if we only planarize the toroidal part t_2^2, i.e. $\epsilon_s = 0, \epsilon_t = 1$ in (5.20).

For the fully planarized biPAS (i.e. $\epsilon_s = \epsilon_t = 1$), we found no growing magnetic fields for $0 \leq R \leq 0.4$ using any combinations of Λ_i and Λ_k. The decay rate of these models at $R = 0.4$ can be seen in Table 5.3. The $\lambda_{\max}$ profile of model $\Lambda_1 \Lambda_2$ is depicted in Figure 5.3. The other $\lambda_{\max}$ profiles are similar to Figure 5.3. Thus, we do not provide them in this thesis.

For all successful dynamos, we found that $\lambda_{\max}$ was real for $0 \leq R \leq 3$. Without any normalization, all R_{crit} were smaller than that of the original PAS model, i.e. $R_{\text{crit}} \approx 0.37$. A more detailed discussion is given later in §5.4.

Model	R	N	$J = 100$	$J = 200$
$\Lambda_1 \Lambda_2$	0.20	11	0.44797	0.45087
		12	0.44801	0.45092
		13	0.44795	0.45086
$\Lambda_1 \Lambda_3$	0.23	15	0.94276	0.94276
		16	0.94272	0.95373
		17	0.94159	0.95261
$\Lambda_2 \Lambda_3$	0.125	11	1.00819	1.01746
		12	1.00827	1.01753
		13	1.00770	1.01697

Table 5.1: $\lambda_{\max}$ for model biPAS with M12 magnetic chain and various Λ_i and Λ_k, showing that these models can act as a dynamo. Model $\Lambda_i \Lambda_k$ means model biPAS (5.2) using the i-th and k-th roots of j_2.

$\Lambda_i\,\Lambda_k$	R	N	$J=100$	$J=200$
$\Lambda_1\,\Lambda_2$	0.22	11	0.85539	0.86114
		12	0.85595	0.86170
		13	0.85402	0.85977
$\Lambda_1\,\Lambda_3$	0.27	15	0.38185	0.36578
		16	0.37130	0.35529
		17	0.36565	0.34969
$\Lambda_2\,\Lambda_3$	0.14	12	0.90915	0.92749
		13	0.89861	0.91698
		14	0.89815	0.91653

Table 5.2: $\lambda_{\max}$ for model partly planarized ($\epsilon_s = 1, \epsilon_t = 0$) biPAS with M12 magnetic chain and various Λ_i and Λ_k. Model $\Lambda_i\,\Lambda_k$ means partly planarized biPAS model using the i-th and k-th roots of j_2.

Model	N	$J=100$	$J=200$
$\Lambda_1\,\Lambda_2$	11	-24.8382	-24.8784
	12	-26.8392	-26.8303
	13	-24.5238	-24.5510
$\Lambda_1\,\Lambda_3$	11	-25.9743	-25.9899
	12	-26.4116	-26.3559
	13	-27.9236	-27.8956
$\Lambda_2\,\Lambda_3$	11	-26.1995	-26.1905
	12	-26.7390	-26.7808
	13	-28.3623	-28.3663

Table 5.3: $\lambda_{\max}$ for model fully planarized biPAS with M12 magnetic chain and various Λ_i and Λ_k, at $R = 0.4$. Model $\Lambda_i\,\Lambda_k$ means fully planarized biPAS (5.20) using the i-th and k-th roots of j_2.

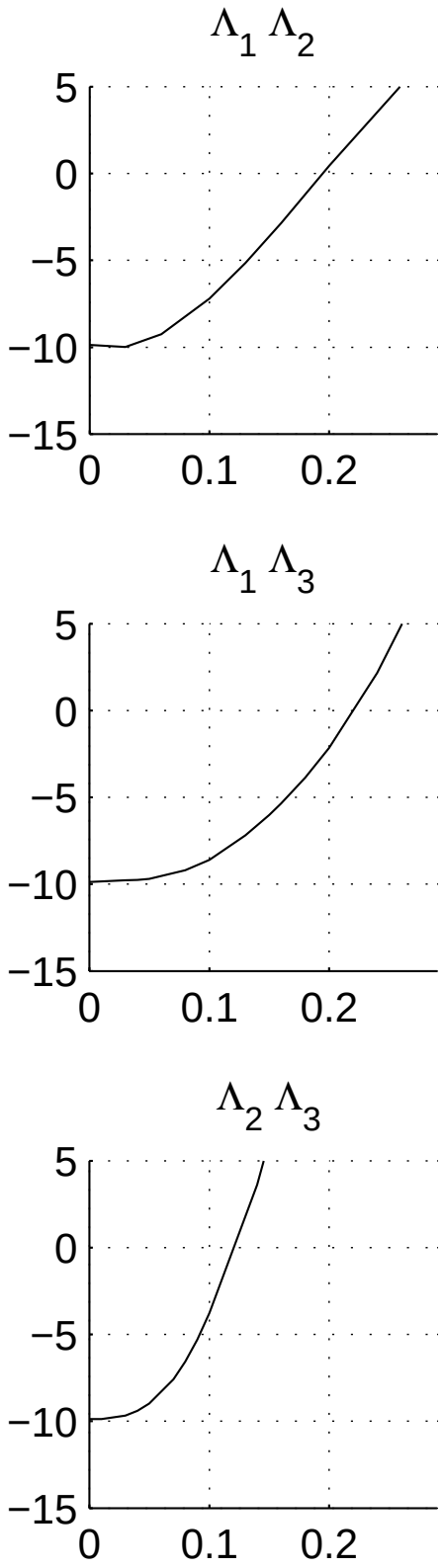

Figure 5.1: $\lambda_{\max}(R)$ profiles for unplanarized biPAS using various Λ_i and Λ_k with $[J, N] = [100, 12]$ and M12 magnetic chain. Model $\Lambda_i\,\Lambda_k$ means unplanarized biPAS using the i-th and k-th roots of j_2.

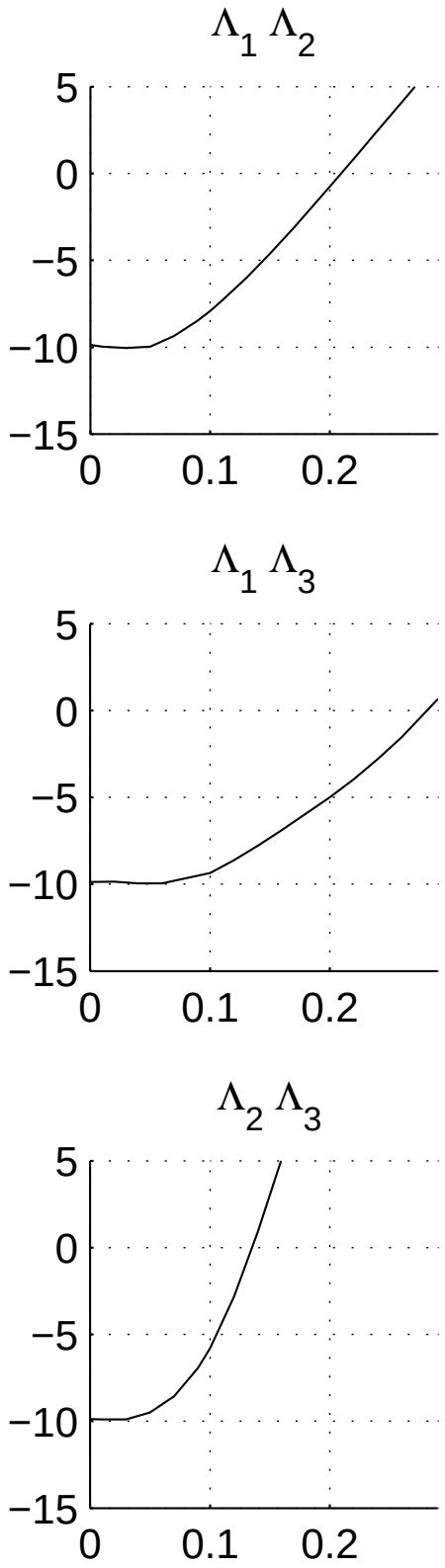

Figure 5.2: $\lambda_{\max}(R)$ profiles for partly planarized biPAS ($\epsilon_s = 1, \epsilon_t = 0$) using various Λ_i and Λ_k with $[J, N] = [100, 12]$ and M12 magnetic chain. Model $\Lambda_i\,\Lambda_k$ means partly planarized biPAS using the i-th and k-th roots of j_2.

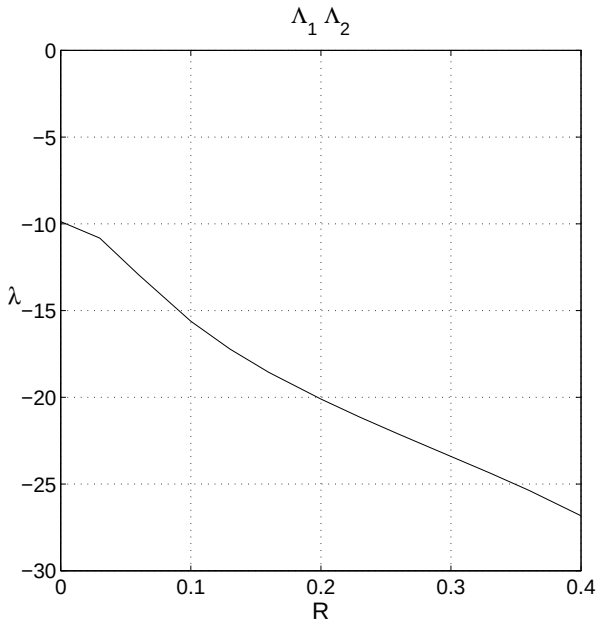

Figure 5.3: $\lambda_{\max}(R)$ profiles for fully planarized biPAS with Λ_1 and Λ_2, $[J, N] = [100, 12]$ and M12 magnetic chain.

5.3 QuasiPAS Models

5.3.1 QuasiPAS Definition

The second modification of PAS is the quasiPAS model defined by

$$\mathbf{v} = 2\Re\{\mathbf{s}_2^2 + \mathbf{t}_2^2\}, \tag{5.21}$$

where

$$s_2^2 = K\Lambda_i j_2(\Lambda_i r), \tag{5.22}$$
$$t_2^2 = K\Lambda_i^2 j_2(\Gamma_k r), \tag{5.23}$$

$K = \sqrt{6/5}$, Λ_i is the i-th root of j_2, Γ_k is the k-th root of j_3, and with one of magnetic chains

$$\begin{aligned}
\text{M02}: &\quad S_1^0, T_1^0, S_2^0, T_2^0, S_2^2, T_2^2, S_3^0, T_3^0, S_3^2, T_3^2, S_4^0, T_4^0, S_4^2, T_4^2, S_4^4, T_4^4, \ldots \\
\text{M12}: &\quad S_1^1, T_1^1, S_2^1, T_2^1, S_3^1, T_3^1, S_3^3, T_3^3, S_4^1, T_4^1, S_4^3, T_4^3, S_5^1, T_5^1, S_5^3, T_5^3, \\
&\quad S_5^5, T_5^5, \ldots
\end{aligned}$$

Here, we use the first three positive roots of j_2 and j_3, which are approximately:

$$\Lambda = 5.3674, 9.0950, 12.3229,$$
$$\Gamma = 6.98793, 10.4171, 13.6980.$$

So, the $\Lambda_i\,\Gamma_k$ combinations that are possible candidates for dynamo are: $\Lambda_1\,\Gamma_1, \Lambda_1\,\Gamma_2, \Lambda_1\,\Gamma_3, \Lambda_2\,\Gamma_1, \Lambda_2\,\Gamma_2, \Lambda_2\,\Gamma_3, \Lambda_3\,\Gamma_1, \Lambda_3\,\Gamma_2, \Lambda_3\,\Gamma_3$. The flow of this model satisfies the boundary condition (2.33), the differentiability conditions (2.40) and (2.41), but not the no-slip conditions (2.34). Furthermore, t_2^2 satisfies the consistency condition (3.10)

$$\begin{aligned}
\int_0^1 r^4 K\Lambda_i^2 j_2(\Gamma_k\, r)\mathrm{d}r &= K\frac{\Lambda_i^2}{\Gamma_k} r^4 j_3(\Gamma_k\, r)\Big|_0^1, \\
&= 0.
\end{aligned} \tag{5.24}$$

5.3.2 Planarizing QuasiPAS

To planarize the poloidal part of the flow s_2^2, we first use (3.3) to obtain

$$f_2^2 = -3\mathrm{i}s_2^2 = -3\mathrm{i}K\Lambda_i j_2(\Lambda_i r).$$

Then, we use (3.8) and (5.13) to obtain

$$t_3^2 = -\frac{\alpha_3}{3} d_{-2} f_2^2 = -\alpha_3 \mathrm{i}K\Lambda_i^2 j_3(\Lambda_i r). \tag{5.25}$$

We planarize t_2^2 using (3.9a),

$$f_3^2 = \frac{3}{\alpha_3} r^{-4} \int_1^r r^4 K \Lambda_i^2 j_2(\Gamma_k r)\, \mathrm{d}r,$$
$$= \frac{3}{\alpha_3} K \frac{\Lambda_i^2}{\Gamma_k} j_3(\Gamma_k r). \tag{5.26}$$

We then use (3.3), (3.8) and (5.13) to obtain

$$s_3^2 = \frac{\mathrm{i}}{6} f_3^2 = \frac{\mathrm{i}}{2\alpha_3} \frac{\Lambda_i^2}{\Gamma_k} K j_3(\Gamma_k r), \tag{5.27}$$

$$t_4^2 = -\frac{\alpha_4}{4} d_{-3} f_3^2 = K \Lambda_i^2 \frac{\sqrt{3}}{2} j_4(\Gamma_k r). \tag{5.28}$$

The fully planarized quasiPAS model is thus defined by

$$\mathbf{v} = 2\Re\{(\mathbf{s}_2^2 + \epsilon_s \mathbf{t}_3^2) + (\mathbf{t}_2^2 + \epsilon_t(\mathbf{s}_3^2 + \mathbf{t}_4^2))\}, \tag{5.29}$$

where $\epsilon_s = \epsilon_t = 1$ and with magnetic chains M02, M12. The flow of this model satisfies the boundary condition (2.33), the differentiability conditions (2.40) and (2.41), but not the no-slip conditions (2.34). Similar to model biPAS, we also consider the partly planarized versions of model quasiPAS where $\epsilon_s = 1, \epsilon_t = 0$ (i.e. planarizing s_2^2 only) or $\epsilon_s = 0, \epsilon_t = 1$ (i.e. planarizing t_2^2 only). Similar to biPAS, we started the investigation of these models using magnetic chain M12, with $R \in [0, 0.4]$.

5.3.3 Results

We found that eight of the nine unplanarized quasiPAS models were successful dynamos. Convergence of $\lambda_{\max}$ was achieved easily at relatively low $[J, N]$ for each case. $\Re\{\lambda_{\max}\} \geq 0$ also converged at relatively low R. Corresponding $\lambda_{\max}$ profiles can be seen in Figure 5.4. It can be seen that all $\lambda_{\max}$ are real except for the $\Lambda_1 \Gamma_1$ model. This model has complex $\lambda_{\max}$ at $R \gtrsim 1.1$. Table 5.4 shows the convergence of $\lambda_{\max}$ for the successful dynamos. The only model that cannot produce a dynamo action is model unplanarized quasiPAS with $\Lambda_1 \Gamma_3$.

For the nine partly planarized quasiPAS with $\epsilon_s = 1, \epsilon_t = 0$, we found five new successful dynamos. Similar to the unplanarized quasiPAS, the $\lambda_{\max}$ are well converged at relatively low $[J, N]$. $\Re\{\lambda_{\max}\} \geq 0$ also converged at relatively low R. Figure 5.5 contains $\lambda_{\max}$ profiles. Model $\Lambda_1 \Gamma_1$ exhibits a mode crossing at $R \approx 0.8$ and has a complex $\lambda_{\max}$ for $R \gtrsim 0.8$. Also, Model $\Lambda_2 \Gamma_2$ exhibits a mode crossing at $R \approx 0.5$ and has a complex $\lambda_{\max}$ for $R \gtrsim 0.5$. Otherwise, all the $\lambda_{\max}$ are real. Table 5.5 shows the convergence of $\lambda_{\max}$ of these models. Using the chosen interval of R and magnetic chain, there was no dynamo found if we planarize the toroidal part t_2^2, i.e. $\epsilon_s = 0, \epsilon_t = 1$ in (5.29).

For fully planarized quasiPAS (i.e. $\epsilon_s = \epsilon_t = 1$), we found no dynamo generated using different combinations of Λ_i and Γ_k in the interval $0 \leq R \leq 0.4$. The convergence of $\lambda_{\max}$ at $R = 0.4$ can be seen in Table 5.6. The $\lambda_{\max}$ profile of model $\Lambda_1 \Gamma_1$

is depicted in Figure 5.6. The other $\lambda_{\max}$ profiles are similar to Figure 5.6. Thus, we do not provide them in this thesis.

Model	R	N	$J = 100$	$J = 200$	$J = 400$
$\Lambda_1\,\Gamma_1$	1.65	15	0.76319(15.5186)	0.76800(15.4650)	
		16	0.76489(15.5163)	0.76971(15.4628)	
		17	0.75943(15.5064)	0.76436(15.4530)	
$\Lambda_1\,\Gamma_2$	2.1	15	1.25098	1.27094	
		16	1.21959	1.23967	
		17	1.24670	1.26565	
$\Lambda_2\,\Gamma_1$	0.28	11	0.54980	0.55255	
		12	0.54975	0.55251	
		13	0.55144	0.55420	
$\Lambda_2\,\Gamma_2$	0.4	11	1.98289	2.00828	
		12	1.97981	2.00522	
		13	1.98667	2.01203	
$\Lambda_2\,\Gamma_3$	1.05	22	0.43719	0.60306	0.64406
		23	0.46125	0.62721	0.66803
		24	0.46070	0.62664	0.66749
$\Lambda_3\,\Gamma_1$	0.25	13	0.51587	0.53019	
		15	0.51327	0.52760	
		16	0.51345	0.52778	
$\Lambda_3\,\Gamma_2$	0.2	13	0.48316	0.49379	
		15	0.48301	0.49364	
		16	0.48301	0.49364	
$\Lambda_3\,\Gamma_3$	0.23	11	0.36786	0.39800	
		12	0.36679	0.39694	
		13	0.36523	0.39539	

Table 5.4: $\lambda_{\max}$ for model quasiPAS with M12 magnetic chain and various Λ_i and Γ_k. Model $\Lambda_i\ \Gamma_k$ means quasiPAS (5.21) using the i-th root of j_2 and k-th root of j_3. The non-zero $\Im\{\lambda_{\max}\}$ are shown in brackets.

Model	R	N	$J = 100$	$J = 200$
$\Lambda_1\,\Gamma_1$	1.50	15	0.76250(23.2700)	0.75926(23.2402)
		16	0.77127(23.2670)	0.76795(23.2372)
		17	0.74650(23.2072)	0.74341(23.1777)
$\Lambda_2\,\Gamma_1$	0.30	11	0.72303	0.72709
		12	0.72483	0.72889
		13	0.72878	0.73283
$\Lambda_2\,\Gamma_2$	0.70	11	5.22681(18.4455)	5.21363(18.4107)
		12	5.10061(18.4951)	5.08767(18.4594)
		13	5.08786(18.0274)	5.07431(17.9913)
$\Lambda_3\,\Gamma_2$	0.22	11	0.53463	0.54966
		12	0.54233	0.55733
		13	0.55314	0.56804
$\Lambda_3\,\Gamma_3$	0.28	11	1.17245	1.26500
		12	1.15481	1.24763
		13	1.12840	1.22081

Table 5.5: $\lambda_{\max}$ for the partly planarized ($\epsilon_s = 1, \epsilon_t = 0$) quasiPAS model with M12 magnetic chain and various Λ_i and Γ_k. Model $\Lambda_i\ \Gamma_k$ means quasiPAS (5.21) using the i-th root of j_2 and k-th root of j_3. The non-zero $\Im\{\lambda_{\max}\}$ are shown in brackets.

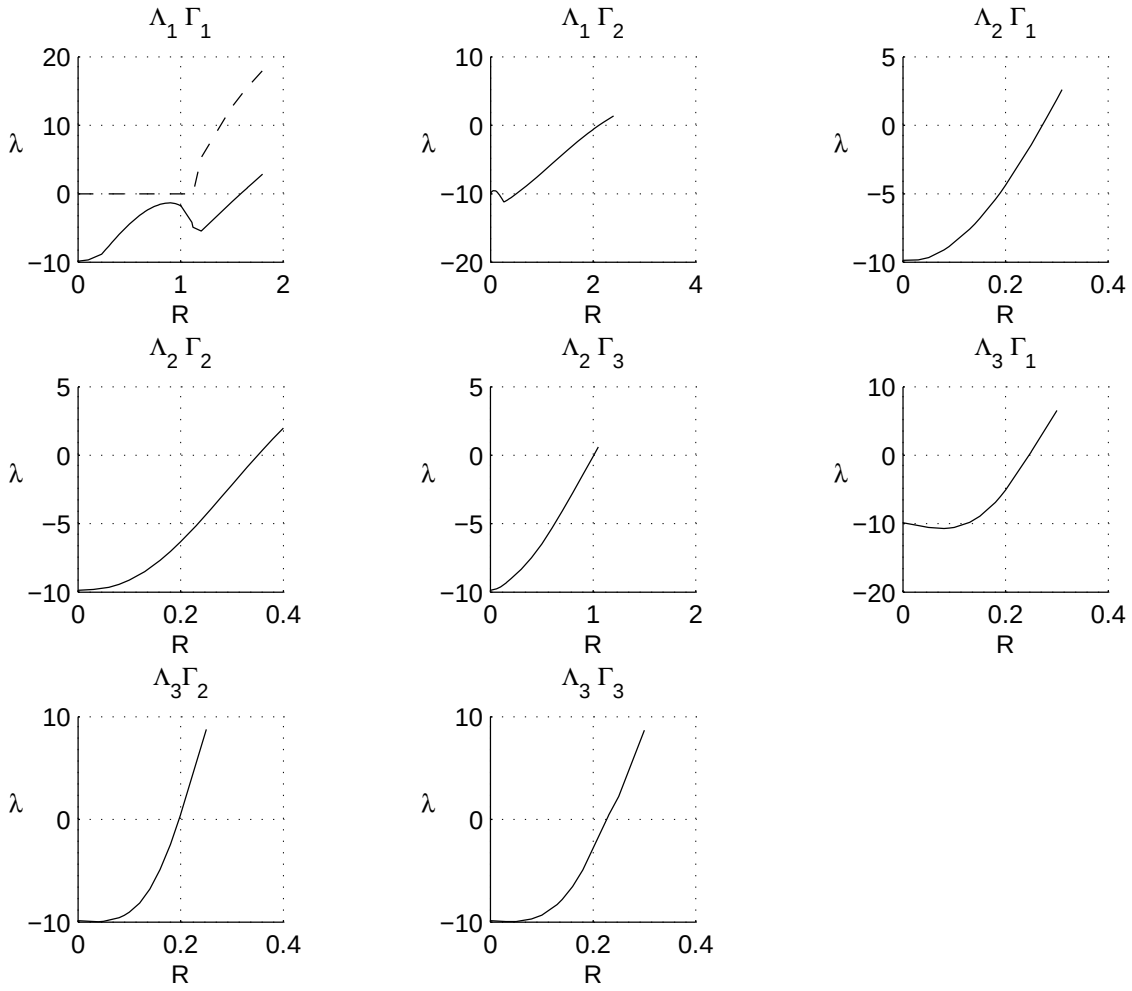

Figure 5.4: $\lambda_{\max}(R)$ profiles for unplanarized quasiPAS using various Λ_i and Γ_k with $[J, N] = [100, 12]$, except for $\Lambda_2\,\Gamma_3$ with $[J, N] = [200, 22]$. Model $\Lambda_1\,\Gamma_1$ has complex $\lambda_{\max}$ at $R \gtrsim 1.1$ represented by dashed line.

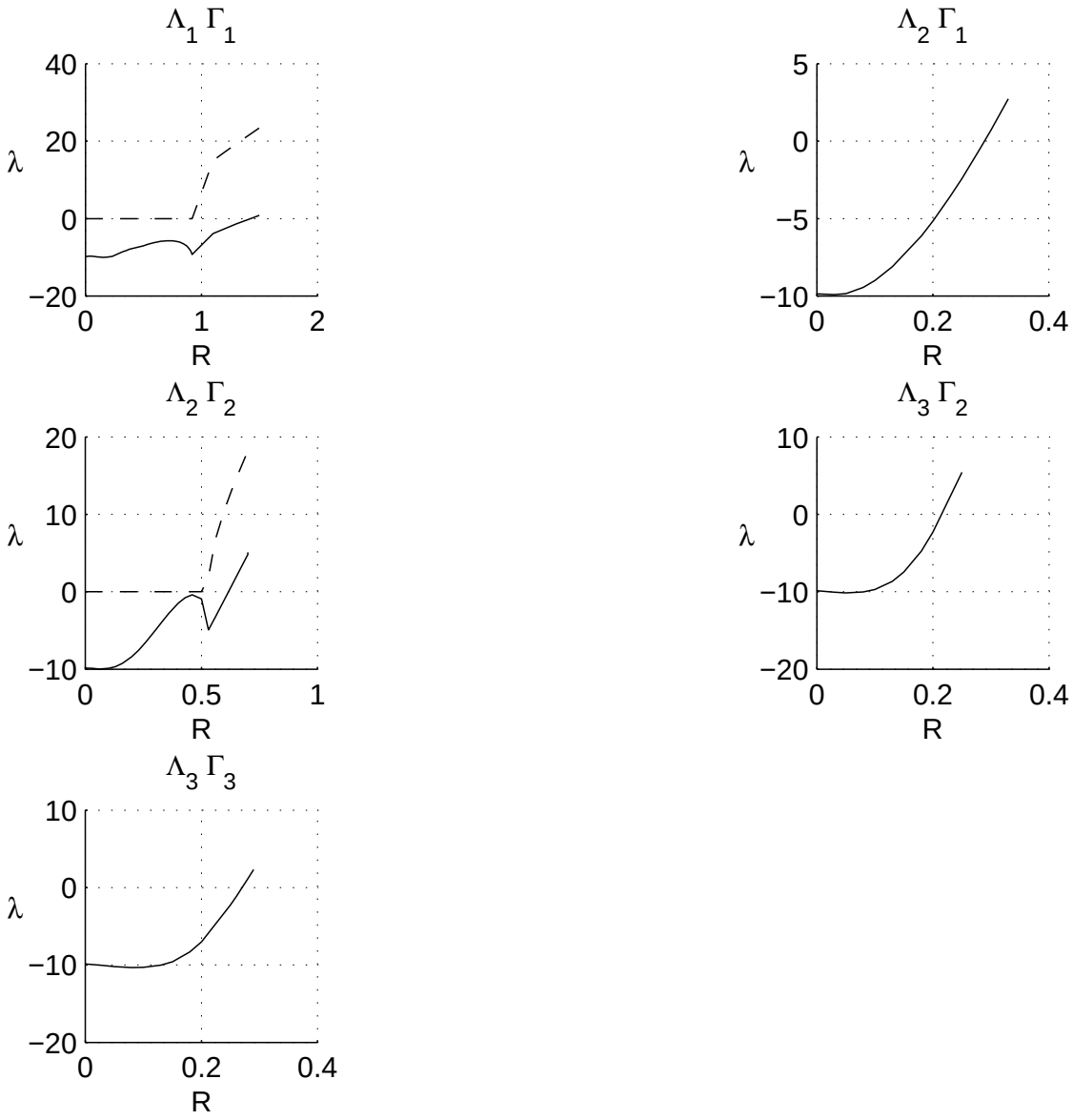

Figure 5.5: $\lambda_{\max}(R)$ profiles for partly planarized quasiPAS ($\epsilon_s = 1, \epsilon_t = 0$) using various Λ_i and Γ_k with $[J, N] = [100, 12]$. Model $\Lambda_1\,\Gamma_1$ and $\Lambda_2\,\Gamma_2$ has complex $\lambda_{\max}$ at $R \gtrsim 0.8$ and $R \gtrsim 0.5$ respectively, represented by dashed line.

Model	N	$J = 100$	$J = 200$
$\Lambda_1\,\Gamma_1$	11	-17.3852	-17.3854
	12	-17.6912	-17.6913
	13	-17.5052	-17.5054
$\Lambda_1\,\Gamma_2$	11	-17.0302	-17.0303
	12	-17.1027	-17.1025
	13	-17.0605	-17.0603
$\Lambda_1\,\Gamma_3$	11	-15.2126	-15.2114
	12	-15.2009	-15.1997
	13	-15.2087	-15.2075
$\Lambda_2\,\Gamma_1$	11	-22.4570	-22.4719
	12	-22.6345	-22.6512
	13	-23.2292	-23.2272
$\Lambda_2\,\Gamma_2$	11	-20.6365	-20.6407
	12	-20.5597	-20.5631
	13	-20.6645	-20.6659
$\Lambda_2\,\Gamma_3$	11	-20.6310	-20.6311
	12	-20.4188	-20.4194
	13	-20.5398	-20.5398
$\Lambda_3\,\Gamma_1$	11	-14.0506	-14.1939
	12	-15.0011	-15.0295
	13	-16.9940	-17.0563
$\Lambda_3\,\Gamma_2$	11	-25.6350	-25.7109
	12	-24.9181	-24.9563
	13	-26.1947	-26.2533
$\Lambda_3\,\Gamma_3$	11	-22.2624	-22.2769
	12	-23.0515	-23.0562
	13	-22.6904	-22.6958

Table 5.6: $\lambda_{\max}$ for fully planarized quasiPAS with M12 magnetic chain and various Λ_i and Γ_k, at $R = 0.4$. Model $\Lambda_i\,\Gamma_k$ means fully planarized quasiPAS (5.21) using the i-th root of j_2 and k-th root of j_3.

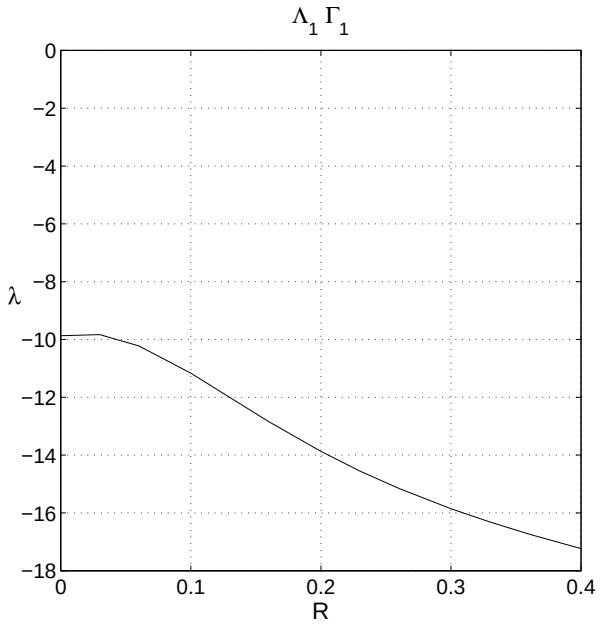

Figure 5.6: $\lambda_{\max}(R)$ profiles for fully planarized quasiPAS with Λ_1 and Γ_1, $[J, N] = [100, 12]$ and M12 magnetic chain.

5.4 R_{crit} Comparison

Here, we compare R_{crit} of the unplanarized and partly planarized biPAS and quasiPAS models. As in Chapter 3, we normalized the R_{crit} using rms($\mathbf{v}$) and max $|\mathbf{v}|$. The numerical results are presented in Tables 5.7 and 5.8. Our results reveal that fourteen out of nineteen new successful dynamos have lower normalized R_{crit}, using both normalization, than that of the original PAS model in equation (3.29). Three of the unplanarized quasiPAS have higher normalized R_{crit} than that of PAS. We note that partly planarized quasiPAS models with $\Lambda_1\ \Gamma_1$ and $\Lambda_2\ \Gamma_2$ are exceptional: the order of R_{crit} is reversed for the two normalizations. Unlike PAS flow, the biPAS and quasiPAS flows are not Beltrami flows. This shows that flows that do not have strong helicity can produce a dynamo at lower R compared to a Beltrami flow. These results are contrary to our expectation, since earlier researchers (e.g. Parker (1955) and Moffat (1970)) argued that it is an advantage for dynamo action to have strong helicity, $\mathbf{v} \cdot \nabla \times \mathbf{v}$.

Model	R_{crit}	Normalized R_{crit}	
		rms($\mathbf{v}$)	max $\|\mathbf{v}\|$
PAS	0.37	29.67	113.15
biPAS			
$\Lambda_1\ \Lambda_2$	0.19	12.83	41.09
$\Lambda_1\ \Lambda_3$	0.22	18.77	56.55
$\Lambda_2\ \Lambda_3$	0.12	11.86	54.59
quasiPAS			
$\Lambda_1\ \Gamma_1$	1.60	52.58	116.45
$\Lambda_1\ \Gamma_2$	2.10	61.60	162.37
$\Lambda_2\ \Gamma_1$	0.27	17.85	43.64
$\Lambda_2\ \Gamma_2$	0.35	19.20	62.14
$\Lambda_2\ \Gamma_3$	1.00	49.84	190.50
$\Lambda_3\ \Gamma_1$	0.25	27.54	79.25
$\Lambda_3\ \Gamma_2$	0.19	16.51	54.01
$\Lambda_3\ \Gamma_3$	0.23	17.49	74.04

Table 5.7: Normalized R_{crit} for PAS, biPAS and quasiPAS.

Model	R_{crit}	Normalized R_{crit}	
		rms($\mathbf{v}$)	max $\|\mathbf{v}\|$
biPAS			
$\Lambda_1\ \Lambda_2$	0.21	15.16	44.15
$\Lambda_1\ \Lambda_3$	0.27	24.63	74.68
$\Lambda_2\ \Lambda_3$	0.14	14.79	61.80
quasiPAS			
$\Lambda_1\ \Gamma_1$	1.42	50.54	96.30
$\Lambda_2\ \Gamma_1$	0.28	19.52	54.31
$\Lambda_2\ \Gamma_2$	0.60	35.50	99.86
$\Lambda_3\ \Gamma_2$	0.22	20.24	73.86
$\Lambda_3\ \Gamma_3$	0.27	22.11	81.97

Table 5.8: Normalized R_{crit} for partly planarized biPAS and quasiPAS.

5.5 Chapter Summary

In §4.5 on page 66, we modified the PAS flow so that the new flow could be planarized within a spherical shell. In this chapter, we modified the PAS flow into two new flows: biPAS and quasiPAS flows. These flows can be planarized in a sphere.

All the three unplanarized biPAS models were found to be successful dynamos. We also found that three of the six possible partly planarized biPAS models were successful dynamos. $\lambda_{\max}$ converged well at relatively low $[J, N]$, and $\Re\{\lambda_{\max}\} \geq 0$ converged at relatively low R. Tables 5.1–5.2 show the convergence of these successful dynamos. The $\lambda_{\max}$ profiles of these successful dynamos can be seen in Figures 5.1–5.2. However, we could not find any of the fully planarized biPAS models that acted as a dynamo in the interval $0 \leq R \leq 0.4$. Table 5.3 shows the decay rate of the fully planarized biPAS models at $R = 0.4$.

Of nine quasiPAS models, we found eight new successful dynamos and of the eighteen partly planarized models, we found five new successful dynamos. For the successful dynamos, $\lambda_{\max}$ converged well at relatively low $[J, N]$, and $\Re\{\lambda_{\max}\} \geqslant 0$ converged at relatively low R. The change in $\lambda_{\max}$ can be seen in Tables 5.4–5.5. Corresponding $\lambda_{\max}$ profiles can be seen in Figures 5.4–5.5. Similar to biPAS, no fully planarized quasiPAS models were found to act as dynamos in the interval $0 \leq R \leq 0.4$. The decay rates of these models can be seen in Table 5.6.

It is interesting to note that the successful partly planarized biPAS and quasiPAS models, all resulted from planarizing the poloidal part of the flow and leaving the toroidal part unplanarized. In contrast, we do not find any dynamos if we planarize the toroidal part only.

We found that most R_{crit} of the successful dynamos were lower than that of the original PAS model. Our lowest R_{crit}, without any normalization, is 0.12 which is a significant improvement compared to 0.37 for PAS. Our results reveal that the fourteen out of nineteen new dynamos perform better that the PAS dynamo, even though they are not Beltrami flows.

Chapter 6

The Convergence of Kinematic Dynamos

Although we are convinced that models p1Y22DM12 and p1q10Y22DM12 do act as dynamos, the relative change of $\lambda_{\max}$, shown in Table 3.2 on page 39 and Table 3.5 on page 46 is about 1–5%. Also, our use of spherical shells in Chapter 4 did not significantly improve the convergence of $\lambda_{\max}$. Therefore, in this chapter, we provide additional convergence evidence that planar flows can maintain a magnetic field.

Various convergence tests have been used by earlier researchers (e.g. Gubbins (1973), KR, DJ). Most researchers used the change in $\lambda_{\max}$ as a convergence test. Some researchers also use the eigenvector elements (i.e. the elements of $\mathbf{x}$ in (2.38) on page 20) to indicate convergence. Gubbins (1973) stated that the change in the higher harmonics of the eigenvector is a better test than the change in $\lambda_{\max}$. Later, DJ introduced another test based on the root-mean-square of $\mathbf{B}$ over spherical surfaces regarded as a function of r.

In this chapter we discuss the above convergence tests and introduce two new tests: SRMS and VRMS. We compare the various tests based on sensitivity and convenience and apply them to models p1Y22DM12 and p1q10Y22DM12.

6.1 Some Existing Tests for Convergence

6.1.1 The Eigenvalue (λ) Test

In this test, values of $\lambda_{\max}(J, N, R)$ are first calculated. Then, we can tabulate and plot them in various ways. For visual presentation, we can plot $\lambda_{\max}(R)$ for various $[J, N]$ as in Figures 3.2–3.3 on page 35. Alternatively, we can plot $\lambda_{\max}(N)$ for various J and a fixed R as in Figure 3.5 on page 40 and Figure 3.13 on page 46. We

can also plot $\lambda_{\max}(h^2)$ for various N where $h = 1/J$ at fixed R as in Figure 3.6 on page 40 and Figure 3.14 on page 47.

In most work, tables of $\lambda_{\max}$ are used to demonstrate convergence. In this chapter to quantify convergence, we calculate the absolute difference (AD)

$$\mathrm{AD}(\lambda_{\max}) := |\lambda_{\max}(J_2, N_2) - \lambda_{\max}(J_1, N_1)|,$$

where $[J_1, N_1], [J_2, N_2]$ are two different truncation levels at fixed R with $J_2 = J_1 + \Delta J, N_2 = N_1 + \Delta N$ and $\Delta J, \Delta N \geq 0$.
We also calculate the mixed difference (MD)

$$\mathrm{MD}(\lambda_{\max}) := \mathrm{AD}(\lambda_{\max})/(1 + |\lambda_{\max}(J_2, N_2)|),$$

and the relative difference (RD)

$$\mathrm{RD}(\lambda_{\max}) := \mathrm{AD}(\lambda_{\max})/|\lambda_{\max}(J_2, N_2)|.$$

6.1.2 The Eigenvector (S, T) Test

For this test, we need the eigenvector in (2.38) on page 20 which has element

$$X := S_n^m(r_j) \text{ or } T_n^m(r_j),$$

where $r_j = jh; j = 1, \ldots, J$. We normalized the eigenvector to make the element with maximum magnitude equal to 1. (The first-found element with maximum magnitude was used) Earlier researchers used this method to indicate convergence by comparing visually the graphs of $X(r_j)$ for each n, m at two different truncation levels (see Gubbins (1973), KR, Dudley (1988)).

We attempt to quantify this test by calculating the maximum absolute difference (MAD)

$$\mathrm{MAD}(X) := \max_{S,T,j,n,m} |X(J_2, N_2) - X(J_1, N_1)|,$$

the maximum mixed difference (MMD)

$$\mathrm{MMD}(X) := \max_{S,T,j,n,m} |X(J_2, N_2) - X(J_1, N_1)|/(1 + |X(J_2, N_2)|),$$

and the maximum relative difference (MRD)

$$\mathrm{MRD}(X) := \max_{S,T,j,n,m} |X(J_2, N_2) - X(J_1, N_1)|/|X(J_2, N_2)|.$$

However, we found MRD to be impractical because some $|X| \lll 1$, which made $\mathrm{MRD}(X) \ggg 1$, even when $\mathrm{RD}(\lambda_{\max}) < 1\%$.

6.1.3 The Vector Field (B) Test

For given $\lambda = \mu + \mathrm{i}\,\omega$ and $\overline{\lambda} = \mu - \mathrm{i}\,\omega$, the λ contribution to $\mathbf{B}$ is

$$\mathbf{B} = (\mathbf{B}_\lambda e^{\lambda t} + \mathbf{B}_{\overline{\lambda}}\, e^{\overline{\lambda} t})/(1+\delta^0_\omega), \tag{6.1}$$

$$= e^{\mu t}\Big((\mathbf{B}_\lambda + \mathbf{B}_{\overline{\lambda}})\cos(\omega t) + \mathrm{i}(\mathbf{B}_\lambda - \mathbf{B}_{\overline{\lambda}})\sin(\omega t)\Big)/(1+\delta^0_\omega), \tag{6.2}$$

where $\mathbf{B}_{\overline{\lambda}} = \overline{\mathbf{B}_\lambda}$. For real λ, we only need to consider the first term of (6.2) since $\mathbf{B}_\lambda = \mathbf{B}_{\overline{\lambda}}$. In this chapter, we only use models that have real eigenvalues. To be comparable to other tests, we normalized $\mathbf{B}$ such that $|\mathbf{B}| = 1$ at $t = 0$.

For visual comparison, we can plot contours of B_r, B_θ, B_ϕ in planes ϕ = const. and planes z = const. BIJ used such contours to infer convergence for model p1Y22DM12. In addition, for quantitative comparison, we calculate the maximum absolute difference (MAD)

$$\mathrm{MAD}(\mathbf{B}) := \max_\xi |B_\xi(J_2, N_2) - B_\xi(J_1, N_1)|,$$

the maximum mixed difference (MMD)

$$\mathrm{MMD}(\mathbf{B}) := \max_\xi \frac{|B_\xi(J_2, N_2) - B_\xi(J_1, N_1)|}{1 + |B_\xi(J_2, N_2)|},$$

where $\xi = r, \theta, \phi$. We do not use MRD because we found the same problem as in the (S, T) test.

6.2 Surface Root Mean Square (SRMS) Tests

6.2.1 Definition

This is our first new test. From (6.1),

$$\mathbf{B}^2 = e^{2\mu t}\Big(\mathbf{B}_\lambda^2 e^{2\omega i t} + \mathbf{B}_{\bar{\lambda}}^2 e^{-2\omega i t} + 2\mathbf{B}_\lambda \cdot \mathbf{B}_{\bar{\lambda}}\Big)/(1+\delta^0_\omega).$$

Consideration of the weighted average of $\mathbf{B}^2$ over time span $\tau = \pi/\omega$

$$\frac{1}{\tau}\int_0^\tau \mathbf{B}^2 e^{-2\mu t}\mathrm{d}t \;\; = \;\; \mathbf{B}_\lambda \cdot \mathbf{B}_{\bar{\lambda}}\,(2 - \delta^0_\omega),$$

led us to define the SRMS quantities

$$\mathrm{srms}\mathbf{B}(r) = \Big(\frac{1}{4\pi}\int_{4\pi} \mathbf{B}_\lambda \cdot \mathbf{B}_{\overline{\lambda}}\,\sin\theta\,\mathrm{d}\theta\,\mathrm{d}\phi\Big)^{\frac{1}{2}}, \tag{6.3}$$

$$\mathrm{srms}\mathbf{B}(\theta) = \Big(\frac{1}{\pi}\int_0^1\int_0^{2\pi} \mathbf{B}_\lambda \cdot \mathbf{B}_{\overline{\lambda}}\,r\,\mathrm{d}\phi\,\mathrm{d}r\Big)^{\frac{1}{2}}, \tag{6.4}$$

$$\mathrm{srms}\mathbf{B}(\phi) = \Big(\frac{2}{\pi}\int_0^1\int_0^\pi \mathbf{B}_\lambda\cdot\mathbf{B}_{\overline{\lambda}}\, r\,\mathrm{d}\theta\,\mathrm{d}r\Big)^{\frac{1}{2}}. \tag{6.5}$$

The factor $(2-\delta^0_\omega)$ has been dropped since we only consider real eigenvalues ($\omega = 0$).

$\mathrm{srms}\mathbf{B}(r)$ is an average over the spherical surface

$$r = \text{const.}, \quad 0 \le \theta \le \pi, \quad 0 \le \phi \le 2\pi;$$

$\mathrm{srms}\mathbf{B}(\theta)$ is an average over the conical surface

$$\theta = \text{const.}, \quad 0 \le r \le 1, \quad 0 \le \phi \le 2\pi;$$

and $\mathrm{srms}\mathbf{B}(\phi)$ is an average over the semi-circular surface

$$\phi = \text{const.}, \quad 0 \le \theta \le \pi, \quad 0 \le r \le 1.$$

The associated SRMS of $\mathbf{B}$ components are

$$\mathrm{srmsB}_\xi(r) = \Big(\frac{1}{4\pi}\int_{4\pi} B_{\xi\lambda}B_{\xi\bar{\lambda}}\,\sin\theta\,\mathrm{d}\theta\,\mathrm{d}\phi\Big)^{\frac{1}{2}}, \tag{6.6}$$

$$\mathrm{srmsB}_\xi(\theta) = \Big(\frac{1}{\pi}\int_0^1\int_0^{2\pi} B_{\xi\lambda}B_{\xi\bar{\lambda}}\,r\,\mathrm{d}\phi\,\mathrm{d}r\Big)^{\frac{1}{2}}, \tag{6.7}$$

$$\mathrm{srmsB}_\xi(\phi) = \Big(\frac{2}{\pi}\int_0^1\int_0^{\pi} B_{\xi\lambda}B_{\xi\bar{\lambda}}\,r\,\mathrm{d}\theta\,\mathrm{d}r\Big)^{\frac{1}{2}}. \tag{6.8}$$

Equations (6.3)–(6.5) and (6.6)–(6.8) are related by:

$$\mathrm{srms}\mathbf{B}(\xi) = \sqrt{(\mathrm{srmsB}_r(\xi))^2 + (\mathrm{srmsB}_\theta(\xi))^2 + (\mathrm{srmsB}_\phi(\xi))^2}. \tag{6.9}$$

This test is an extension of DJ's test, in which $\mathrm{srms}\mathbf{B}(r)$ was used to indicate convergence (DJ's Brms). We normalized SRMS quantities such that

$$\max_\xi \mathrm{srms}\mathbf{B}(\xi) = 1. \tag{6.10}$$

The SRMS tests involve the amplification factors $n(n+1)$, $\partial S/\partial r$, $\partial Y/\partial\theta$ and $\partial Y/\partial\phi$. Thus, we expect that this test is more sensitive than the (S,T) test. Furthermore, each SRMS graph indicates the structure of the magnetic field in an average sense. The graphs, however, do not reflect any large but localized field values which do not significantly contribute to the average.

6.2.2 The Numerical Integrations

Here, we explain the numerical methods that are used in calculating the integrals in the SRMS formula. For each λ,

$$\mathbf{B}_\lambda \;= \mathbf{S}_\lambda + \mathbf{T}_\lambda \tag{6.11}$$

where, in our formalism,

$$\mathbf{S}_\lambda = \sum_{n,m} \Big(\frac{n(n+1)}{r} S^m_{n\lambda} Y^m_n, \frac{1}{r}\big(rS^m_{n\lambda}\big)' \frac{\partial Y^m_n}{\partial \theta}, \frac{1}{r\sin\theta}\big(rS^m_{n\lambda}\big)' \frac{\partial Y^m_n}{\partial \phi} \Big),$$
$$\mathbf{T}_\lambda = \sum_{n,m} \Big(0, \frac{T^m_{n\lambda}}{\sin\theta} \frac{\partial Y^m_n}{\partial \phi}, -T^m_{n\lambda} \frac{\partial Y^m_n}{\partial \theta} \Big).$$

Therefore,

$$B_{r\lambda}B_{r\overline{\lambda}} = \sum_{n_1,m_1} \sum_{n_2,m_2} \left(\frac{n_1(n_1+1)}{r} S_{n_1\lambda} Y^{m_1}_{n_1} \frac{n_2(n_2+1)}{r} S_{n_2\overline{\lambda}} Y^{m_2}_{n_2} \right)$$
$$B_{\theta\lambda}B_{\theta\overline{\lambda}} = \sum_{n_1,m_1} \sum_{n_2,m_2} \left(\frac{1}{r}(rS_{n_1\lambda})' \frac{\partial Y^{m_1}_{n_1}}{\partial \theta} \frac{1}{r}(rS_{n_2\overline{\lambda}})' \frac{\partial Y^{m_2}_{n_2}}{\partial \theta} + \frac{T_{n_1\lambda}}{\sin\theta} \frac{\partial Y^{m_1}_{n_1}}{\partial \phi} \frac{T_{n_2\overline{\lambda}}}{\sin\theta} \frac{\partial Y^{m_2}_{n_2}}{\partial \phi} \right.$$
$$\left. + 2\Re\Big\{ \frac{1}{r}(rS_{n_1\lambda})' \frac{\partial Y^{m_1}_{n_1}}{\partial \theta} \frac{T_{n_2\overline{\lambda}}}{\sin\theta} \frac{\partial Y^{m_2}_{n_2}}{\partial \phi} \Big\} \right)$$
$$B_{\phi\lambda}B_{\phi\overline{\lambda}} = \sum_{n_1,m_1} \sum_{n_2,m_2} \left(\frac{1}{r\sin\theta}(rS_{n_1\lambda})' \frac{\partial Y^{m_1}_{n_1}}{\partial \phi} \frac{1}{r\sin\theta}(rS_{n_2\overline{\lambda}})' \frac{\partial Y^{m_2}_{n_2}}{\partial \phi} + T_{n_1\lambda} \frac{\partial Y^{m_1}_{n_1}}{\partial \theta} T_{n_2\overline{\lambda}} \frac{\partial Y^{m_2}_{n_2}}{\partial \theta} \right.$$
$$\left. - 2\Re\Big\{ \frac{1}{r\sin\theta}(rS_{n_1\lambda})' \frac{\partial Y^{m_1}_{n_1}}{\partial \phi} T_{n_2\overline{\lambda}} \frac{\partial Y^{m_2}_{n_2}}{\partial \theta} \Big\} \right).$$

Substituting the above equations into equations (6.6)–(6.8), led us to evaluate three types of integral: r, θ, and ϕ integrals. However, for the surface integrals in (6.3) and (6.6), the calculations are shortened by the use of orthogonality.

r Integrals

There are four different integrals

$$I_{r_1} = \int_0^1 \frac{1}{r^2} S_{n_1\lambda}\, S_{n_2\overline{\lambda}}\, \mathrm{d}r$$
$$I_{r_2} = \int_0^1 T_{n_1\lambda}\, T_{n_2\overline{\lambda}}\, \mathrm{d}r$$
$$I_{r_3} = \int_0^1 \frac{1}{r^2}(rS_{n_1\lambda})'\,(rS_{n_2\overline{\lambda}})'\, \mathrm{d}r$$
$$I_{r_4} = \int_0^1 \frac{1}{r}(rS_{n_1\lambda})'\, T_{n_2\overline{\lambda}}\, \mathrm{d}r$$

We approximate these integrals using Simpson's rule. This rule is adequate, having error $\mathcal{O}(h^4)$ compared to the error $\mathcal{O}(h^2)$ of our second order central difference scheme (2.35) and (2.36) on page 20.

θ Integrals

There are five integrals

$$I_{\theta_1} = \int_0^\pi P_{n_1}^{m_1}(\cos\theta) P_{n_2}^{m_2}(\cos\theta)\,\mathrm{d}\theta, \tag{6.12}$$

$$I_{\theta_2} = \int_0^\pi \frac{\mathrm{d}}{\mathrm{d}\theta} P_{n_1}^{m_1}(\cos\theta) \frac{\mathrm{d}}{\mathrm{d}\theta} P_{n_2}^{m_2}(\cos\theta)\,\mathrm{d}\theta, \tag{6.13}$$

$$I_{\theta_3} = \int_0^\pi \frac{m_1 m_2}{\sin^2\theta} P_{n_1}^{m_1}(\cos\theta) P_{n_2}^{m_2}(\cos\theta)\,\mathrm{d}\theta, \tag{6.14}$$

$$I_{\theta_4} = \int_0^\pi \frac{\mathrm{d}}{\mathrm{d}\theta} P_{n_1}^{m_1}(\cos\theta) \frac{m_2}{\sin\theta} P_{n_2}^{m_2}(\cos\theta)\,\mathrm{d}\theta, \tag{6.15}$$

$$I_{\theta_5} = \int_0^\pi \frac{m_1}{\sin\theta} P_{n_1}^{m_1}(\cos\theta) \frac{\mathrm{d}}{\mathrm{d}\theta} P_{n_2}^{m_2}(\cos\theta)\,\mathrm{d}\theta, \tag{6.16}$$

As defined in (2.21) on page 18, P_n^m is the Schmidt normalized Legendre function. This normalization is commonly used in geomagnetism and geophysics (Chapman and Bartels, 1962). The alternative Neumann normalized Legendre function, $P_{n,m}$, used by BG and PAS and the default in MATLAB and *Mathematica*, is

$$P_{n,m} = \begin{cases} P_n^m & \text{, when } m = 0, \\ \left(2\frac{(n-m)!}{(n+m)!}\right) P_n^m & \text{, when } m > 0. \end{cases}$$

In calculating integrals (6.12)–(6.16), we used various numerical methods:

1. Built in Legendre Function and numerical integration in MATLAB.
2. Built in Legendre Function and integration in *Mathematica*.
3. The Gauss-Kronrod (GK) method available as a Fortran routine from the Guide to Available Mathematical Software (GAMS) web site.

We first consider integral (6.12) using both the Neumann and Schmidt normalizations to determine the numerical suitability.

In our experiment on integral (6.12), we sometimes could not obtain agreement between MATLAB, *Mathematica* and the GK method, using Neumann normalization. However, apart from a very small values, agreement was obtained using the Schmidt normalization. As a further check, we also evaluated

$$\int_{-1}^1 P_{n_1}^{m_1}(\cos\theta) P_{n_2}^{m_2}(\cos\theta)\,\mathrm{d}\cos\theta, \tag{6.17}$$

using the above methods and the formula of Schuster (1903) (see appendix), and reached the same conclusion. These results confirm the generally accepted rule that

Schmidt normalization is better for numerical work. The integration differences are explainable since the integrand of (6.12) can be highly oscillatory for some n and m, and the amplitudes with Neumann normalization can be much bigger than with Schmidt, as shown in Figure 6.1.

We conclude that it is convenient to use the Schmidt normalized Legendre function with the GK method for evaluating integral (6.12). Furthermore, using the Schmidt normalization, the recurrence relations (Chapman and Bartels, 1962):

$$\begin{aligned}\frac{\mathrm{d}}{\mathrm{d}\theta}P_n^m =& \tfrac{1}{2}\{\delta_{m-1}^0(n+m)(n-m+1)\}^{\frac{1}{2}}P_n^{m-1} \\ & - \tfrac{1}{2}\{(n+m+1)(n-m)\}^{\frac{1}{2}}P_n^{m+1}\,(m>0) \qquad (6.18)\\ \frac{\mathrm{d}}{\mathrm{d}\theta}P_n^0 =& -\{\tfrac{1}{2}n(n+1)\}^{\frac{1}{2}}P_n^1 \qquad (6.19)\\ 2\frac{m}{\sin\theta}P_n^m =& \{\delta_{m-1}^0(n+m)(n+m-1)\}^{\frac{1}{2}}P_{n-1}^{m-1} \\ & + \{(n-m)(n-m-1)\}^{\frac{1}{2}}P_{n-1}^{m+1}\,(m>0), \qquad (6.20)\end{aligned}$$

allow us to rewrite integrals (6.13)–(6.16) in terms of (6.12).

ϕ Integrals

There is just one integral

$$\begin{aligned}\int_{2\pi} e^{(m_1-m_2)\mathrm{i}\phi}\,\mathrm{d}\phi &= 0, \text{ for } m_1-m_2\neq 0 \\ &= 2\pi, \text{ for } m_1-m_2=0. \qquad (6.21)\end{aligned}$$

(a)

(b)

(c)

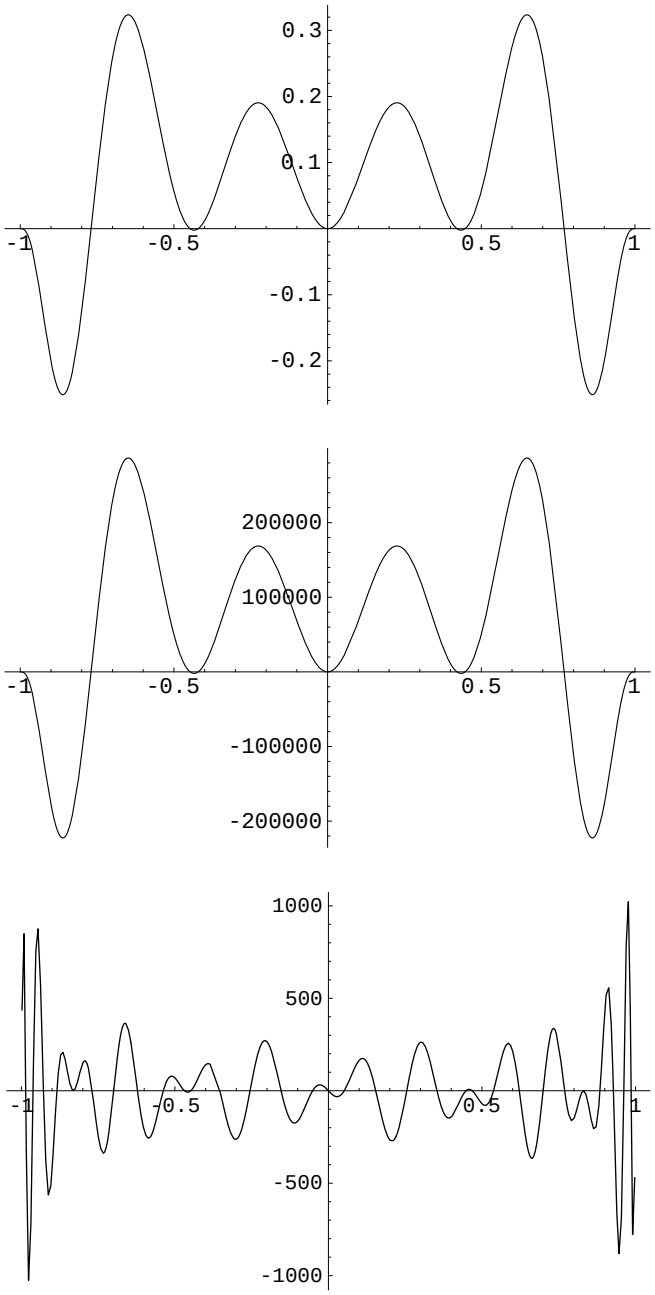

Figure 6.1: Plot of (a) $P_8^5 P_7^2$ using Schmidt normalization, (b)$P_8^5 P_7^2$ using Neumann normalization, and (c)$P_{30}^2 P_6^1$ using Neumann normalization.

6.2.3 Visual and Numerical Presentation for SRMS

For visual presentation, we need only twelve graphs for $\mathrm{srmsB}(\xi), \mathrm{srmsB}_\xi(\xi)$. To observe convergence, in each graph, we plot a SRMS quantity for two different $[J, N]$ values.

For numerical presentation, we calculate the maximum absolute difference (MAD)

$$\mathrm{MAD}(\mathrm{srmsX}) := \max_\xi |\,\mathrm{srmsX}(\xi, J_2, N_2) - \mathrm{srmsX}(\xi, J_1, N_1)|,$$

the maximum mixed difference (MMD)

$$\mathrm{MMD}(\mathrm{srmsX}) := \max_\xi \frac{|\,\mathrm{srmsX}(\xi, J_2, N_2) - \mathrm{srmsX}(\xi, J_1, N_1)|}{1 + |\,\mathrm{srmsX}(\xi, J_2, N_2)|},$$

and the maximum relative difference (MRD)

$$\mathrm{MRD}(\mathrm{srmsX}) := \max_\xi \frac{|\,\mathrm{srmsX}(\xi, J_2, N_2) - \mathrm{srmsX}(\xi, J_1, N_1)|}{|\,\mathrm{srmsX}(\xi, J_2, N_2)|}.$$

where $X = \mathbf{B}$, B_ξ and $\max_\xi \mathrm{srms}\mathbf{B}(\xi) = 1$.

6.3 The Volume Root Mean Square (VRMS) Test

In their earlier work, PAS used the magnetic energy

$$E = \frac{1}{2\mu} \int_V |\mathbf{B}|^2 \,\mathrm{d}V, \tag{6.22}$$

where μ is the permeability, to test convergence. PAS maintained that this test is more stringent than the λ test. In this chapter, we construct a volume root-mean-square (VRMS) test which is similar to SRMS and has the same sensitivity as E:

$$\begin{aligned}
\mathrm{vrms}\mathbf{B} :&= \left[\frac{3\mu E}{2\pi}\right]^{1/2}, \\
&= \left[\frac{3}{4\pi} \int_V |\mathbf{B}|^2 \,\mathrm{d}V\right]^{1/2}, \\
&= \Big[\sum_{n,m} 3n(n+1) \int_0^1 \Big(n(n+1)|S_n^m|^2 \\
&\qquad + \left|\frac{\mathrm{d}}{\mathrm{d}r}(rS_n^m)\right|^2 + |rT_n^m|^2\Big) \,\mathrm{d}r\Big].
\end{aligned} \tag{6.23}$$

We expect that VRMS is less sensitive than SRMS because the volume integral decreases sensitivity. There is no natural way of normalizing $\mathrm{vrms}\mathbf{B}$. If we normalize

vrms$\mathbf{B}$ using a sensitive factor, such as $\mathbf{B}$, then it become artificially sensitive. We decided to calculate vrms$\mathbf{B}$ directly from the (S,T) eigenvector, in which case it has normalization as in the (S,T) test.

For numerical presentation, we calculate the absolute difference (AD)

$$\mathrm{AD}(\mathrm{vrms}\mathbf{B}) := |\,\mathrm{vrms}\mathbf{B}(J_1,N_1) - \mathrm{vrms}\mathbf{B}(J_2,N_2)|,$$

the mixed difference (MD)

$$\mathrm{MD}(\mathrm{vrms}\mathbf{B}) := \frac{\mathrm{AD}(\mathrm{vrms}\mathbf{B})}{1+|\,\mathrm{vrms}\mathbf{B}(J_2,N_2)|},$$

and the relative difference (RD)

$$\mathrm{RD}(\mathrm{vrms}\mathbf{B}) := \mathrm{AD}(\mathrm{vrms}\mathbf{B})/|\,\mathrm{vrms}\mathbf{B}(J_2,N_2)|,$$

so that we can compare it with the other tests.

6.4 Comparison of Convergence Tests

To determine the most sensitive and convenient test, we apply the above tests to the following models: (a) PAS as defined in (3.29) , (b) KR as defined in (3.22), (c) DJ, (d) α^2-dynamo (Roberts, 1972), and (e) free decay. In general, to calculate MAD, MMD and MRD, we use the grid $r = j/J_1, (j = 0, ..., J_1), \theta = \pi k/100, \phi = 2\pi k/100, (k = 0, ..., 100)$. The following is the DJ model,

$$\mathbf{v} = \mathbf{t}_2^0 + \epsilon \mathbf{s}_2^0, \tag{6.24}$$

where

$$t_2^0 = s_2^0 = r\sin(\pi r)\ , \epsilon = 0.14\ ,$$

with magnetic chain: $S_1^1, T_1^1, S_2^1, T_2^1, S_3^1, T_3^1, ...$

In the α^2-dynamo, the dimensionless induction equations are

$$\frac{\partial S}{\partial t} = R_\alpha T + \nabla^2 S, \tag{6.25}$$

$$\frac{\partial T}{\partial t} = -R_\alpha \nabla^2 S + \nabla^2 T, \tag{6.26}$$

where R_α is a mean-field magnetic Reynolds number and $R_{\mathrm{crit}} \approx 4.49$, with magnetic chain: S_1^0, T_1^0.

We originally intended to use (M)RD to compare all tests. However, this was not possible due to the very large errors as discussed previously in §6.1.2. As a result, we used (M)RD for comparing the λ, SRMS and VRMS tests. And we used (M)AD and (M)MD for comparing the $\mathbf{B}$, (S,T), SRMS and VRMS tests.

6.4.1 The Free Decay Model

In this problem, it can be proved theoretically that the change in λ is second order in the change of the (S,T) eigenvector. Suppose

$$\eta\nabla^2 f = \begin{cases} \lambda f & \text{in } V; \\ 0 & \text{in } \widehat{V}; \end{cases} \tag{6.27}$$

$$\nabla f = \mathcal{O}(1/r^2) \qquad \text{as } r \to \infty; \tag{6.28}$$

$$[g\nabla f] = 0 \qquad \text{across } \Sigma; \tag{6.29}$$

$$g = \mathcal{O}(1/r) \qquad \text{as } r \to \infty. \tag{6.30}$$

Our magnetic scalars (S,T) actually satisfy $\nabla f = \mathcal{O}(1/r^3)$, $g = \mathcal{O}(1/r^2)$ as $r \to \infty$. The valid choices for (f,g) are: $(S,S),(T,T),(T,S)$, but not (S,T) since (6.29) is invalid. Using (6.27)–(6.30), we consider the following integral:

$$\begin{aligned} \lambda \int_V fg \,\mathrm{d}V &= \eta \int_V \nabla^2 f \cdot g \,\mathrm{d}V, \\ &= -\eta \int_{\widehat{V}} \nabla\cdot(g\nabla f)\,\mathrm{d}V + \eta \int_{\Sigma_\infty} g\nabla f \cdot \mathbf{e}_r \,\mathrm{d}\Sigma \\ &\quad - \eta \int_V \nabla f \cdot \nabla g \,\mathrm{d}V, \\ &= -\eta \int_{V_\infty} \nabla f \cdot \nabla g \,\mathrm{d}V - \eta \int_{\widehat{V}} g\nabla^2 f \,\mathrm{d}V \\ &\quad + \eta \int_{\Sigma_\infty} \mathcal{O}(1/r^3) r^2 \,\mathrm{d}\Sigma\,, \\ &= -\eta \int_{V_\infty} \nabla f \cdot \nabla g \,\mathrm{d}V\,. \end{aligned} \tag{6.31}$$

The special choices $g = f, g = \delta f$ yield

$$\lambda \int_V f^2 \,\mathrm{d}V = -\eta \int_{V_\infty} (\nabla f)^2 \,\mathrm{d}V\,, \tag{6.32}$$

$$\lambda \int_V f(\delta f)\,\mathrm{d}V = -\eta \int_{V_\infty} \nabla f \cdot \nabla(\delta f)\,\mathrm{d}V\,. \tag{6.33}$$

Varying (6.32),

$$(\lambda + \delta\lambda) \int_V (f+\delta f)^2 \,\mathrm{d}V = -\eta \int_{V_\infty} \big(\nabla f + \nabla(\delta f)\big)^2 \,\mathrm{d}V\,. \tag{6.34}$$

Using (6.32) and (6.33),

$$\lambda \int_V (\delta f)^2 \,\mathrm{d}V + \delta\lambda \int_V (f+\delta f)^2 \,\mathrm{d}V = -\eta \int_{V_\infty} \big(\nabla(\delta f)\big)^2 \,\mathrm{d}V\,. \tag{6.35}$$

On the right hand side of (6.35), if $f = T$, then V_∞ can be replaced with V since $T = \delta T = 0$ in $\widehat{V}$. Equation (6.35) implies that $\delta\lambda$ is second order in (δf) and $\nabla(\delta f)$, where $f = S, T$. Our numerical results, as presented in Table 6.1, reveal MAD$((S,T)) \approx$ MAD$(SRMS)$, MMD$((S,T))\approx$MMD(SRMS) and RD$(\lambda) \lll$ MRD(SRMS). These results confirm that (S,T) is more sensitive than λ for free decay. In the steady kinematic dynamo problem, where the eigenvalue is R, a similar result to (6.35) has been discussed by Gibson and Roberts (1967).

	J	N	λ	SRMS	**B**	ST	VRMS
	10	1	-9.8805767				2.4936311
	20	1	-9.8723019				2.5025770
(M)AD				0.0096578	0.0110236	0.0057261	0.0089459
(M)MD				0.0053984	0.0059406	0.0035758	0.0025541
(M)RD			0.000838	0.0434350			0.0035746

Table 6.1: Comparison of λ, SRMS, **B**, ST and VRMS for the free decay problem using $J = 10, 20$ and $N = 1$.

6.4.2 PAS, KR, DJ and α^2-Dynamo Models

Here, we compare convergence tests. The comparison of convergence tests is divided into two groups. In the first group, we use the same R as earlier researchers (i.e. PAS, KR, and DJ), given in Tables 5, 6 and Figure 8 of DJ. In the second group, we use R_+ such that $\lambda_{\max}(R_+) \approx 1$. With the chosen R, generally we aim for 1% and 5% changes in $\lambda_{\max}$ but this is not always obtainable.

All of the differences have magnitude $\mathcal{O}(h^2)$ due to the $\mathcal{O}(h^2)$ accuracy of the eigenvalue and eigenvector. Consequently, the estimates of the differences depend on the numerical methods used. For example, we found that the MAD of SRMS, **B** and (S,T) depended on the type of interpolation used (e.g. linear or spline) in their calculation. To remove this dependence, we chose J_1 to be a divisor of J_2, and used J_1 radial subintervals, so that no interpolation was needed.

We rank the tests using the following rules: (a) Ranks 1–5 were given, where 1 is the most sensitive, and (b) two tests will be given the same rank if they agree to within 0.5 in the leading digit. The numerical results can be seen in Tables 6.2–6.8. In addition, the comparative rankings are shown in Tables 6.9–6.11.

In (M)AD rankings, we found the **B** test to be the most sensitive in the majority of cases followed by SRMS, (S,T) and VRMS. However, there are some exceptional cases. In Tables 6.4b, 6.8a and 6.8b, SRMS is as sensitive as **B**. In Table 6.7b, (S,T) is as sensitive as SRMS and more sensitive than SRMS in Table 6.6b. VRMS is the least sensitive test in all cases, except in Table 6.8a where (S,T) is the least sensitive one.

In (M)MD rankings, we found that the rank order is similar to that in (M)AD. We also found some exceptional cases, as in the (M)AD rankings. In Tables 6.4b, 6.5b, 6.8a and 6.8b, SRMS is as sensitive as **B**. In Table 6.6a and b, (S,T) seems to be as sensitive as SRMS. VRMS is the least sensitive test in almost all cases, except in Table 6.8a, where (S,T) is least sensitive.

In (M)RD rankings, VRMS is still the least sensitive test in all cases. We reach no conclusion on the most sensitive test. 50% of our results show that λ is more sensitive than SRMS but the other 50% show vice versa.

In the second group except for VRMS, we used (M)AD to compare the tests. This seems reasonable for **B**, (S,T) and SRMS, given the normalization specified in §6.1.2, §6.1.3, and §6.2. This also seems reasonable for λ since $\lambda_{\max}(R) \approx 1$ and hence AD $\approx$ RD, this choice of R in effect normalizes $\lambda_{\max}$. However, lacking any obvious way of normalizing VRMS, we used RD to compare it with the other tests. The differences and comparative rankings are shown in Table 6.12. In determining their rank, we use the same rules as used above for the first group.

Similar to the first group, we are unable to draw any general conclusion regarding to the most sensitive test. However, our results show that λ is often more sensitive than the (S,T) eigenvector, and sometimes even more sensitive than **B**. Moreover, either λ or **B** is always the most sensitive test. Meanwhile, SRMS is usually more sensitive than (S,T) and VRMS. VRMS seems to be the least sensitive test in all cases, except when we compare two truncation levels, $([J_1, N_1] = [100, 15], [J_2, N_2] = [200, 15])$, of the DJ model.

Our results, in the PAS, KR, DJ and α^2 models tested, reveal that $\lambda_{\max}$ is usually a more sensitive measure of convergence than (S,T) eigenvector. This is contrary to expectations and common belief. Gubbins (1972) argued that the magnitude of the higher harmonics in X are more sensitive than $\lambda_{\max}$ with respect to changing N and keeping J fixed. However, his argument only applies when the matrix in (2.38) is sparse but not banded.

		J	N	$\lambda_{\max}$	SRMS	$\mathbf{B}$	(S,T)	VRMS
a		100	15	2.0398095				0.5391634
		100	16	2.0276901				0.5393975
	(M)AD				0.0010093	0.0138683	0.0004388	0.0002341
	(M)MD				0.0008689	0.0116743	0.0003377	0.0001520
	(M)RD			0.0059769	0.0062496			0.0004340
b		50	11	2.3097980				0.5363805
		100	11	2.3140750				0.5346440
	(M)AD				0.0078823	0.0083763	0.005726	0.0017365
	(M)MD				0.0044972	0.0069540	0.0034252	0.0011315
	(M)RD			0.0513505	0.0512122			0.0032479

Table 6.2: Comparison of λ, SRMS, $\mathbf{B}$, (S,T) and VRMS for PAS. The changes in $\lambda_{\max}$ are less than 1%. We vary N in (a) and J in (b).

		J	N	$\lambda_{\max}$	SRMS	$\mathbf{B}$	(S,T)	$VRMS$
a		100	13	1.9246983				0.5410935
		100	14	1.9729995				0.5402251
	(M)AD				0.0020500	0.0281684	0.0016901	0.0008683
	(M)MD				0.0017677	0.0240300	0.0009737	0.0005638
	(M)RD			0.0244811	0.0190023			0.0016073
b		50	9	1.0148861				0.5574653
		100	9	1.0501654				0.5561781
	(M)AD				0.0069606	0.0102706	0.0044087	0.0012871
	(M)MD				0.0039658	0.0069611	0.0034251	0.0008271
	(M)RD			0.0335938	0.0383175			0.0023142

Table 6.3: Comparison of λ, SRMS, $\mathbf{B}$, (S,T) and VRMS for PAS. The changes in $\lambda_{\max}$ are less than 5%. We vary N in (a) and J in (b).

		J	N	$\lambda_{\max}$	SRMS	$\mathbf{B}$	(S,T)	VRMS
a		800	11	0.1908203				1.1766875
		800	12	0.1921644				1.1768992
	(M)AD				0.0250262	0.0341076	0.0010932	0.0002117
	(M)MD				0.0171473	0.0251564	0.0010796	0.0000973
	(M)RD			0.0069948	0.1053402			0.0001799
b		800	12	0.1921644				1.1768992
		1600	12	0.1910535				1.1769060
	(M)AD				0.0001232	0.0001369	0.0000516	0.0000068
	(M)MD				0.0001056	0.0001155	0.0000431	0.0000031
	(M)RD			0.0058146	0.0022149			0.0000058

Table 6.4: Comparison of λ, SRMS, $\mathbf{B}$, (S,T) and VRMS for KR. The changes in $\lambda_{\max}$ are less than 1%. We vary N in (a) and J in (b).

		J	N	$\lambda_{\max}$	SRMS	$\mathbf{B}$	(S,T)	VRMS
a		100	9	0.2830387				1.1763992
		100	10	0.2864833				1.1756805
	(M)AD				0.0432499	0.0740190	0.0040132	0.0007188
	(M)MD				0.0286046	0.0536863	0.0039638	0.0003304
	(M)RD			0.0120235	0.1160508			0.0006114
b		400	10	0.1967945				1.1770135
		800	10	0.1923502				1.1770804
	(M)AD				0.0004955	0.0005556	0.0002020	0.0000669
	(M)MD				0.0004245	0.0004691	0.0001773	0.0000307
	(M)RD			0.0231053	0.0082287			0.0000568

Table 6.5: Comparison of λ, SRMS, $\mathbf{B}$, (S,T) and VRMS for KR. The changes in $\lambda_{\max}$ are less than 5%. We vary N in (a) and J in (b).

		J	N	$\lambda_{\max}$	SRMS	$\mathbf{B}$	(S,T)	VRMS
a		100	9	1.4510494				0.9801350
		100	10	1.4614627				0.9808524
	(M)AD				0.0047974	0.0625658	0.0036968	0.0007175
	(M)MD				0.0033303	0.0606694	0.0030416	0.0003623
	(M)RD			0.0071253	0.0064795			0.0007315
b		50	9	1.4607313				0.9803844
		100	9	1.4510494				0.9801350
	(M)AD				0.0014877	0.0033139	0.0025158	0.0002495
	(M)MD				0.0011018	0.0023958	0.0012595	0.0001260
	(M)RD			0.0066723	0.0027058			0.0002545

Table 6.6: Comparison of λ, SRMS, $\mathbf{B}$, (S,T) and VRMS for DJ. The changes in $\lambda_{\max}$ are less than 1%. We vary N in (a) and J in (b).

		J	N	$\lambda_{\max}$	SRMS	$\mathbf{B}$	(S,T)	VRMS
a		100	6	1.5510714				0.9840762
		100	10	1.4614627				0.9808524
	(M)AD				0.0568522	0.1891378	0.0234026	0.0032237
	(M)MD				0.0349397	0.1821002	0.0227682	0.0016248
	(M)RD			0.0613144	0.0908874			0.0032867
b		20	9	1.5767503				0.9754851
		100	9	1.4510494				0.9801350
	(M)AD				0.0101338	0.0252767	0.0109626	0.0046499
	(M)MD				0.0068365	0.0172203	0.0059534	0.0023538
	(M)RD			0.0866276	0.0196633			0.0047441

Table 6.7: Comparison of λ, SRMS, $\mathbf{B}$, (S,T) and VRMS for DJ. The changes in $\lambda_{\max}$ are less than 5%. We vary N in (a) and J in (b).

		J	N	$\lambda_{\max}$	SRMS	$\mathbf{B}$	(S,T)	VRMS
a		15	1	0.7383134				0.9311456
		90	1	0.7031502				0.9369293
	(M)AD				0.0125802	0.0125100	0.0030344	0.0057837
	(M)MD				0.0069817	0.0068032	0.0021006	0.0029860
	(M)RD			0.0500080	0.3458718			0.0061731
b		30	1	0.7111874				0.9363679
		90	1	0.7031502				0.9369293
	(M)AD				0.0034270	0.0034386	0.0006458	0.0005614
	(M)MD				0.0018758	0.0018481	0.0004662	0.0002899
	(M)RD			0.0114302	0.0728596			0.0005992

Table 6.8: Comparison of λ, SRMS, $\mathbf{B}$, (S,T) and VRMS for α^2 dynamo. The changes in $\lambda_{\max}$ are less than 1% in (a) and 5% in (b).

Table														
	6.2a	6.2b	6.3a	6.3b	6.4a	6.4b	6.5a	6.5b	6.6a	6.6b	6.7a	6.7b	6.8a	6.8b
SRMS	2	2	2	2	2	1	2	2	2	3	2	2	1	1
$\mathbf{B}$	1	1	1	1	1	1	1	1	1	1	1	1	1	1
(S,T)	3	3	3	3	3	3	3	3	3	2	3	2	4	3
VRMS	4	4	4	4	4	4	4	4	4	4	4	4	3	4

Table 6.9: (M)AD rankings of SRMS, $\mathbf{B}$, (S,T) and VRMS tests using models PAS, KR, DJ and α^2.

Table														
	6.2a	6.2b	6.3a	6.3b	6.4a	6.4b	6.5a	6.5b	6.6a	6.6b	6.7a	6.7b	6.8*a*	6.8b
SRMS	2	2	2	2	2	1	2	1	2	2	2	2	1	1
$\mathbf{B}$	1	1	1	1	1	1	1	1	1	1	1	1	1	1
(S,T)	3	3	3	3	3	3	3	3	2	2	3	3	4	3
VRMS	4	4	4	4	4	4	4	4	4	4	4	4	3	4

Table 6.10: (M)MD rankings of SRMS, $\mathbf{B}$, (S,T) and VRMS tests using models PAS, KR, DJ and α^2.

Table														
	6.2a	6.2b	6.3a	6.3b	6.4a	6.4b	6.5a	6.5b	6.6a	6.6b	6.7a	6.7b	6.8	6.8b
SRMS	1	1	1	1	1	2	1	2	2	2	1	2	1	1
VRMS	3	3	3	3	3	3	3	3	3	3	3	3	3	3
λ	1	1	1	1	2	1	2	1	1	1	2	1	2	2

Table 6.11: (M)RD rankings of λ, SRMS and VRMS tests using models PAS, KR, DJ and α^2.

$[J_1, N_1]$	$\lambda_{\max}$	AD(λ)	AD($\mathbf{B}$)	AD(ST)	AD(SRMS)	RD(vrms$\mathbf{B}$)
α^2: $R_+ = 4.786$, $\lambda_{\max} = 1.0001443$ for $[J_2, N_2] = [200, 1]$						
$[40, 1]$	1.005095	0.004951	0.002321	0.000538	0.002308	0.000039
		1	2	4	2	5
$[20, 1]$	1.020566	0.020422	0.008017	0.001502	0.007983	0.001233
		1	2	4	2	4
$[10, 1]$	1.082441	0.082296	0.026389	0.009813	0.025933	0.001664
		1	2	4	2	5
PAS: $R_+ = 0.38272$, $\lambda_{\max} = 1.000245$ for $[J_2, N_2] = [200, 20]$						
$[200, 15]$	1.017098	0.016853	0.014666	0.000559	0.001461	0.000564
		1	1	4	3	5
$[200, 13]$	0.930966	0.069279	0.032761	0.002291	0.003470	0.002235
		1	2	4	3	4
$[100, 20]$	0.994794	0.005451	0.001692	0.000812	0.002063	0.000521
		1	2	4	2	5
$[50, 20]$	0.977180	0.023065	0.008376	0.004329	0.008871	0.001728
		1	2	4	2	5
KR: $R_+ = 4421$, $\lambda_{\max} = 1.000215$ for $[J_2, N_2] = [900, 12]$						
$[900, 11]$	0.997686	0.002530	0.051397	0.002250	0.037393	0.000300
		3	1	3	2	5
$[900, 7]$	0.931474	0.068742	0.251715	0.035478	0.184483	0.007109
		3	1	4	2	5
$[300, 12]$	1.011288	0.011072	0.001370	0.000502	0.001210	0.000088
		1	2	4	2	5
$[150, 12]$	1.048831	0.048615	0.006020	0.002153	0.005289	0.000491
		1	2	4	3	5
DJs2t2: $R_+ = 57.963$, $\lambda_{\max} = 1.000787$ for $[J_2, N_2] = [200, 15]$						
$[100, 15]$	1.003094	0.002307	0.000789	0.000348	0.000477	0.000411
		1	2	5	3	4
$[200, 9]$	0.994274	0.006513	0.100818	0.004081	0.038555	0.000498
		3	1	4	2	5
$[200, 8]$	1.042718	0.041931	0.155070	0.009068	0.080278	0.000169
		3	1	4	2	5
$[50, 15]$	1.012371	0.011584	0.003994	0.001598	0.001844	0.001629
		1	2	3	3	3

Table 6.12: Difference results, and rankings, for α^2, PAS, KR, DJ, at various $[J, N]$, keeping J fixed and varying N, and vice versa.

6.4.3 The Visual Convergence Test

In this section, we will consider convergence tests based on graphical presentation of the **B**, (S,T) and SRMS tests. To test convergence of the eigenvector visually, we apply SRMS, (S,T), and **B** tests to the PAS model, using $[J,N]=[100,13],[100,14]$ and magnetic chain M12 at $R=0.4$. The graph of the SRMS quantities can be seen in Figure 6.2. In addition, the (S,T) plots and the contours of **B**'s components can be seen in Figures 6.3 and 6.4, respectively. The good convergence of PAS is reflected by the fact that Figures 6.2–6.4 for the two $[J,N]$ are virtually indistinguishable.

For SRMS, we only need 12 graphs to see the distribution of SRMS fields. On the other hand, with the above $[J,N]$, $\mathcal{O}(N^2)$ (i.e. about 150) graphs may be needed for the (S,T) test. Figure 6.3 shows some of the $S_n^m(r), T_n^m(r)$ plots. We observe that there are already 25 plots where $N \leq 5$. Moreover, $S_n^m(r), T_n^m(r)$ plots give little or no information about the spatial structure of **B** (which involve sums of product and derivative of (S_n^m, T_n^m) and spherical harmonics). For the **B** test, the graphs give information about the spatial variation of **B** as shown in Figure 6.4. But, we need to plot the contour of **B**'s components in many meridional and equatorial planes to observe global convergence visually. For visual presentation, we conclude that SRMS graphs are the most convenient to use.

For the λ test, we visually observe the convergence of PAS by using $\lambda_{\max}(R)$, $\lambda_{\max}(N)$ and $\lambda_{\max}(h^2)$ plots. These plots are given in Figure 6.5 on page 107. Again, the good convergence of PAS is reflected in these plots. $\lambda_{\max}(R)$ plots show the convergence of $\lambda_{\max}$ and also R_{crit}. $\lambda_{\max}(N)$ and $\lambda_{\max}(h^2)$ plots show the convergence of $\lambda_{\max}$ with respect to J and N.

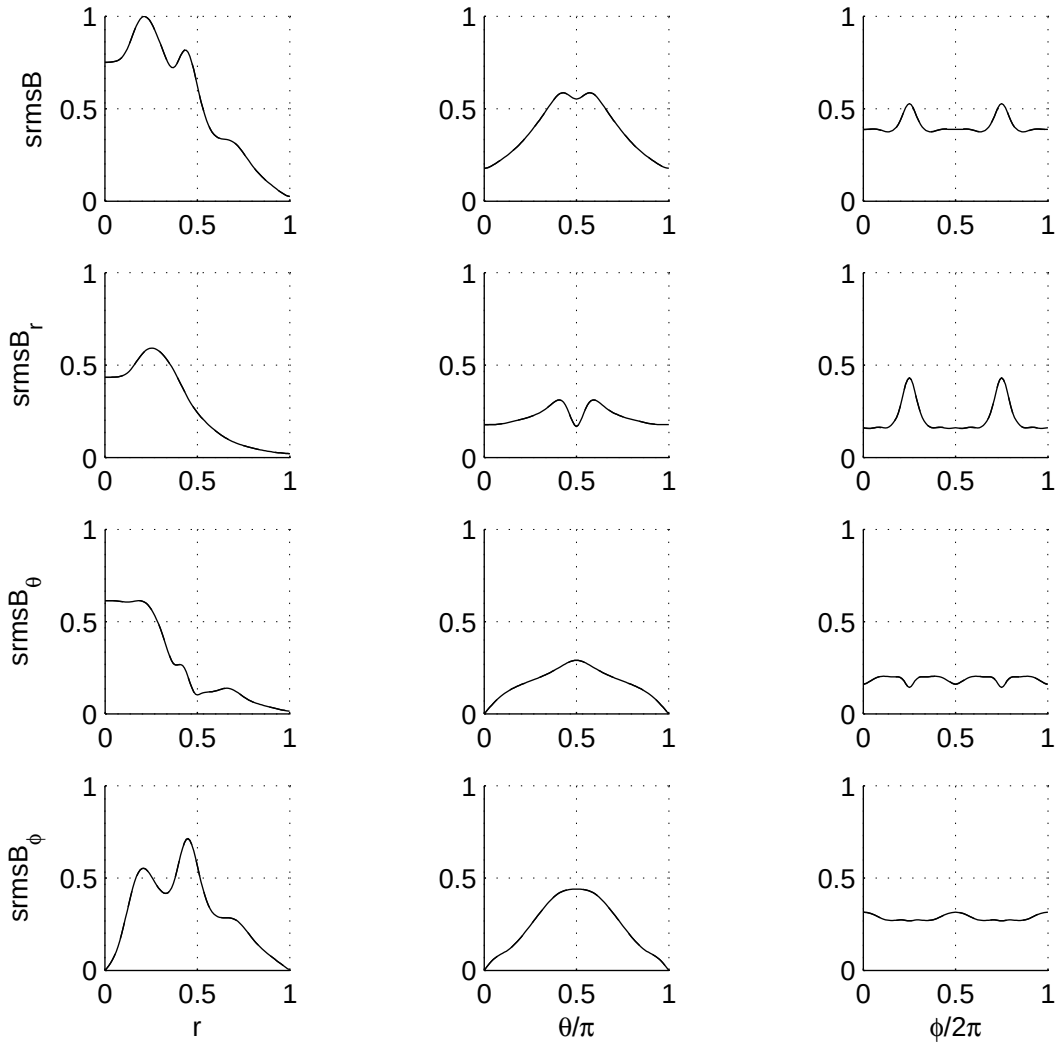

Figure 6.2: SRMS quantities for model PAS at $R = 0.4$ using $[J, N] = [100, 13]$ and $[J, N] = [100, 14]$ represented by solid and dashed line respectively. The difference between the two $[J, N]$ curves is indistinguishable in each case.

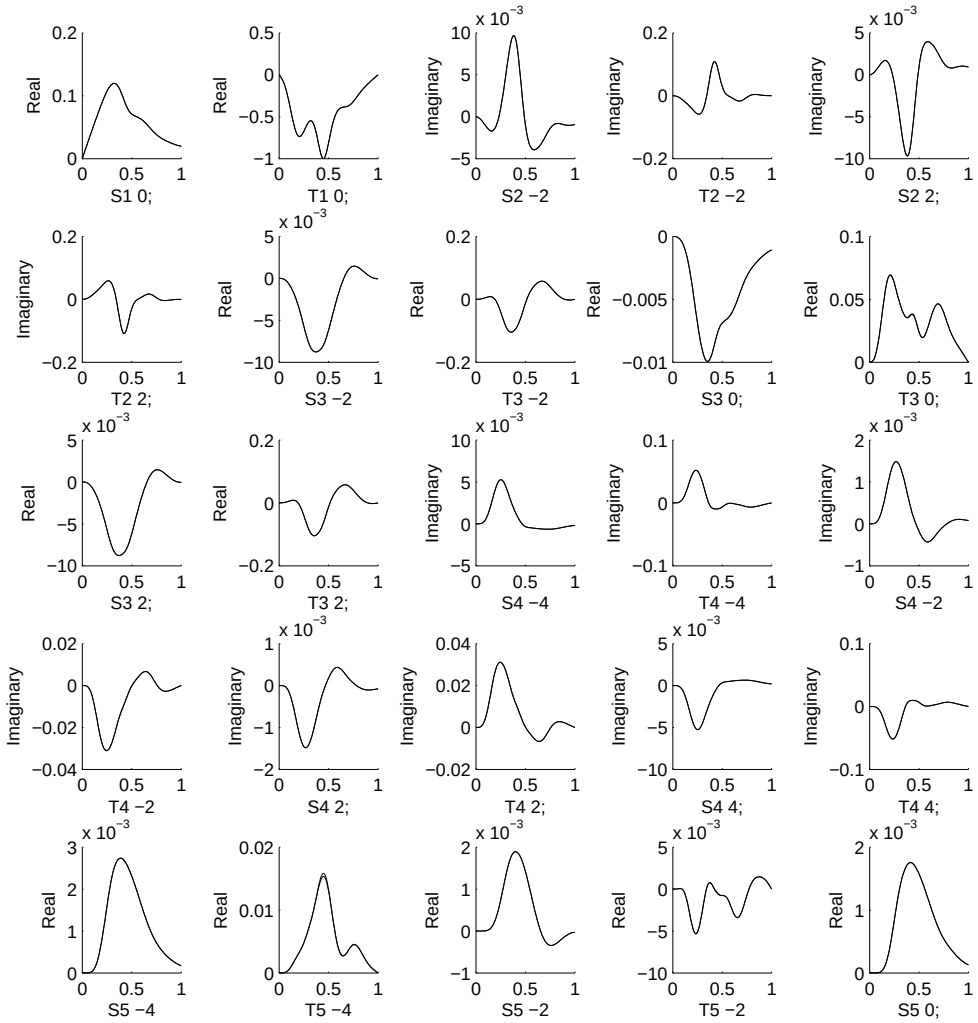

Figure 6.3: A selection of $(S_n^m(r), T_n^m(r))$ plots for model PAS at $R = 0.4$ using $[J, N] = [100, 13]$ and $[J, N] = [100, 14]$. A complete $(S_n^m(r), T_n^m(r))$ plot for this model may consist of more than 50 graphs.

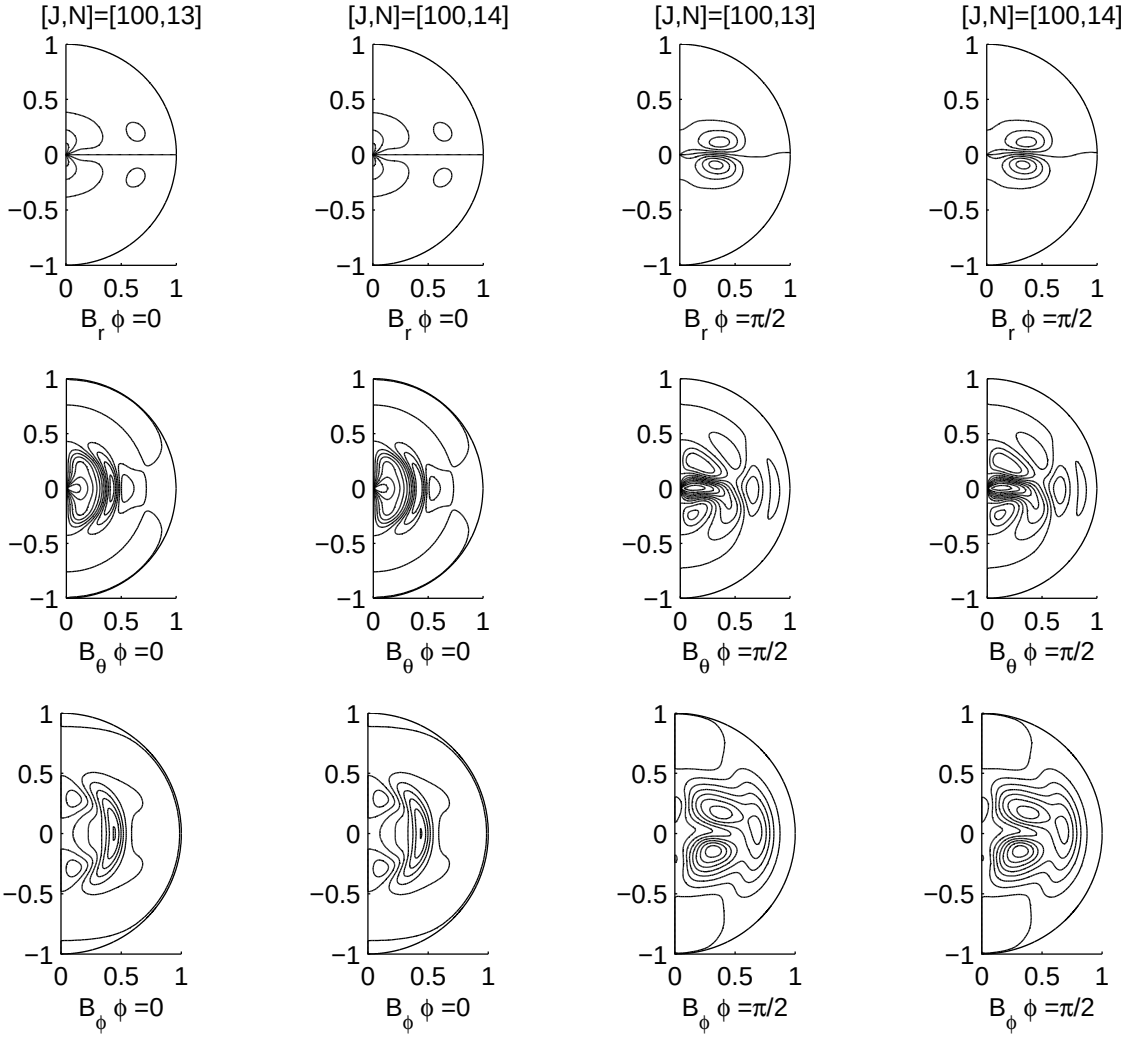

Figure 6.4: B_r, B_θ, B_ϕ contours for model PAS at $R = 0.4$, in the plane $\phi = 0$, are presented in the first column using $[J, N] = [100, 13]$ and in the second column using $[J, N] = [100, 13]$. B_r, B_θ, B_ϕ contours, in the plane $\phi = \pi/2$, are presented in the third column using $[J, N] = [100, 13]$ and in the fourth column using $[J, N] = [100, 13]$.

(a)

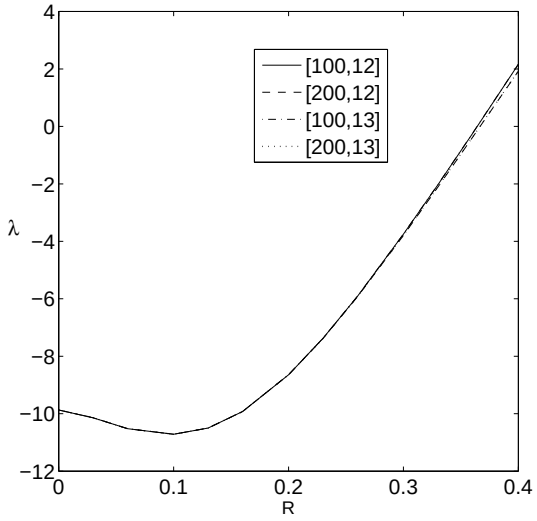

(b)

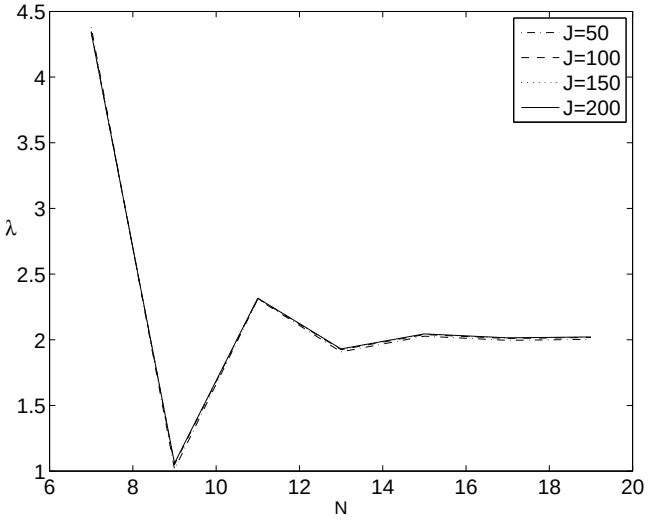

(c)

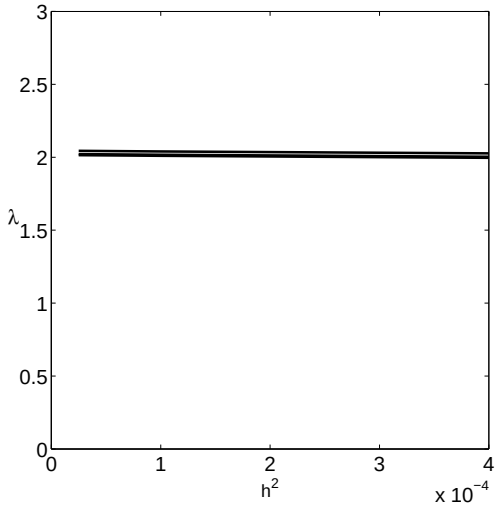

Figure 6.5: Plot of (a) $\lambda_{\max}(R)$ using $[J, N] = [100, 12], [100, 13], [200, 12], [200, 12]$; (b)$\lambda_{\max}(N)$ using $J = 50, 100, 150, 200$ at $R = 0.4$; and (c) $\lambda_{\max}(h^2)$ at $R = 0.4$ for the PAS model with magnetic chain M12.

6.5 Application to Planar Velocity Dynamos

In Chapter 3, one of the highest $[J, N]$ used, was $[2400, 35]$, which is approximately equivalent to a 39 GB matrix band size and a 70 MB eigenvector size. These size arrays are difficult to store. Here, we use less demanding $[J, N]$ to test the convergence of models p1Y22DM12 and p1q10Y22DM12, using SRMS, $\mathbf{B}$, (S, T) and VRMS tests. Nevertheless, we use $[J, N]$ that give the same level of convergence at the same supercritical R as shown in Table 3.2 on page 39 and Table 3.5 on page 46 (i.e. $\mathrm{RD}(\lambda_{\max}) \lesssim 0.1\%$ for fixed J and $\mathrm{RD}(\lambda_{\max}) \lesssim 5\%$ for fixed N).

In Chapter 3, we used the terminology "level of convergence" with reference to $\lambda_{\max}$ (we spoke of 1% convergence when $\mathrm{RD}(\lambda_{\max}) \approx 0.01$). In this section, we more generally use the wording "1% level of convergence" for any convergence tests where the associated measure [i.e. (M)AD, (M)MD, (M)RD] is $\lesssim 0.01$; similarly for 2% and so on.

To test convergence with respect to N, we chose $[J, N] = [400, 56], [400, 55]$ for p1Y22DM12 and $[J, N] = [400, 49], [400, 50]$ for p1q10Y22DM12. The results are shown in Table 6.13. For the $\mathbf{B}$ test, which is the most sensitive test (according to our results in §6.4), Table 6.13 shows that MAD($\mathbf{B}$), MMD($\mathbf{B}$) give $\lesssim 0.5\%$ level of convergence. In addition, all other tests give $\lesssim 0.2\%$ level of convergence.

To test convergence with respect to J, we chose $[J, N] = [2400, 28], [1600, 28]$ for models p1Y22DM12 and p1q10Y22DM12. The results are shown in Table 6.14. For the $\mathbf{B}$ test, Table 6.14 shows that MAD($\mathbf{B}$), MMD($\mathbf{B}$) give $\lll 1\%$ level of convergence. In addition, all other tests, except the λ test, give $\lesssim 0.5\%$ level of convergence.

To test convergence visually, it is inconvenient to show a large number of $(S_n^m(r), T_n^m(r))$ graphs (e.g for N=56, as many as 1624 graphs may be needed in general). On the other hand, it is very easy to show the 12 SRMS graphs, as in Figures 6.6–6.8. These Figures show unobservable differences between $[J, N] = [400, 55], [400, 56]$, $[J, N] = [400, 56], [2400, 28]$ and $[J, N] = [2400, 28], [1600, 28]$, and hence demonstrate convergence. In addition, these graphs give some idea of the distribution of $\mathbf{B}$ throughout the sphere, in an average sense, for models p1Y22DM12 and p1q10Y22DM12.

All $\mathrm{srmsB}_\xi(r)$ fields are concentrated near $r = 0$, and have similar magnitude; $\mathrm{srmsB}_r(\theta)$ is concentrated near the equator, $\theta = \pi/2$; $\mathrm{srmsB}_\theta(\theta)$ is stronger near the polar axis. Meanwhile, $\mathrm{srmsB}_\phi(\theta)$ is stronger near $\theta = 0, \pi/2, \pi$. In the ϕ direction, $\mathrm{srmsB}_r(\phi)$ and $\mathrm{srmsB}_\theta(\phi)$ are concentrated near $\phi = 3\pi/4, 7\pi/4$, i.e. at the cell boundaries of the planar flow (see Figure 3.1 on page 31). In contrast, $\mathrm{srmsB}_\phi(\phi)$ field is flat, except near the cell boundaries where the field is nearly zero. SRMS graphs of p1q10Y22DM12 are similar to those of p1Y22DM12, except for $\mathrm{srmsB}_\phi(r)$ which is greater for model p1q10Y22DM12 near $r = 1$.

At this point, we conclude that models p1Y22DM12 and p1q10Y22DM12 can maintain a magnetic field since all tests, except the λ test, give $< 1\%$ level of convergence.

		J	N	$\lambda_{\max}$	SRMS	$\mathbf{B}$	(S,T)	VRMS
a		400	55	0.929184				1.213290
		400	56	0.930387				1.213283
	(M)AD				0.000022	0.002371	0.000014	0.000007
	(M)MD				0.000018	0.002489	0.000013	0.000003
	(M)RD			0.001293	0.001717			0.000006
b		400	49	2.227584				2.308324
		400	50	2.227706				2.308351
	(M)AD				0.000048	0.004595	0.000024	0.000027
	(M)MD				0.000041	0.004548	0.000024	0.000008
	(M)RD			0.000055	0.001290			0.000012

Table 6.13: Comparison of λ, SRMS, $\mathbf{B}$, (S,T) and VRMS for (a) model p1Y22DM12 at $R = 220$ using $[J,N] = [400,55],[400,56]$ and (b) model p1q10Y22DM12 at $R = 65$ using $[J,N] = [400,46],[400,47]$.

		J	N	$\lambda_{\max}$	SRMS	$\mathbf{B}$	(S,T)	VRMS
a		1600	28	0.411688				1.695922
		2400	28	0.392799				1.695956
	(M)AD				0.000073	0.000088	0.000040	0.000034
	(M)MD				0.000045	0.000079	0.000036	0.000013
	(M)RD			0.048088	0.003436			0.000020
b		1600	28	1.565015				2.296459
		2400	28	1.542210				2.296093
	(M)AD				0.000134	0.000125	0.000145	0.000367
	(M)MD				0.000130	0.000116	0.000125	0.000111
	(M)RD			0.014572	0.004230			0.000160

Table 6.14: Comparison of λ, SRMS, $\mathbf{B}$, (S,T) and VRMS for (a) model p1Y22DM12 at $R = 220$ using $[J,N] = [2400,28],[1600,28]$ and (b) model p1q10Y22DM12 at $R = 65$ using $[J,N] = [2400,28],[1600,28]$.

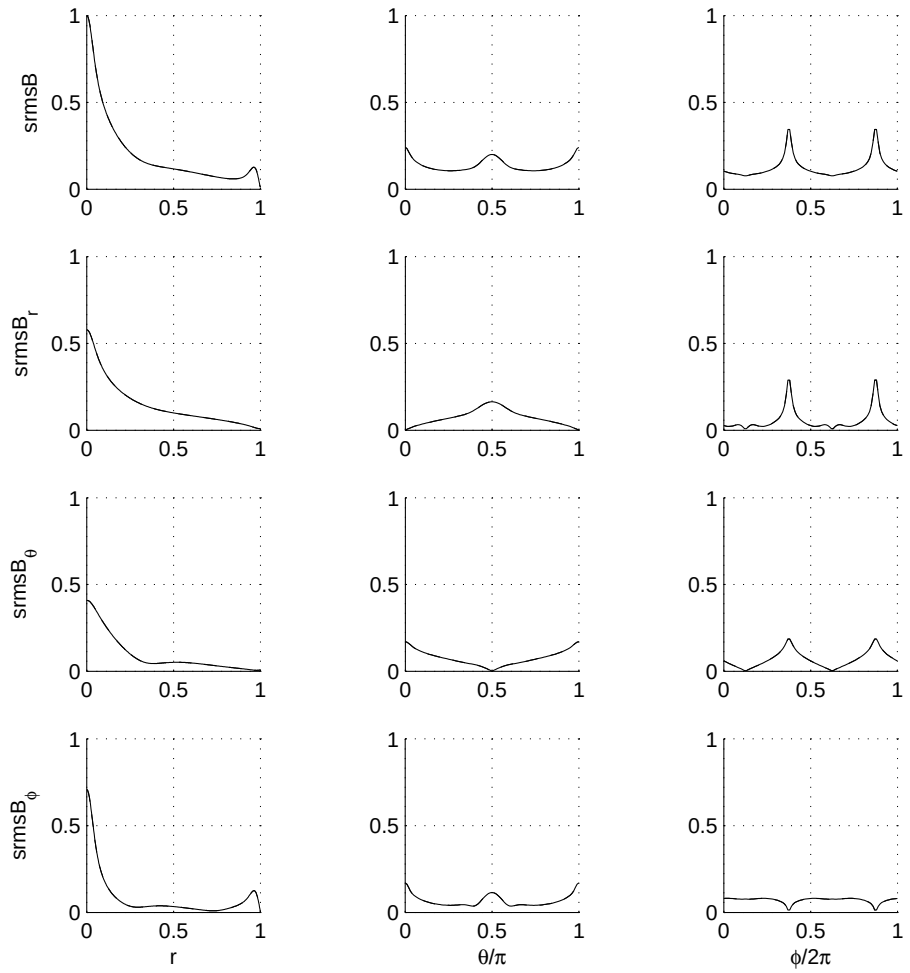

Figure 6.6: SRMS quantities for model p1Y22DM12 at $R = 220$ using two truncation levels: $[J, N] = [400, 55]$ and $[J, N] = [400, 56]$.

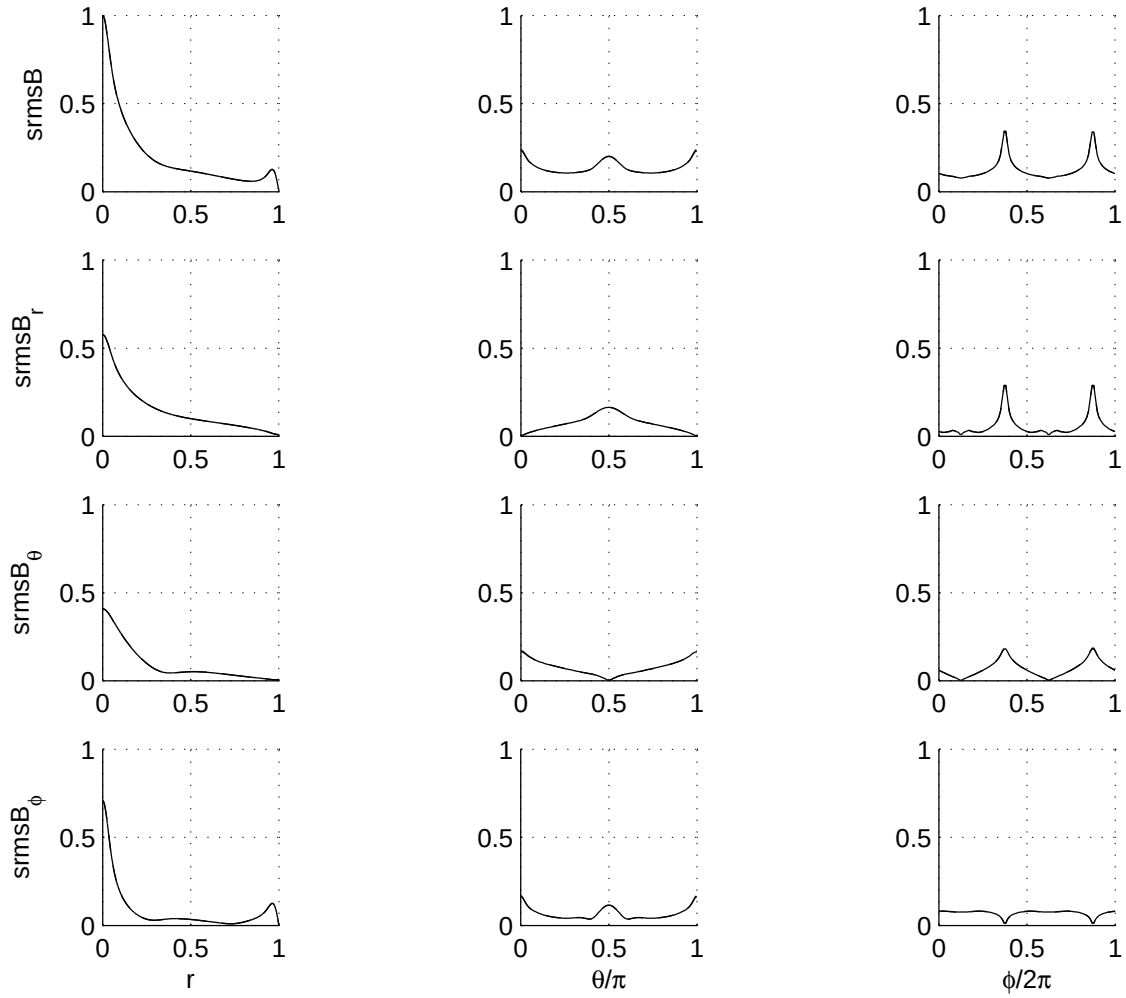

Figure 6.7: SRMS quantities for model p1Y22DM12 at $R = 220$ using two truncation levels: $[J, N] = [400, 56]$ and $[J, N] = [2400, 28]$.

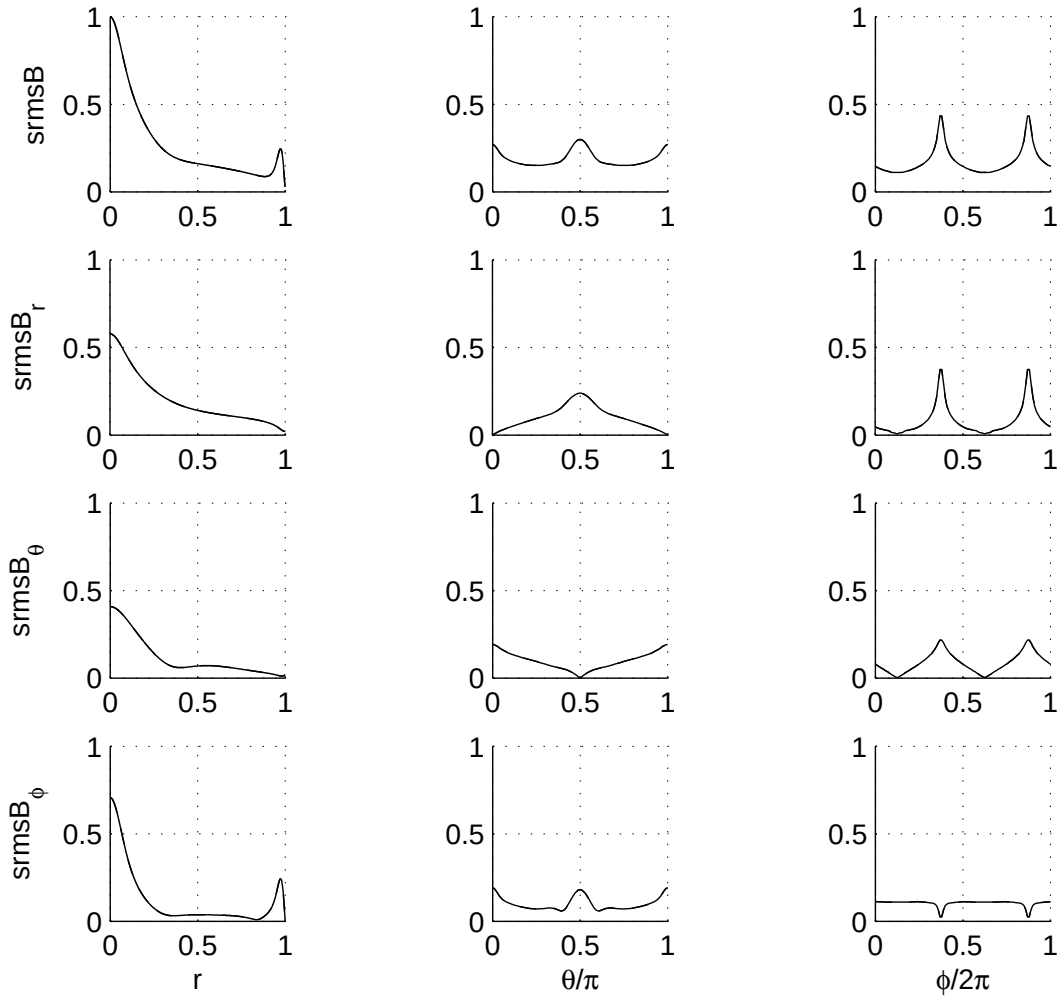

Figure 6.8: SRMS quantities for model p1q10Y22DM12 at $R = 65$ using two truncation levels: $[J, N] = [1600, 28]$ and $[J, N] = [2400, 28]$.

6.6 $\lambda_{\max}$ Estimation

Besides indicating convergence, $\lambda_{\max}(h^2)$ and $\lambda_{\max}(N)$ plots can also be used in estimating $\lambda_{\max}$ for higher $[J, N]$. For $\lambda_{\max}(h^2)$, we can estimate $\lambda_{\max}$, for a fixed N and $J \to \infty$, by linearly extrapolating our data to get $\lambda_{\max}(h^2)$ as $h \to 0$. Table 6.15 shows the $\lambda_{\max}$ estimation for models p1Y22DM12 and p1q10Y22DM12 using the extrapolation of $\lambda_{\max}(h^2)$ plots in Figures 3.6 and 3.14. The earlier plots, Figures 3.5 and 3.13, show that the variation of $\lambda_{\max}$ decreases a N increases. Therefore, we estimate the bound of $\lambda_{\max}$ for $J, N \to \infty$ using Table 6.15. For model p1Y22DM12,

$$0.35 < \lambda_{\max}(\infty, \infty) < 0.45. \tag{6.36}$$

For model p1q10Y22DM12,

$$1.54 < \lambda_{\max}(\infty, \infty) < 1.59. \tag{6.37}$$

The behaviour of $\lambda_{\max}(N)$ for various fixed J, as shown in Figures 3.5 and 3.13, suggests $\lambda_{\max}(N)$ might be extrapolated using the underdamped oscillator function

$$\lambda_{\max}(J, N) = \lambda_{\max}(J, \infty) + b(J)e^{-\alpha N}\cos(\beta N + \gamma). \tag{6.38}$$

A similar function was used by PAS (1973) in estimating R_{crit} for their model. Least squares fitting of (6.38) results in the parameter values for $\lambda_{\max}$, $b(J)$, α, β, γ shown in Tables 6.16 and 6.17. From these tables, we infer $\lambda_{\max} \approx 0.39$ at $R = 220$ for p1Y22DM12 and $\lambda_{\max} \approx 1.59$ at $R = 65$ for p1q10Y22DM12. These estimates are consistent with the bounds in (6.36) and (6.37). Based on Tables 6.16 and 6.17, the convergence level for models p1Y22DM12 and p1q10Y22DM12 are 5% and 1% respectively. In addition, the visual fits of (6.38) of these models are shown in Figure 6.9, which shows the data are well represented by (6.38) and convergence is occurring.

	$\lambda_{\max}(h^2=0)$	
N	p1Y22DM12 $R=220$	p1q10Y22DM12 $R=65$
36	0.3466	1.5372
37	0.4485	1.5858
38	0.4321	1.5868
39	0.3520	1.5464
40	0.3609	1.5451
41	0.4266	1.5784
42	0.4201	1.5793
43	0.3674	1.5515
44	0.3718	1.5509
45	0.4147	1.5740

Table 6.15: $\lambda_{\max}$ estimation for models p1Y22DM12 and p1q10Y22DM12 using $\lambda_{\max}(h^2)$ plot. These numbers are the y-intercept of the lines in Figures 3.6 on page 40 and 3.14 on page 47.

J	N	$\lambda_{\max}(J, N\to\infty)$	$b(J)$	α	β	γ
200	[25..55]	2.5383	-79.419	0.1908	1.5182	2.9114
400	[25..56]	0.93297	-66.633	0.1867	1.5173	2.9602
800	[25..45]	0.52431	-74.465	0.1915	1.5137	3.0658
1600	[25..35]	0.41600	-74.127	0.1915	1.5093	-3.1007
2400	[25..35]	0.39699	-73.989	0.1915	1.5093	-3.1009

Table 6.16: $\lambda_{\max}$ estimation for model p1Y22DM12 using the underdamped oscillatory function (6.38). The convergence with respect to J is around 5%.

J	N	$\lambda_{\max}(J, N\to\infty)$	$b(J)$	α	β	γ
200	[25..55]	4.1686	-33.447	0.1914	1.5154	2.6714
400	[25..56]	2.2235	-39.426	0.1999	1.5086	2.9155
800	[25..45]	1.7318	-47.443	0.2075	1.5045	3.0389
1600	[25..35]	1.6117	-48.192	0.2087	1.4986	3.2096
2400	[25..35]	1.5890	-48.532	0.2091	1.4984	3.2163

Table 6.17: $\lambda_{\max}$ estimation for model p1q10Y22DM12 using the underdamped oscillatory function (6.38). The convergence with respect to J is around 1%.

(a)

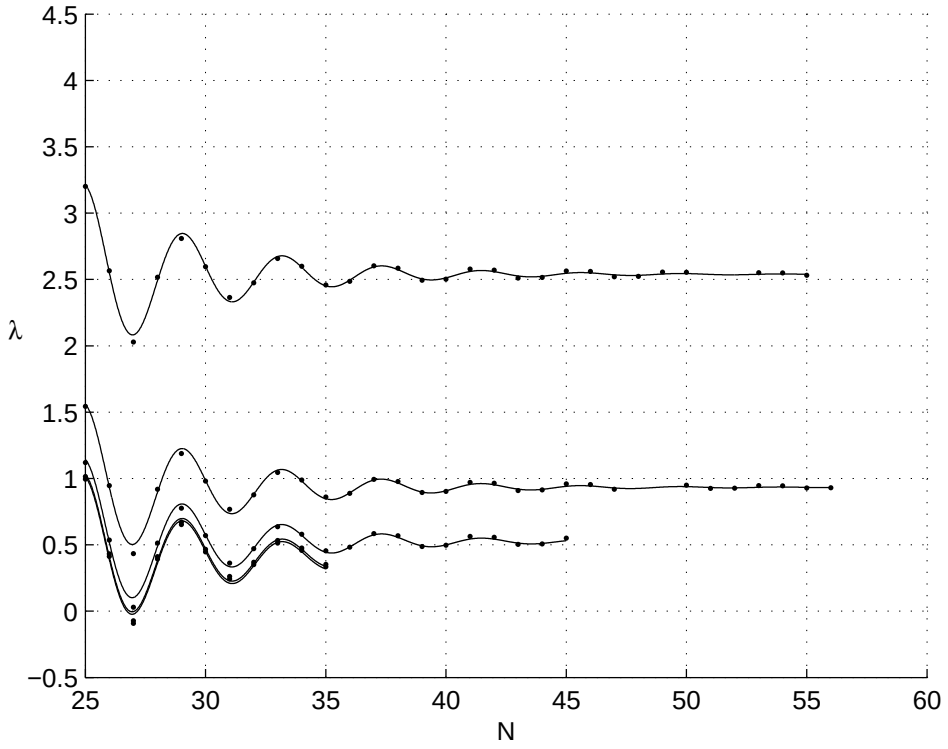

(b)

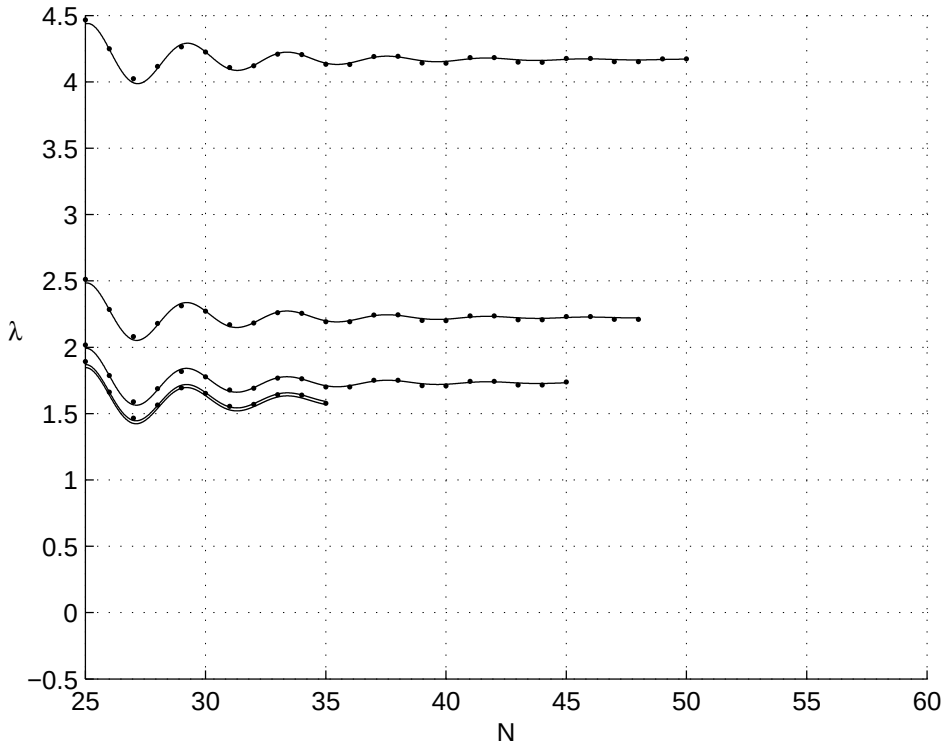

Figure 6.9: The plot of (a) the underdamped oscillatory function (6.38) for model p1Y22DM12 using the same $[J, N]$ as in Figure 3.5, (b) the underdamped oscillatory function (6.38) for model p1q10Y22DM12 using the same $[J, N]$ as in Figure 3.13. The convergence with respect to J and N is observable.

6.7 Chapter Summary

In Chapter 3, we pursued better convergence levels for models p1Y22DM12 and p1q10Y22DM12 by increasing $[J, N]$ up to the limit of our computational capacity. Although we achieved much better convergence results than BIJ, we still could not get 1% convergence levels. This led us to assess various convergence tests and apply them to p1Y22DM12 and p1q10Y22DM12.

There are various tests that have been used by other authors to study the convergence of kinematic dynamos. The λ, (S, T) and $\mathbf{B}$ tests are the most common tests. We introduced two new tests: SRMS and VRMS, the latter is a modification of the test used by PAS (1973). Before applying them to p1Y22DM12 and p1q10Y22DM12, we compared their performance visually and numerically using the models of PAS, KR, DJ, α^2 and free decay.

We came to no general conclusion as to which test is the most sensitive. However, our numerical results reveal:

1. No test is always most sensitive.
2. SRMS is usually more sensitive than (S, T) and VRMS.
3. VRMS is the least sensitive with two exceptional cases.
4. SRMS graphs are convenient to observe convergence visually.

When we applied the tests to p1Y22DM12 and p1q10Y22DM12, we found that the convergence level of $\mathbf{B}$ is less than 1%, as indicated by MAD($\mathbf{B}$) and MMD($\mathbf{B}$). In §6.6, we showed that $\lambda_{\max} \approx 0.4$ for model p1Y22DM12 at $R = 220$, and $\lambda_{\max} \approx 1.6$ for model p1q10Y22DM12 at $R = 65$. So, we conclude that models p1Y22DM12 and p1q10Y22DM12 do provide numerical evidence of successful dynamos and that the planar velocity anti dynamo theorem does not apply for finite spherical conductors.

Chapter 7

Conclusions

In this thesis, we have studied planar velocity dynamos. We have extended the work of BIJ (2006) who proposed model p1Y22DM12 that indicates the existence of a planar velocity dynamo. We have conducted a number of numerical experiments, which we now summarize to conclude this thesis.

In Chapter 3, we began our experiment by investigating p1Y22DM12 at higher $[J, N]$. We used a sub-band method to achieve higher $[J, N]$ and obtained better convergence results. The convergence level of $\lambda_{\max}$, as measured by $\mathrm{RD}(\lambda_{\max})$, is now around 1–5% compared to BIJ's approximately 10% level. The numerical results are presented in Table 3.2 on page 39 and Figure 3.5 on page 40. In addition, we found another model, p1q10Y22DM12, which has better convergence ($\mathrm{RD}(\lambda_{\max}) \lesssim 1.5\%$) compared to p1Y22DM12. This model is a modification of p1Y22DM12; its radial function f_2^2 has greater gradient near $r = 1$. Table 3.5 on page 46 and Figure 3.13 on page 46 show the numerical results for this model. We also investigated several related models: p1Y42DM12 and p1Y44DM24 in §3.4.2. These gave preliminary indication of possibly successful dynamos, but our investigation proved them to have worse convergence problems than p1Y22DM12.

In Chapter 4, we allowed two types of inner core: insulating and conducting. Our numerical results, presented in Tables 4.3–4.5 on page 62 and Figures 4.4–4.9 on page 65, reveal that inner cores may improve the convergence level of $\lambda_{\max}$. However, to get a 1% level of convergence, we needed to use almost the same $[J, N]$ as for p1Y22DM12. Thus, we did not attempt to use higher $[J, N]$ but rather, sought other planar flows that might converge better. In Chapter 4, we also showed that the PAS flow, with a minor modification, can be fully planarized inside spherical shells. Although, this flow was not found to be capable of maintaining a magnetic field, the modification process led us to investigate other planar flows.

In Chapter 5, we modified the PAS flow so that it could be fully planarized in a sphere. We constructed two modified PAS flows: biPAS and quasiPAS, and investigated the unplanarized, partly planarized and fully planarized versions of these. In

total, we discovered nineteen new successful dynamos in the unplanarized and partly planarized versions of biPAS and quasiPAS models. Some of these dynamos have a lower R_{crit} than that of PAS. The numerical results are shown in Tables 5.1–5.6 on page 82. However, we were not able to find a fully planarized versions of biPAS and quasiPAS models that acted as a dynamo, in the interval $0 \leq R \leq 0.4$ with magnetic chain M12.

Lastly in Chapter 6, we investigated the convergence of models p1Y22DM12 and p1q10Y22DM12 using various convergence tests, which we called the λ, $\mathbf{B}$, (S, T), SRMS and VRMS tests. We discovered that all convergence tests, apart from the λ test, show that p1Y22DM12 and p1q10Y22DM12 were able to maintain a magnetic field. Our results revealed that $\lambda_{\max}$ is quite sensitive to $[J, N]$ changes in these models. By using both linear extrapolation, and least squares fitting of an underdamped oscillatory function, we obtained supercritical estimation of $\lambda_{\max} \approx 0.39$ at $R = 220$ for p1Y22DM12, and $\lambda_{\max} \approx 1.59$ at $R = 65$ for p1q10Y22DM12. The numerical results supporting these estimations, are shown in Table 6.9 on page 115.

Our results clearly indicate models p1Y22DM12 and p1q10Y22DM12 are convergent. But achieving 1% convergence level would require more computer capacity in terms of speed and memory or an alternative numerical method not based on spherical harmonics.

For future work, there are at least two directions that we can follow: solving the problem using parallel computing techniques, or using a time-stepping method so we only have to store the eigenvector. Both directions require a new different computational dynamo routine.

Appendix Schuster's Formula

The Schuster formula (Schuster, 1903) is

$$\int_{-1}^{1} P_{n_1}^{m_1}(\cos\theta) P_{n_2}^{m_2}(\cos\theta)\,\mathrm{d}\cos\theta =$$
$$c \sum_{i=m_1}^{i=n_1}{}^{(2)} (-1)^{\frac{i-m_1}{2}} \frac{(n_1+m_1)!!(n_1+i-1)!!(n_2+m_2-1)!!(n_2-i-2)!!(m_2+i)!!}{(n_1-m_1-1)!!(n_1-i)!!(n_2-m_2)!!(n_2+i+1)!!(m_2-i-2)!!}$$
$$\frac{1}{(i-m_1)!!(i+m_1)!!},$$

where $\sum_{i=m_1}^{i=n_1}{}^{(2)}$ means summing for $i = m_1, m_1+2, m_1+4, ..., n_1$, c equal to 2 or π according as $m_2 - m_1$ is even or odd and

$$n!! = \begin{cases} n(n-2)(n-4).... & \text{, when } n \text{ is positive, the last factor is either 1} \\ & \text{ or 2 according as } n \text{ is odd or even,} \\ (-1)^{\frac{-n-1}{2}} \frac{1}{(-n-2)!!} & \text{, when } n \text{ is negative and odd,} \\ \infty & \text{, when } n \text{ is negative and even.} \end{cases}$$

Appendix Program list

Below are the programs used. The author was A.A. Bachtiar (AAB) except where otherwise indicated. All programs have been checked independently by R.W. James (RWJ) except where indicated by (*). Some abbreviations: Fortran77(F77), Fortran90(F90), MATLAB(M), *Mathematica*(Math).

Routine	Software	Comments
1. Main dynamo program	F77, F90	Written by M.L. Dudley, modified by RWJ, followed by AAB to allow sub band method, checked against results from earlier researchers.
2. Planar flows	F90	Independently checked by D.J.Ivers.
3. Spherical shell dynamo	F90	Checked against results from earlier researchers.
4. BiPAS flow of §5.2 on page 68	F90	
5. QuasiPAS flow of §5.3 on page 76	F90	
6. SRMS test of §6.2 on page 88	F90	
7. VRMS test of §6.3 on page 94	F90	
8. **B** test of §6.1.3 on page 88	F90	
9. (S,T) test of §6.1.2 on page 87	M	
10. Planar velocity's Streamlines	M	
11. Least square fitting of underdamped oscillator function of §6.6 on page 113	M	Written by RWJ.
12. Evaluation of $\int_0^\pi P_{n_1}^{m_1} P_{n_2}^{m_2} \, \mathrm{d}\theta$	M(*)	Using built-in functions: legendre and quad, checked using the methods below.
	Math(*)	Using built-in functions: LegendreP and Integrate.
	F90	Using Gauss-Kronrod method available from Guide to Available Mathematical Software(GAMS).
	F90(*)	Formula given by Schuster (1903).

Bibliography

Backus, G. E. & Chandrasekhar, S. 1956 On Cowling's theorem on the impossibility of self-maintained axisymmetric homogeneous dynamos. *Proc. Nat. Acad. Sci. USA*, **42**, 105–109.

Backus, G. E. 1958 A class of self sustaining dissipative spherical dynamos. *Ann. Phys., (N.Y.)*, **4**, 372–447.

Bullard, E. C. 1949 The magnetic field within the earth. *Proc. Roy. Soc.* **197**, 433–453.

Bullard, E. C. 1955 The stability of a homopolar dynamo *Proc. Camb. Phil. Soc.* **51**, 744–760.

Bullard, E. C. & Gellman, H. 1954 Homogeneous dynamos and terrestrial magnetism. *Phil. Trans. R. Soc. Lond.* A **247**, 213–278.

Bullard, E. C. & Gubbins, D. 1977 Generation of magnetic fields by fluid motions of global scale. *Geophys. Astrophys. Fluid Dynamics.* **8**, 43–56.

Bachtiar, A. A., Ivers D. J. & James, R. W. 2006 Planar velocity dynamos in a sphere. *Proc. R. Soc. Lond.* A **462**, 2439–2456.

Chapman, S. & Bartels, J. 1962 *Geomagnetism*, vol.II. Oxford: Oxford University Press.

Cowling, T. G. 1934 The magnetic field of sunspots. *Mon. Not. Roy. Astron. Soc.*, **94**, 39–48.

Cowling, T. G. 1976 *Magnetohydrodynamics*, Monographs on Astronomical Subject, Adam Hilger Ltd, 1976.

Dudley, M. L. 1988 A numerical study of kinematic dynamos with stationary flows. Ph.D. thesis, University of Sydney.

Dudley, M. L. & James, R. W. 1989 Time-dependent kinematic dynamos with stationary flows. *Proc. R. Soc. Lond.* A **425**, 407–429.

Friedman, A. 1964 *Partial differential equations of parabolic type*. Prentice-Hall, New Jersey.

Gibson, R. D. & Roberts, P. H. 1967 Some comments on the theory of homogeneous dynamos. In *Magnetism and the cosmos* (ed. W. R. Hindmarsh, F. J. Lowes, P. H. Roberts and S. K. Runcorn). New York: Wiley Interscience.

Glatzmeir, G. A. & Roberts, P. H. 1995 A three-dimensional self-consistent computer simulation of a geomagnetic field reversal. *Nature*, **377**, 203–209.

Gubbins, D. 1972 Geomagnetic dynamos. Ph.D. thesis, University of Cambridge.

Gubbins, D. 1973 Numerical solutions of the kinematic dynamo problem. *Phil. Trans. R. Soc. Lond.* A **274**, 493–521.

Herzenberg, A. 1958 Geomagnetic dynamos. *Phil. Trans. Roy. Soc. Lond.* A **250**, 543–583.

Hobson, E.W. 1931 *Theory of spherical and ellipsoidal harmonics*. University Press: Cambridge.

Hollenbach, D. F. & Herndon, J. M. 2001 Deep-Earth reactor: Nuclear fission, helium, and the geomagnetic field. *Proc. Nat. Ac. Sc.*, **20**, 11085–11090.

Hollerbach, R. & Jones, C. A. 1995 On the magnetically stabilizing role of the Earth's inner core. *Physics of the Earth and Planetary Interiors*, **87**, 171–181.

Holme, R. 1997 Three-dimensional kinematic dynamos with equatorial symmetry: Application to the magnetic fields of Uranus and Neptune. *Physics of the Earth and Planetary Interiors*, **102**, 105–122.

Inglis, D. R. 1955 Theories of the Earth's magnetism. *Rev. Mod. Phys.*, **27**, 212–248.

Ivers D. J. & James, R. W. 1984 Axisymmetric antidynamo theorems in compressible non-uniform conducting fluids. *Phil. Trans. R. Soc. Lond.* A **312**, 179–218.

Ivers D. J. & James, R. W. 1988 An antidynamo theorem for partly symmetric flows. *Geophys. Astrophys. Fluid Dynamics.* **44**, 271–278.

James, R. W. 1974 The Adams and Elsasser dynamo integrals. *Proc. R. Soc. Lond.*, A **331**, 469–478.

James, R. W. 1974 The spectral form of the magnetic induction equation. *Proc. R. Soc. Lond.*, A **340**, 287–299.

Kumar, S. & Roberts, P. H. 1975 A three-dimensional kinematic dynamo. *Proc. R. Soc. Lond.* A **344**, 235–258.

Larmor, J. 1919 How could a rotating body such as the sun become a magnet? *Rep. Br. Assoc. Adv. Sci.* **4**, 159–160.

Lilley, F. E. M. 1970 On kinematic dynamos. *Proc. R. Soc. Lond.* A **316**, 153–167.

Lortz, D. 1968 Impossibility of steady dynamos with certain symmetries. *Physics Fluids.* **11**, 913–915.

Malin, S. 1987 Historical Introduction to Geomagnetism.*Geomagnetism*, vol. 1, Academic Press.

Merril, R. T., McElhinny, M. W. & McFadden, P. L. 1996 *The magnetic field of the Earth.* International geophysics series, vol. 63. Academic Press.

Moffat, H. K. 1970 Turbulent dynamo action at low magnetic Reynolds number. *J. Fluid Mech.*, **41**, 435–452.

Moffat, H. K. 1978 *Magnetic field generation in electrically conducting fluids.* Cambridge University Press.

Namikawa, T. & Matsushita, S. 1970 Kinematic dynamo problem. *Geophys. J. R. Astr. Soc.*, **19**, 319–415.

Parker, E. N. 1955 Hydromagnetic dynamo models. *Astrophys. J.* **122**, 293–314.

Pekeris, C. L., Accad, Y. & Shkoller, B. 1973 Kinematic dynamos and the Earth's magnetic field. *Proc. R. Soc. Lond.* A **275**, 425–261.

Rikitake, T. 1958 Oscillations of a system of disk dynamos. *Proc. Camb. Phil. Soc.*, **54**, 89–105.

Rikitake, T. & Honkura, Y. 1985 *Solid Earth Geomagnetism.* Tokyo: TERRAPUB.

Roberts, P. H. 1967 *An Introduction to Magnetohydrodynamics*. Longmans. London; Elsevier, New York.

Roberts, P. H. & Stix, M. 1972 α-effect dynamos, by the Bullard-Gellman formalism. *Astron.& Astrophys.* **18**, 453–466.

Sarson, G. R. 2003 Kinematic dynamos driven by thermal-wind flows. *Proc. R. Soc. A*, **459**, 1241–1259.

Sarson, G. R. & Gubbins, D. 1996 Three-dimensional kinematic dynamos dominated by strong differential rotation. *J. Fluid Mech.*, **306**, 223–265.

Schuster, A. 1903 On some definite integrals, and a new method of reducing a function of spherical co-ordinates to a series of spherical harmonics. *Phil. Trans. R. Soc. Lond.*, **200**, 181–223.

Sperb, R. 1981 *Maximum principles and their applications.* New York: Academic Press.

Wilkinson, J. H. 1965 *The algebraic eigenvalue problem.* Oxford : Clarendon Press.

Wilson, R. L. 1962a The palaeomagnetism history of a doubly-baked rock. *Geophys. J. Roy. Astron., Soc.,* **6**, 397–399.

Wilson, R. L. 1962b The palaeomagnetism of baked contact rocks and reversals of the earth's magnetic field. *Geophys. J. Roy. Astron., Soc.,* **7**, 194–202.

Zel'dovitch, Ya. B. 1957 The magnetic field in the two-dimensioned motion of a conducting turbulent liquid. *JETP*, **4**, 460.

Zel'dovitch, Ya. B. & Ruzmaikin, A. A. 1980 The magnetic field in a conducting fluid in two-dimensional motion. *Soviet Phys. JETP*, **51**, 493–497.